DYNAMIC STRESS CONCENTRATION IN A SINGLE PARTICLE COMPOSITE

Sinisa Bugarin

A thesis submitted to the Faculty of Engineering and the Built Environment, University of the Witwatersrand, Johannesburg, in fulfilment of the requirements for the degree of Doctor of Philosophy.

Johannesburg, 2012

Abstract

The fracture and fatigue properties of particle reinforced matrix composites are greatly influenced by stress concentration around the reinforcements as the failure of a structural member often initiates at regions of high stress concentration. Determining stress concentration has been the focus of number of researchers for quite some time in order to better understand the failure mechanics of structural members. The first part of the study investigates the stress concentration around a spheroidal particle that is embedded in a large elastic matrix and subjected to dynamic loading. Interaction between neighboring particles is ignored. The results are therefore valid for composites with low volume fractions. The problem is studied by extending a hybrid technique that was previously developed for axisymmetric loading. In the hybrid technique, a fictitious spherical boundary enclosing the particle is drawn. The fictitious boundary divides the entire region into interior and exterior regions. The interior region is modeled through an assemblage of conventional finite elements while the exterior region is represented by spherical wave functions. Coupling of the solutions for the interior and exterior regions is achieved by imposing the continuity of displacements and tractions along the common boundary B. This leads to a set of linear equations that enables the displacements and stresses at any point to be determined. It is found that the stress concentrations within the matrix at the matrix-particle interface are dependent on the frequency of the dynamic excitation, aspect ratio of the particle and the material properties of both matrix and a particle. The study reveals that the dynamic stress concentration can reach much higher values than the static case.

A second part of the study involved investigating the potential of using an interphase layer to reduce stress concentrations under a dynamic loading in Mg matrix surrounding a SiC particle. An interphase layer was applied between the particle and the matrix and the contact between them was assumed to be perfect. Both constant property materials and functionally graded materials were considered for the interphase. A constant property interphase was modelled as a single layer while a functionally graded interphase was divided into a number of sublayers and each sublayer was treated as having constant material properties. Numerical results reveal that the interphase layer made of a constant property material shows better stress concentration reduction than that made of functionally graded materials. An interphase layer with low values of both shear modulus and Poisson's ratio is necessary for a significant stress concentration reduction. Studies were focused on reducing the concentration that occurs over a range of frequencies.

The third part of the study investigates the size effects as the particle size reduces to nanometers. This part of the study was inspired by the current interest in nanomaterials. For instance, a quantum dot that is embedded in the matrix of a composite could introduce stress concentrations under dynamic loading. This is studied here by using the surface/interface theory of elasticity. It is found that the stress concentration values are significantly dependent on the elastic properties of the surface/interface and the frequency of excitation.

The work presented here has resulted in three publications in international journals and three conference presentations. The complete list is given below:

1. R. Paskaramoorthy, S. Bugarin and R. Reid: Effect of an interphase layer on the dynamic stress concentration in a Mg-matrix surrounding a SiC-particle. *Journal of Composite and Structures, 2009, 91, 451–460.*

2. R. Paskaramoorthy, S. Bugarin and R. Reid. Analysis of stress concentration around a spheroidal cavity under asymmetric dynamic loading. *Journal of Solids and Structures, July 2011, 48, Issues 14-15, 2255-2263.*

3. S. Bugarin, R. Paskaramoorthy and R. Reid. Influence of the geometry and material properties on the dynamic stress field in the matrix containing a spheroidal particle reinforcement. *Composite Part B: Engineering, Volume 43, Issue 2, March 2012, Pages 272-279*

4. Paskaramoorthy R, Bugarin S, Reid RG. A hybrid finite element method for stress concentration in a single fibre composite. *ASME 2011 Applied Mechanics and Materials Conference in Chicago, Illinois, USA, June 2011.*

5. Bugarin S, Paskaramoorthy R, Reid RG. A hybrid finite element method for stress analysis around an inhomogeneity under dynamic loads. *South African Conference on Applied Mechanics, 2010, University of Pretoria, South Africa.*

6. Paskaramoorthy R, Bugarin S, Reid RG. On the reduction of dynamic stress concentrations in a SiC/Mg composite using interphase layers. *Proceedings of the Sixth International Conference on Composite Science and Technology, Durban, January 2007. (ISBN: 1-86840-642-3)*

Declaration

I declare that this thesis is entirely my own work. It is being submitted for the degree of Doctor of Philosophy in the University of The Witwatersrand, Johannesburg. It has not been submitted before for any degree or examination in any other University.

_____

(Signature of candidate)

_____day of_____ 2012

Acknowledgments

I would like to thank my supervisor Professor R. Paskaramoorthy, for his assistance in guiding me into the world of scientific research. Many thanks also go to National Aerospace Centre of Excellence in Strong Materials for bursary support during this research study. To my colleagues Kmil Midor, Andrew Allcock, Nico Wilke and Adolph Vogel I extend my gratitude for help and advice with Matlab and Python programming.

Table of Contents

List of Figures

Glossary of terms

U - displacement vector
σ_{xx} - normal stress in Cartesian coordinate system
σ_{xy} - shear stress in Cartesian coordinate system
ε_{xx} - normal strain in Cartesian coordinate system
ε_{xy} - shear strain in Cartesian coordinate system
σ_{RR} - normal stress in Spherical coordinate system
$\sigma_{R\theta}$ - shear stress in Spherical coordinate system
ε_{RR} - normal strain in Spherical coordinate system
$\varepsilon_{R\theta}$ - shear strain in Spherical coordinate system
R - radial distance from the centre of inhomogeneity in Spherical coordinates system
r - radial distance from the centre of inhomogeneity in Cylindrical coordinates system
a - dimension of the inclusion along the $\boldsymbol{x}$ axis
b - dimension of the inclusion along the $\boldsymbol{z}$ axis
θ - angle in $\boldsymbol{zx}$-plane
ϕ - angle in $\boldsymbol{xy}$-plane
t - time variable
λ - Lamé constant of the material
μ - Lamé constant of the medium
ν - Poisson's ratio of the medium
ρ - density of the medium
ω - frequency of the incident wave
ω^* - normalized frequency of the incident wave
α - wave number
β - wave number
j_n - Spherical Bessel function of the first kind
y_n - Spherical Bessel function of the second kind
P_n^m - Legendre polynomial
$h_n^{(1)}$ - Henkel function of the first kind
$h_n^{(2)}$ - Henkel function of the second kind
χ - Pressure wave potential function
φ - Shear wave potential function
ψ - Shear wave potential function

1. Introduction

1.1. Introduction to Composites

A composite material is a microscopic combination of two or more distinct materials, having a recognizable interface between them, which have been bonded together at a scale that is sufficiently fine that the result can be considered a material with properties of its own. Composites are engineered materials that have been designed to provide higher structural efficiency, which is higher specific strength and specific stiffness relative to previously available materials. High strength and modulus of elasticity of reinforcements provide strength and stiffness in composites. By selecting the reinforcements with desired levels of strength and stiffness and by controlling the volume fraction of reinforcements the actual magnitude of composite strength and stiffness can be controlled. Composites are used not only for their structural properties, but also for their thermal, electrical and environmental applications. Modern composites are usually optimized to achieve a particular balance of properties for a given range of applications. The composite material has a balance of structural properties that is superior to either constituent material alone. The improved structural properties generally result from a load-sharing mechanism.

Composites typically have a fibre or particle phase that is stiffer than the continuous matrix phase. The distinction of the matrix in composite from other two or more phase alloys comes about from the processing of the composite. This is possible by the virtue of the fact that the melting temperature of the matrix is much lower than that of the reinforcement and the two can be mixed together to distinguish a composite from two or more phase alloys. Many types of reinforcements often have good thermal and electrical conductivity, good wear resistance and a coefficient of thermal expansion (CTE) that is less than the matrix. Composites are commonly classified at two distinct levels. The first classification is usually made with respect to the matrix constituent of which major composite classes include organic-matrix composites (OMCs), metal-matrix composites (MMCs) and ceramic-matrix composites (CMCs). In each of these composites the matrix is typically a continuous phase throughout the component. The second level of classification refers to the reinforcement form being particulate-reinforcement, whisker reinforcement, continuous fibre reinforcement (see Figure 1.1) and woven fibre composites (braided and knitted fibre architectures). The reinforcement volume fraction must generally be substantial (10% or more) to provide a useful increase in properties.

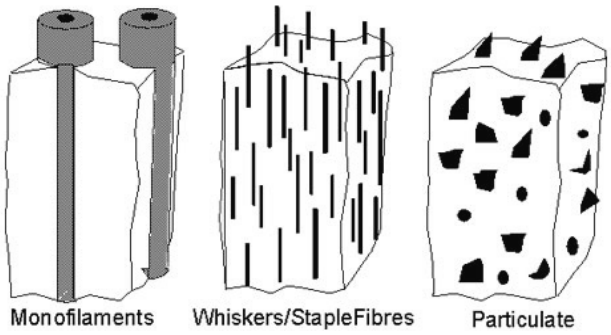

Figure 1.1 Schematic showing the three main types of composite [1]

Particulate-reinforcements and whisker reinforcement are classified as “discontinuous” reinforcements as the reinforcing phase is discontinuous for the lower volume fraction (20% - 30%) typically used in MMCs. In particle reinforcement all of particle’s dimensions are roughly equal and thus, particle-reinforced composites include those reinforced by spheres, flakes and many other shapes of roughly equal axes. Whisker reinforcements, with an aspect ratio typically between 20 to a 100 are often considered together with particulates in MMCs. Continuous fibre-reinforced composites contain reinforcements that have length much greater than their cross-sectional dimensions and their length is comparable to the overall dimensions of the composite part. The prime role of the fibers is to carry the load, while the matrix serves to transfer and distribute the load to the fibers.

In fibre-reinforced composites, the strength and stiffness can also be controlled by specifying the fibre direction. Highest structural efficiency is obtained when fibres are aligned along the primary loading direction within the composites, which provides part of the motivation for the widespread use of these materials. Simultaneously this fibre orientation produces a material with lower structural efficiency for the loads perpendicular to the fibre direction. These highly anisotropic properties must be considered in the use of such materials.

The purpose of the matrix is to bind the reinforcements together by virtue of its cohesive and adhesive characteristics, to transfer the load to and between reinforcements, and to protect the reinforcements from environmental handling. The matrix also provides a solid form to the composite that aids in handling of the finished part in manufacture. In discontinuously reinforced composites the matrix is particularly necessary as the reinforcements are not of sufficient length to provide manageable form. The matrix is often a “weak link” from a structural perspective in the composite since the reinforcements are typically stronger and stiffer. However the matrix allows the strength of reinforcements to be used to their full potential by holding reinforcing fibres in the proper orientation and position so that they can carry the intended loads and distribute the loads more or less evenly among reinforcements. A great deal of flexibility exists in the lay-up of composite. The fraction of fibres in any given direction can be tailored in proportion to the load that must be supported thereby significantly increasing structural efficiency of the composite. Some OMCs such as quasi-isotropic graphite/epoxy laminate provide in-plane isotropy as required in some applications.

The specific stiffness of quasi-isotropic laminated OMCs is significantly higher than structural metals, with the exception of few specialty titanium alloys and high strength steel.

Almost all high strength or high stiffness materials fail due to propagation of flaws under loading. A fibre of such a material is inherently stronger than the bulk form as the size of the flaw is limited by the small diameter of the fibre. If equal volumes of fibrous and bulk material are compared, the flaw that would produce the failure in fibres will not propagate to fail the entire assemblage of fibres, as would happen in the bulk material.

The technology base for fibre-reinforced MMCs is less established. Their use is limited due to factors such as high cost of constituent material and processing difficulties of monofilament-reinforced metal alloys. Cross-plied architectures have never been successfully demonstrated in any commercial fibre-reinforced MMC. One of the few commercially available is aluminium alloy reinforced with tow-based alumina (Al_2O_3) reinforcement which is significantly cheaper than the graphite/epoxy OMC. The applications of fibre-reinforced MMCs are limited to areas where metal-like behavior is important, including good wear resistance, elevated temperature operation, high electrical conductivity and high bearing strength.

Particle-reinforced metals provide essentially isotropic properties that are in the same general range as graphite/epoxy quasi-isotropic material. Discontinuously reinforced aluminium (DRA) is by far the most widely used MMC and a number of important applications have been established. For reinforcement volume fraction less than 25%, DRA has good fracture toughness and ductility, and structural efficiency that overlap that of quasi-isotropic organic matrix composites (OMC). For higher volume fraction the fracture properties are lower, but these materials are used widely for wear resistant applications, thermal management and electronic packaging. The relatively low cost and ease of manufacturing makes DRA an affordable material where high structural efficiency is required. Discontinuously reinforced titanium (DRTi) is less established than DRA, but already has important applications, including intake and exhaust valves in production automobile engines. Current DRTi materials provide a balance of specific strength and specific stiffness that is superior to any isotropic engineering material, including quasi-isotropic OMCs.

1.2. Introduction to metal-matrix composites

Metal Matrix Composites (MMCs) are composed of a metal matrix and a reinforcement, or filler material, which confers excellent mechanical performance, and can be classified according to whether the reinforcement is continuous (monofilament or multifilament) or discontinuous (particle, whisker, short fibre or other). The principal matrix materials for MMCs are aluminium and its alloys. To a lesser extent, magnesium and titanium are also used, and for several specialised applications a copper, zinc or lead matrix may be employed. The reinforcements can be metallic or ceramic (in general an oxide, a carbide or a nitride)

having much higher melting temperature than the matrix which allows mixing of the two distinct materials together to form a composite. MMCs with discontinuous reinforcements are usually less expensive to produce than continuous fibre reinforced MMCs, although this benefit is normally offset by their inferior mechanical properties. Consequently, continuous fibre reinforced MMCs are generally accepted as offering the ultimate in terms of mechanical properties and commercial potential.

The first focused effort to develop metal-matrix composites (MMC) originated in the early 1950s and 1960s. Historically, MMCs, such as steel-wire reinforced copper, were among the first continuous-fiber reinforced composites studied as a model system. Initial work in late 1960s was stimulated by the high-performance needs of the aerospace industry. In these development efforts, performance, not cost, was the primary driver. The principal motivation was to dramatically extend the structural efficiency of metallic materials while still retaining the already utilized advantages such as high shear strength, high chemical inertness and property retention at high temperatures. Boron filament, the first high-strength, high-modulus reinforcement, was developed both for metal- and organic- matrix composites. Because of the fiber-strength degradation and poor wettability in molten-aluminum alloys, the early carbon fibers could only be properly reinforced in organic-matrix composites. Therefore, the development of MMCs was primarily directed toward diffusion-bonding processing. At the same time, optimum (air stable) surface coatings were developed for boron and graphite fibers to facilitate wetting and inhibit reaction with aluminum or magnesium alloys during processing.

Early work on sintered aluminium powder was an initiator to discontinuously reinforced MMC. The development of high-strength monofilaments (first boron and then silicone carbide – SiC) significantly increased efforts on fibre-reinforced MMC throughout the 1960s and 1970s. Issues associated with processing, fibre damage and fibre-matrix interaction were established and overcome to produce useful materials. Despite the costs at the time and marginal reproducibility, important applications were established such as numerous components on the space shuttle orbiter (frame and rib truss members in the mid-fuselage section, see Figure 1.2). In the early 1970s, economic recession resulted in significant research and development funding cuts leading to an end of this phase of MMC discovery.

In the late 1970s efforts were again renewed on discontinuously reinforced MMCs using SiC whisker reinforcements. The high cost of whiskers and difficulty in avoiding whisker damage led to the concept of particulate reinforcement resulting in nearly equivalent strength and stiffness, but with much lower cost and easier processing. Both discontinuous and fibre-reinforced MMCs experienced tremendous increase in research and development throughout the 1980s. Major efforts were focused on particle-reinforced, whisker-reinforced and tow-based MMCs of aluminium, magnesium, iron and copper in applications mostly in automotive, thermal management, tribology and aerospace industries. In addition, monofilament-reinforced titanium MMCs were developed for high temperature applications primarily in aeronautical systems such as critical rotating components for advanced gas turbine engines and structures for high-Mach airframes. Since this period saw significant

improvements in performance and material quality of MMCs, there were an increasing number of generally small businesses that specialized in the production of MMCs for target markets. A growing number of MMC applications were entering service during this period. However, these successful insertions were not often widely advertised and so the full impact of MMC technology was not widely appreciated. Despite the successful production of MMCs such as continuous-fiber reinforced boron/aluminum (B/Al), graphite/ aluminum (Gr/Al), and graphite/ magnesium (Gr/Mg), the technology insertion was limited by the concerns related to ease of manufacturing and inspection, scale-up, and cost.

Significant investment provided by the U.S. Air Force, in the early 1990s, produced several milestone military and commercial aerospace applications of MMC technology in the United States, specifically of discontinuously reinforced aluminium (DRA). Greater benefits, other than just a simple weight reduction in components, provided motivation and cost justification for the use of DRA. In addition, new MMC with increasing insertions in ground transportation, industrial and thermal management and electronic packaging industries far exceeded the growth in the aerospace industries. In 1999, the MMC market for thermal management and electronic packaging alone was five times larger than the aerospace market, and the automotive transportation industry accounted for 62% of the total MMC world market. Due to the aggressive growth in ground transportation and thermal management this gap is expected to increase in future.

Figure 1.2 Mid-fuselage structure of Space Shuttle Orbiter showing boron-aluminum tubes [2].

The potential for MMCs in general and Aluminium Matrix Composites (AMCs) in particular, is enormous, and in certain technology areas their use is already established where conventional unreinforced materials have reached their limits.

Particulate reinforced metal-matrix composites (PRMMC) offer a wide range of attractive material properties that are not available with conventional engineering alloys. They are

based on the concept of using the characteristics of two different materials to make a material with superior properties compared to the unreinforced metals. Such material properties are the ductility and toughness of the metallic matrix and the modulus of elasticity and strength of the ceramic particulate reinforcement. The enhanced physical and material properties associated with PRMMCs are the direct result of the interaction between the matrix and reinforcement. During the cooling process, a geometric mismatch is created at the particle-matrix interface owing to the much higher thermal contraction of the metallic matrix in comparison to the ceramic reinforcements. The mismatch strains that are created at the interface are then relieved by generation of dislocations in the matrix originating from sharp features on the particulate reinforcement.

Metal alloy matrices, unlike their organic counterparts typically possess higher strength and in use with discontinuous reinforcements have much higher matrix volume fraction. Metal-matrix composites that are currently in service use matrices based on alloys of aluminium, titanium, iron, cobalt, copper, silver and beryllium. Copper, silver and beryllium MMCs are mostly used for thermal management as heat sink and electrical contacts. Iron MMCs are mostly used for industrial wear resistant applications and titanium MMCs are used primarily for automotive, aerospace and recreational products. The largest commercial application of DRTi is for automotive intake and exhaust valves as they require high-temperature resistant matrix alloy.

The UK's Advisory Council on Science & Technology in 1992 stated that MMCs can be viewed either as a replacement for existing materials, but with superior properties, or as a means of enabling radical changes in system or product design. Moreover, by utilising near-net shape forming and selective reinforcement techniques MMCs can offer economically viable solutions for a wide variety of commercial applications.

By far the most widely produced MMCs are based on aluminium alloy matrices. In general, the major advantages of Aluminium Matrix Composites (AMCs) compared to unreinforced materials, such as steel and other common metals, are as follows (see Figure 1.3):

- Increased specific strength, specific stiffness and elevated temperature strength
- Improved wear resistance and damping capabilities
- Tailorable thermal expansion coefficients
- Good corrosion resistance

These advantages can be quantified in terms of percentages. For instance, AMCs can offer potential mass savings of up to 60%, and increases in stiffness and strength of up to 200% when compared with, for example, conventional aluminium alloys. Furthermore, AMCs can be produced with near-zero coefficients of thermal expansion.

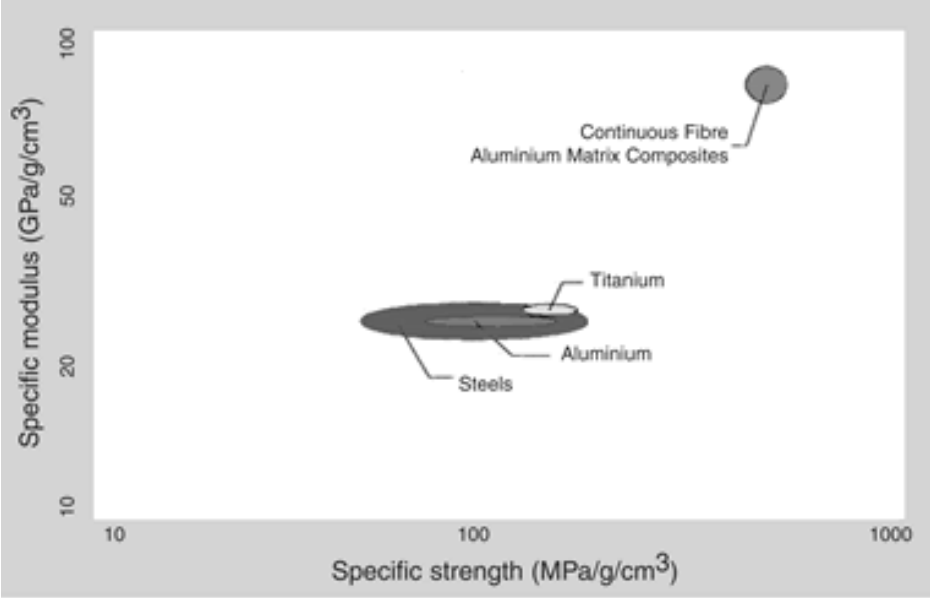

Figure 1.3 Properties of AMCs versus conventional alloys [3]

Aluminium-based MMCs are currently in use in automotive and rail ground transportation, thermal management and electronic packaging, aerospace and recreational applications. A wide range of cast and wrought aluminium alloys are used as matrices in aluminium MMCs. The most widely used MMC casting alloys are based on aluminium-silicone, which are used to produce foundry ingots. The high content of silicone in aluminium alloy improves castability and minimizes chemical interaction with SiC reinforcements during melting.

In particle-reinforced composites significant improvements are obtained, for example, by the addition of 20% SiC to 6061 aluminium. An increase in strength of over 50% and an increase in stiffness of over 40% is achieved in this manner. In addition to structural properties, typical particle-reinforcing materials such as SiC, graphite and glass may also provide good thermal and electrical conductivity, controlled thermal expansion and good wear resistance. By adding ceramic reinforcement, one can generally reduce the coefficient of linear thermal expansion of the composite giving ability to control thermal expansion in applications involving electronic packaging

Abrasive-grade ceramic grit is usually used for particulate reinforcements. This provides a ready commercial source, and the high volume associated with the abrasive industry helps maintain a low cost. Silicon carbide (SiC), alumina and boron carbide (B_4C) are most often used. Titanium carbide (TiC) is also used for iron and titanium matrices. SiC offers the best strength and stiffness for an aluminum matrix, and it is used where these properties are important. Alumina is slightly cheaper than SiC, and so is attractive where cost is critical, such as in the automotive sector. Alumina is also more chemically stable than SiC and has a higher coefficient of thermal expansion (CTE), and so it is frequently used in cast DRA. Typical grit sizes used are between F-1200 (2.5 and 3.5 μm) and F-600 (8.3 to 10.3 μm).

PRMMC can be fabricated using processing techniques similar to those used for unreinforced metals making them more cost-effective. The most commonly used manufacturing processes of MMCs are infiltration casting and squeeze casting. In both cases, carefully produced porous ceramic preforms are required. Infiltration preforms of ceramic particulates are produced by either a slurry-casting approach, powder pressing or by injection molding. These preforms provide a uniform distribution of reinforcements and controlled porosity for infiltration. Nearly twice the volume of MMCs are produced by casting and other liquid routes compared to solid state fabrication, as is evident in automotive applications such as engine block cylinder liners and brake components as well as in thermal management industry. Notable examples of squeeze-cast components, as introduced by Toyota Motor Manufacturing in 1983, are the selectively reinforced MMC pistons as the first MMC application in the automotive industry. Squeeze-cast MMC piston liners have been used in the Honda Prelude since 1990 replacing cast iron inserts. Benefits obtained from using cast MMC here are numerous. Selectively reinforced MMC pistons provided lower CTE than unreinforced aluminum enabling the use of stricter tolerances in engine assembly resulting in higher pressures obtained during combustion and better performance. Improved wear resistance and lower thermal conductivity enabled more of the heat generated by combustion gases to be available for producing work. MMC piston liners provide improved wear resistance thereby allowing overall liner thickness to be reduced and at the same time increasing cylinder displacement so that more power is obtained from the same overall engine weight and volume. The thermal conductivity of MMC is much higher than the cast iron liner thereby decreasing the overall operating temperature and resulting in extended engine life.

Fabrication processes for particle reinforced MMCs, as well as machining and finishing, are typically the same (with only small modifications) to the already established processes for the metalworking industry, such as extrusion, forging and rolling. Excellent dimensional tolerances and surface finish can be achieved in the extruded MMC products. In the automobile industry extruded MMCs are used in applications such as driveshafts for trucks and Chevrolet Corvette and in aerospace components such as fan exit guide vanes of Pratt and Whitney 4000 series gas turbine engines. Rolling and forging processes are also used for commercial MMC components. MMC products such as plate and sheet are both produced by rolling. Plates are used in applications such as thermal management input material, clutch plates and fuel excess doors in the aerospace industry and sheet is used primarily for aerospace components. Both casting and powder metallurgy processes are used to produce rolling preforms. For fatigue-critical applications, such as helicopter rotor blade sleeves, MMCs are usually forged, as that process provides microstructural refinement that improves fatigue response.

Replacement of iron or aluminium with the DRA in driveshafts, as in the case of Chevrolet S-10 and GMC Sonoma in 1996, produced considerable weight savings. Usually the iron driveshaft in trucks and large passenger cars were two-piece metal assembly with a central support in between. The higher specific stiffness of MMC allow a single driveshaft to be used

without the central support and requires less counterweight mass compared to steel resulting in a weight saving of as much as 9 kg.

In thermal and electronic packaging, materials require high thermal conductivity to dissipate large localized heat loads, and a low CTE to minimized thermal stresses with semiconductor and ceramic base-plate materials. Previously used materials include Kovar (Fe-Ni-Co alloy), copper-molybdenum and copper-tungsten. Aluminium MMCs such as DRA have a thermal conductivity that is nearly ten times higher than Kovar and up to 20% higher than copper-molybdenum and copper-tungsten. Replacing such materials with DRA provides a dramatic weight reduction of 60 to 80%. Fewer processing steps in comparison with Kovar and copper alloys also provide a huge benefit in commercial applications such as portable electronics in laptop computers and cellular phones. Other applications of MMCs in related industry include radio frequency packaging for microwave transmitters in commercial low-earth orbit communications satellites, as well as the commercial flip-chip packaging of computer chips [4].

1.3. Failure and mechanisms of crack initiation in PRMMCs

Despite the numerous advantages of PRMMCs and other forms of composites, these materials are generally limited in certain applications due to their poor fracture and fatigue properties under static and dynamic loading. The increasing cost of failure in high-risk applications such as aircraft structures has encouraged the need to understand the failure mechanisms that govern the material's performance and fatigue. In order for these composites to be used at their fullest potential, it is imperative that ways be found to improve their fracture and fatigue strength. To gain insight into the predominant factors that influence fracture properties and failure mechanisms, many researchers have focused their attention on determining the stress state of the constituents of the composite at the microlevel. It is understood that failure often initiates at the microlevel with the formation of microvoids and microcracks in the matrix. The microcracs and voids eventually link up to form macrocracks [4], causing substantial degradation in the mechanical properties of the composite. Extensive studies have been conducted in to the initiation of cracks with most of studies concentrating on aluminium alloy matrix and SiC reinforcement particles. Four major sources of crack initiation have been identified, however the formation of microcracks has mainly been attributed to the large internal stresses. Such high stresses often result from the differences in the elastic and thermal properties of the particulate reinforcement and matrix of the composite.

In MMCs reinforced with ceramic particles it has been observed that the fracture of reinforcement particles initiates microcracks in the surrounding matrix. Reinforcement particles are typically very brittle and tend to fracture in the initial stages of fatigue producing high strain concentration at the interface with the matrix. Just as in unreinforced metals, porosity in composites initiates fatigue cracks. The size of the pores is directly related to their

effectiveness in initiating cracks. An MMC that contain large pores, due to incomplete penetration of matrix into particle clusters would typically fail as a result of fatigue crack initiation from one of these pores. Another important finding is the presence of microcracks at the end of reinforcements at the particle-matrix interface. This eventually causes decohesion of the reinforcement from the matrix. It has been identified that the predominant factor in the formation of these microcracks is stress concentration in the matrix around the reinforcement (Davidson [5]). These microcracks eventually link up to form macrocracks. The degree of the stress concentration depends on the shape, size and elastic modulus of the reinforcement. The analysis of stresses within the reinforcement and the matrix allows for a more accurate prediction of the failure of a composite. Stress concentration that occurs as a result of the mismatch in elastic properties between the reinforcement and matrix is of particular interest.

From classical mechanics point of view the analysis of stress concentration due to the presence of geometric and material discontinuities (cavities, cracks, notches, inclusions and reinforcements) within the elastic bodies has been the subject of many investigations. Review articles by Sternberg [6] and Neuber and Hahn [7] cover a comprehensive literature in this field. More recent research on inclusion problems has been reviewed in the monograph by Tan [8]. The monograph provides a comprehensive coverage on stress concentration in composites.

The applicable solutions for stress concentrations have mostly been obtained for simple shape inclusions and reinforcements such as spherical and infinite cylinders. The applicable solutions for more complex shapes of general nature such as ellipsoidal are rather scarce (Prokic *et al.* [9]). With increasing complexities of geometry and loading conditions considered, obtaining analytical solutions present greater difficulties. Mostly they lead to rather complex and often unsolvable integrations that cannot provide the usable expressions for stresses and strains. Researchers often resort to various numerical methods to obtain stress concentration and intensity factors around more complex inclusion shapes located in infinite or semi-infinite media. Most popular techniques are finite element and boundary element methods. Using finite element analysis Wang *et al.* [10], Agarwal and Broutman [11] and Kassam *et al.* [12] studied internal stress fields in particulate-reinforced composites under static loading.

All these studies mentioned above considered static loading, where the inertia of the medium is not considered. However, under dynamic loading the inertia of the medium plays a significant role. The application of dynamic loading is done by considering displacement and stress waves that travel through the medium. On encountering the reinforcements, these waves are reflected, refracted and scattered, giving rise to a complex stress pattern. Often the result is a high elevation of local stresses around the reinforcement. Pao and Mow [13] give a comprehensive coverage of this and other related subjects. By using a two dimensional model Bogan and Hinders [14] presented results on dynamic stress concentration for continuously reinforced fibre composite. The dynamic stress fields around rigid spherical inclusions in three dimensions have been studied by Ying and Truell [15],

Bostrom [16] and Shindo *el al.* [17]. In the case of elastic inclusion, the dynamic stress field around the spherical solid due to a plane longitudinal and shear waves has been obtained only very recently by Paskaramoorthy *et al.* [18, 19]. The study shows that the dynamic stresses in the matrix at the matrix-particle interface are significantly different from the static stresses. The stress values higher than the static ones occur at various incident frequencies of the plane compressional and shear wave. Elastic properties of particle and matrix have been shown to strongly influence the dynamic stresses. The largest stresses in the matrix produced at the interface between the particle and the matrix are normal stresses which generally reach maximum values up to 58% greater than corresponding static values.

The solutions described above for dynamic stress concentration are available only for simple shapes such as a sphere. For more complicated geometries encountered in practice such as wave scattering by a spheriodal discontinuity, presents greater analytical and computational difficulties. Some approximate asymptotic solutions for ellipsoidal inclusions valid at low frequencies are presented by Datta [20] and Willis [21]. For most of the complicated inhomogeneity geometries encountered in practice, as described previously, researchers resort to numerical methods.

Using the finite element method in combination with analytical procedure Paskaramoorthy *et al.* [22], Olsson *et al.* [23], and Meguid and Wang [24] studied scattering of elastic waves around three dimensional elastic spherical inclusions. With the same numerical technique Paskaramoorthy *et al.* [25] presented dynamic stress concentrations around an oblate spheroidal particle and found that the dynamic stresses in the matrix due to compressional wave could reach values up to 100 % greater than the corresponding static values. The dynamic load excitation considered was an incident plane compressional wave and an axisymethic finite element analysis with the eigenfunction expansion technique was considered.

In chapter 3 of this study the work of Paskaramoorthy *et al.* [18, 19 and 25] is extended by considering the incident plane shear wave on the three-dimensional prolate particle. Even though the geometry is axisymmetric, the loading is asymmetric rendering the problem three dimensional. As a result, all three displacement components need to be considered in the formulation rather than just the two in the axisymmetric problem studied previously [25]. In addition, in the previous study it was found that the dynamic stress concentrations could be 100% greater than the quasi-static values. However, due to the symmetric nature of the loading considered in this paper, these effects are expected to be different.

1.4. Interphase layer effects

An important fact needing consideration is the presence of interphase layer between the matrix and the reinforcement. In MMCs interphase layers in composites can occur naturally during material processing stage or one may intentionally introduce an interphase coating and

tailor its material properties to enhance the performance of composites. Although the studies mentioned previously investigate the stress field in particle-reinforced composites they ignored the interphase region between the reinforcement and matrix. For instance, ceramic reinforced aluminium, which is used for disc brakes in sports cars such as the Lotus Elise, is produced by pressureless infiltration of aluminium into a mass of ceramic particles, which is accompanied by the formation of a unique surface coating on all the reinforcing particles. In recent years, many papers have appeared in the literature and they indicate that the interphase region has a strong influence on the mechanical properties of composites (Madhukar and Drzal [26]). The understanding of the dominant role of the interphase has led many researchers to conceptualize the idea of tailoring the interphase properties in order to enhance the mechanical properties of composites. In this regard, the works of Wu and Dong [27], Ghosn and Lerch [28], Jansson and Leckie [29] and Carman *et al.* [30] are worth mentioning. These studies demonstrated that optimum interphase coatings exist to improve material performance. In all these studies, the composite was subjected to static loads where the inertia of the medium was ignored.

In chapter 4 of his thesis the potential of using interphase layers to reduce stress concentration in Silicone-Carbide/Magnesium particle-reinforced metal-matrix composites under dynamic loading has been investigated. The model of the composite considers only a single particle within an infinite matrix primarily to isolate the results from particles interacting with one another. The solution of a single particle is a good assumption for the dilute case in which inclusions are far away from each other and they do not interact. Al-Ostaz and Jasiuk [31] reported a good correlation in the static stress calculated using a two-dimensional single fibre model and a multiple randomly arranged model for a fibre volume fraction up to 23%. While such results may not hold true for a dynamic loading, it is still worthwhile considering a single particle model since it gives a basic understanding of the influence of various parameters of the composite material on the overall stress field. Moreover, it is possible to extend the results obtained from a single particle to account for multiple particles by applying Foldy's [32] theory. Such considerations are, however, beyond the scope of the present study.

An interphase layer was applied between the particle and the matrix and the contact between them was assumed to be welded. Both constant property materials and functionally graded (Lee *et al.* [33]) materials were considered for the interphase. Constant property materials were modeled as a single layer with uniform material properties throughout the thickness. Functionally graded materials were modeled with multiple layers each having a uniform material property. The stress concentrations are calculated in the matrix at the interface of the matrix and the interphase layer.

1.4. Surface/interface effects at nano-scale

Owing to the reduced coordination of the atoms at the free surface and the volume difference relative to the bulk, the free surface atoms experience the local environment differently than the atoms further away in the bulk (Cammarata [34, 35]). As a result, physical properties and constitutive relations of the material vary across the nanometers distance from the free surface into the bulk. Similarly the energy associated with the atoms at the interface of two dissimilar materials is generally different from that associated with atoms in the bulk in either of the adjoining materials. Surface/interface energy has been identified as the major factor contributing to this variation of the material behavior around the free surface or interface.

The free surface/interface effects are often neglected in the classical continuum mechanics as they are limited to only a few atomic layers compared to the relative size of the conventional engineering structures. Recent rapid development in nanotechnology made fabrication of nanostructured devices possible (thin films, nanowires, and nanotubes) whose particular mechanical properties differ from their macroscopic counterparts. Such nanostructured materials exhibit characteristic length in nanometers. Surface stresses can displace atoms from the equilibrium positions which they normally occupy in bulk macroscopic assemblies affecting the elastic properties of such nanoscale structures (Streitz *et al.* [36]). These properties are not normally noticed in macroscale.

Gurtin and Murdoch [37, 38] and Murdoch [39] first established the continuum mechanics models incorporating free surface stress. Gurtin *et al.* [40] extended the model by incorporating interface effects. The stress model assumes the nanostructure is made of bulk and the free surface both having different moduli (Shenoy [41]). The model agreed well with atomic simulations observed by Miller and Shenoy [42] and Shenoy [43].

Using surface/interface model various researchers studied size dependent properties on nanoscale. Cuenot *et al.* [44] and Jing *et al.* [45] compared the continuum model with atomic measurements of the elastic properties of silver nanowires and found that the apparent Young's modulus of the silver nanowires decreased with an increase in the diameter. The size effect has been attributed to the surface stress effect. Sharma *et al.* [46] investigated the interface stress effects on the deformation of the elastic field around spherical nano-inhomogeneity due to various loading conditions. Fang and Liu [47] analysed size dependent edge dislocations around circular nano-inhomogeneity with interface effects and Wang and Wang [48] studied surface effects on deformation around nano-circular hole.

The studies on surface effects on diffraction of elastic waves around nano-inhomogeneity however are scarce. Dynamic wave scattering around spherical cavity has been studied by Paskaramoorthy and Meguid [49]. The effects of different matrix material properties and wave frequencies on stress concentration in matrix around cavity have been investigated. Wang *et al.* [50] and Wang *et al.* [51] analysed the stress concentration around a nanosized hole due to the diffraction of plane compressional and shear waves. The investigation showed

that that surface/interface elasticity significantly affects the elastic scatting field when the cavity size is reduced to nanometers. In the case of elastic particle Paskaramoorthy *et al.* [18, 19] studied effects of particle and matrix material properties on dynamic stress concentration due to range of frequencies of pressure and shear waves. Significant difference between scattering of shear and plane compressional waves was shown. Wang *et al.* [52] investigated the interface effects on stress concentration around nanosized spherical particle subject to plane compressional wave and showed that the size effects should be taken into account.

In Chapter 5 the investigation of Paskaramoorthy *et al.* [18] has been extended by considering the effects of surface/interface elasticity on the stress concentration around a nanosized particle due to the shear wave.

2. General problem and fundamental equations

2.1. Statement of the problem

Figure 2.1 shows geometry of a single spherical inhomogeneity that can be a solid particle or a cavity, having a radius a embedded in an infinitely large matrix with *z-axis* as the symmetry axis. Spheroid is excited by time harmonic plane *P* (compressional) or *SV* (shear) waves propagating in the *xz* plane, parallel to the axis of symmetry. The inhomogeneity and matrix material is assumed to be homogeneous, linearly elastic, isotropic and fully bonded. Assuming a harmonic steady-state loading and from the theory of elasticity the displacement at any point within the medium must satisfy the equation of motion:

$$(\lambda+2\mu)\nabla(\nabla\cdot\boldsymbol{U})-\mu\nabla\times\nabla\times\boldsymbol{U}+\rho\omega^2\boldsymbol{U}=0 \qquad x\in D \tag{2.1}$$

where vector $\boldsymbol{x}$ is the position vector, ρ is the density, and λ and μ are Lame's constants of the medium. The displacement vector $\boldsymbol{U}=(u_R,u_\phi,u_\theta)$ satisfies Navier's equations of motion of dynamic elasticity with zero body forces.

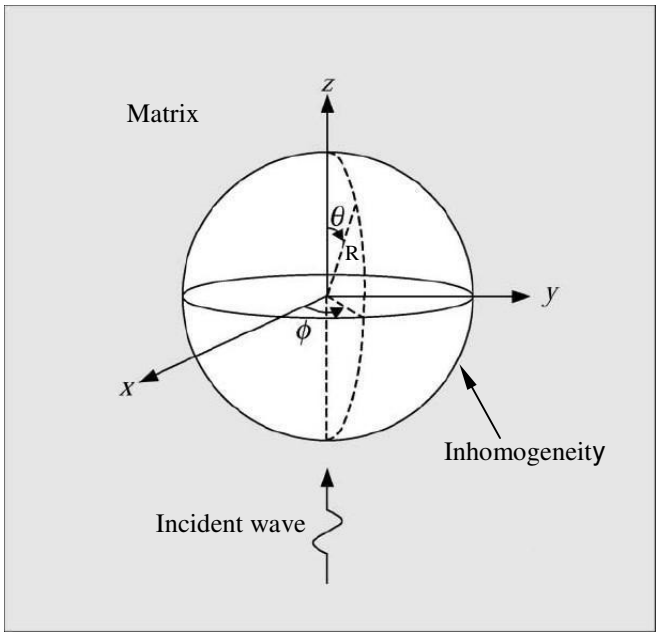

Figure 2.1 Schematic illustration of the general problem.

The solution of the equation (2.1) in terms of stress potentials χ, φ and ψ may be written in spherical coordinates as:

$$\boldsymbol{U} = \nabla\chi + \frac{1}{\beta}\nabla\times\nabla(R\psi)\times e_R + \nabla(R\varphi)\times e_R \tag{2.2}$$

where:

$$\chi(R,\phi,\theta) = \sum_{m=0}^{\infty}\sum_{n=m}^{\infty} a_{1nm} Z_n(\alpha R) P_n^m(\cos\theta)\cos m\phi \; e^{-i\omega t} \tag{2.3}$$

$$\psi(R,\phi,\theta) = \sum_{m=0}^{\infty}\sum_{n=m}^{\infty} a_{2nm} Z_n(\beta R) P_n^m(\cos\theta)\cos m\phi \; e^{-i\omega t} \tag{2.4}$$

$$\varphi(R,\phi,\theta) = \sum_{m=0}^{\infty}\sum_{n=m}^{\infty} a_{3nm} Z_n(\beta R) P_n^m(\cos\theta)\sin m\phi \; e^{-i\omega t} \tag{2.5}$$

Here m represents the azimuthal harmonic number, $i = \sqrt{-1}$, a_{1nm}, a_{2nm} and a_{3nm} are unknown amplitude coefficients, Z_n is the appropriate Bessel (j_n, y_n) or spherical Henkel function ($h_n^{(1)}$ or $h_n^{(2)}$) of order n. $P_n^m(\cos\theta)$ is the associated Legendre function of the first kind of degree n and order m and α and β are wave numbers defined by

$$\alpha^2 = \frac{\omega^2\rho}{(\lambda+2\mu)}; \quad \beta^2 = \frac{\omega^2\rho}{\mu}; \tag{2.6}$$

Only time-harmonic excitation is considered. Thus, all the field quantities have time dependence $e^{-i\omega t}$, where ω is the frequency of excitation. The time dependence is suppressed in all the subsequent representations for notational convenience.

The potential χ and potentials ψ and φ represent the pressure and shear waves respectively and they satisfy the following equations:

$$\nabla^2\chi + \alpha^2\chi = 0 \tag{2.7}$$

$$\nabla^2\psi + \beta^2\psi = 0 \tag{2.8}$$

$$\nabla^2\varphi + \beta^2\varphi = 0 \tag{2.9}$$

By simply substituting equations (2.3) to (2.5) into (2.2) the following expression for displacements in spherical coordinates is obtained:

$$u_R = \sum_{m=0}^{\infty}\sum_{n=m}^{\infty} \overline{u}_R^n \cos m\phi \tag{2.10}$$

$$u_\theta = \sum_{m=0}^{\infty}\sum_{n=m}^{\infty} \overline{u}_\theta^n \cos m\phi \tag{2.11}$$

$$u_\phi = \sum_{m=0}^{\infty}\sum_{n=m}^{\infty} -\overline{u}_\phi^n \sin m\phi \tag{2.12}$$

where the over-bar denotes amplitude of the displacement components which are given by:

$$\bar{u}_R^n = a_{1nm}\left[\frac{n}{R}Z_n(\alpha R) - \alpha Z_{n+1}(\alpha R)\right]P_n^m + a_{2nm}n(n+1)\frac{Z_n(\beta R)}{\beta R}P_n^m \tag{2.13}$$

$$\bar{u}_\theta^n = a_{1nm}\frac{Z_n(\alpha R)}{R}\frac{dP_n^m}{d\theta} + a_{2nm}\left[(n+1)\frac{Z_n(\beta R)}{\beta R} - Z_{n+1}(\beta R)\right]\frac{dP_n^m}{d\theta} + a_{3nm}mZ_n(\beta R)\frac{P_n^m}{\sin\theta} \tag{2.14}$$

$$\bar{u}_\phi^n = a_{1nm}\frac{Z_n(\alpha R)}{R}\frac{P_n^m}{\sin\theta} + a_{2nm}\left[(n+1)\frac{Z_n(\beta R)}{\beta R} - Z_{n+1}(\beta R)\right]\frac{P_n^m}{\sin\theta} + a_{3nm}mZ_n(\beta R)\frac{dP_n^m}{d\theta} \tag{2.15}$$

In the above and the equations that follow, the argument (cosθ) for P_n^m and its derivatives has been suppressed for notational convenience.

The strain-displacement relations in the spherical coordinate system may be written as:

$$\varepsilon_{RR} = \frac{\partial u_R}{\partial R} \tag{2.16}$$

$$\varepsilon_{\theta\theta} = \frac{1}{R}\frac{\partial u_\theta}{\partial\theta} + \frac{u_R}{R} \tag{2.17}$$

$$\varepsilon_{\phi\phi} = \frac{1}{R\sin\theta}\left(\frac{\partial u_\phi}{\partial\phi} + u_R\sin\theta + u_\theta\cos\theta\right) \tag{2.18}$$

$$2\varepsilon_{R\theta} = \frac{\partial u_\theta}{\partial R} + \frac{1}{R}\left(\frac{\partial u_R}{\partial\theta} - u_\theta\right) \tag{2.19}$$

$$2\varepsilon_{\theta\phi} = \frac{1}{R}\frac{\partial u_\phi}{\partial\theta} + \frac{1}{R\sin\theta}\left(\frac{\partial u_\theta}{\partial\varphi} - u_\phi\cos\theta\right) \tag{2.20}$$

$$2\varepsilon_{R\phi} = \frac{\partial u_\phi}{\partial R} + \frac{1}{R\sin\theta}\left(\frac{\partial u_R}{\partial\varphi} - u_\phi\sin\theta\right) \tag{2.21}$$

The Stress-strain relations as:

$$\sigma_{RR} = \lambda\varepsilon + 2\mu\varepsilon_{RR} \tag{2.22}$$

$$\sigma_{\theta\theta} = \lambda\varepsilon + 2\mu\varepsilon_{\theta\theta} \tag{2.23}$$

$$\sigma_{\phi\phi} = \lambda\varepsilon + 2\mu\varepsilon_{\phi\phi} \tag{2.24}$$

$$\sigma_{R\theta} = 2\mu\varepsilon_{R\theta} \tag{2.25}$$

$$\sigma_{\theta\phi} = 2\mu\varepsilon_{\theta\phi} \tag{2.26}$$

$$\sigma_{R\phi} = 2\mu\varepsilon_{R\phi} \tag{2.27}$$

$$\varepsilon = \varepsilon_{RR} + \varepsilon_{\theta\theta} + \varepsilon_{\phi\phi} \tag{2.28}$$

$$\varepsilon = \frac{1}{R^2}\frac{\partial\left(R^2u_R\right)}{\partial R} + \frac{1}{R\sin\theta}\frac{\partial\left(u_\theta\sin\theta\right)}{\partial\theta} + \frac{1}{R\sin\theta}\frac{\partial u_\phi}{\partial\phi} \tag{2.29}$$

The stress-displacement relations can now be written, taking the linear elastic constitutive law of each medium into consideration as:

$$\sigma_{RR} = \lambda\varepsilon + 2\mu\frac{\partial u_R}{\partial R} \tag{2.30}$$

$$\sigma_{\theta\theta} = \lambda\varepsilon + 2\mu\left(\frac{1}{R}\frac{\partial u_\theta}{\partial\theta} + \frac{u_R}{R}\right) \tag{2.31}$$

$$\sigma_{\phi\phi} = \lambda\varepsilon + 2\mu\left(\frac{u_R}{R} + \cot\theta\frac{u_\theta}{R} + \frac{1}{R\sin\theta}\frac{\partial u_\phi}{\partial\phi}\right) \tag{2.32}$$

$$\sigma_{R\theta} = 2\mu\left(\frac{1}{R}\frac{\partial u_R}{\partial\theta} + \frac{\partial u_\theta}{\partial R} - \frac{u_\theta}{R}\right) \tag{2.33}$$

$$\sigma_{\theta\phi} = 2\mu\left(\frac{1}{R}\frac{\partial u_\phi}{\partial\theta} + \frac{1}{R\sin\theta}\frac{\partial u_\theta}{\partial\phi} - \frac{u_\phi\cos\theta}{R\sin\theta}\right) \tag{2.34}$$

$$\sigma_{R\phi} = 2\mu\left(\frac{\partial u_\phi}{\partial R} + \frac{1}{R\sin\theta}\frac{\partial u_R}{\partial\phi} - \frac{u_\phi}{R}\right) \tag{2.35}$$

Substitution of the displacement expressions from equations (2.10) to (2.12) in to equations (2.30) to (2.35) the expressions for stresses in spherical coordinates are obtained as:

$$\sigma_{RR} = \sum_{m=0}^{\infty}\sum_{n=m}^{\infty}\bar{\sigma}_{RR}^{n}\cos m\phi \tag{2.36}$$

$$\sigma_{\theta\theta} = \sum_{m=0}^{\infty}\sum_{n=m}^{\infty}\bar{\sigma}_{\theta\theta}^{n}\cos m\phi \tag{2.37}$$

$$\sigma_{\phi\phi} = \sum_{m=0}^{\infty}\sum_{n=m}^{\infty}\bar{\sigma}_{\phi\phi}^{n}\cos m\phi \tag{2.38}$$

$$\sigma_{R\theta} = \sum_{m=0}^{\infty}\sum_{n=m}^{\infty}\bar{\sigma}_{R\theta}^{n}\cos m\phi \tag{2.39}$$

$$\sigma_{R\phi} = \sum_{m=0}^{\infty}\sum_{n=m}^{\infty}-\bar{\sigma}_{R\phi}^{n}\sin m\phi \tag{2.40}$$

$$\sigma_{\theta\phi} = \sum_{m=0}^{\infty}\sum_{n=m}^{\infty}-\bar{\sigma}_{\theta\phi}^{n}\sin m\phi \tag{2.41}$$

where

$$\begin{aligned}\bar{\sigma}_{RR}^{n} = {} & a_{1nm}\frac{2\mu}{R^2}\left[\left(n^2 - n - \frac{1}{2}\beta^2R^2\right)Z_n(\alpha R) + 2\alpha RZ_{n+1}(\alpha R)\right]P_n^m \\ & + a_{2nm}\frac{2\mu}{R^2}\frac{n(n+1)}{\beta}\left[(n-1)Z_n(\beta R) - \beta RZ_{n+1}(\beta R)\right]P_n^m\end{aligned} \tag{2.42}$$

$$\begin{aligned}\bar{\sigma}^n_{R\theta} &= a_{1nm}\frac{2\mu}{R^2}\left[(n-1)Z_n(\alpha R)-\alpha R Z_{n+1}(\alpha R)\right]\frac{dP_n^m}{d\theta}\\ &+ a_{2nm}\frac{2\mu}{R^2}\frac{1}{\beta}\left[\left(n^2-n-\frac{1}{2}\beta^2R^2\right)Z_n(\beta R)+\beta R Z_{n+1}(\beta R)\right]\frac{dP_n^m}{d\theta}\\ &+ a_{3nm}m\frac{\mu}{R}\left[(n-1)Z_n(\beta R)-\beta R Z_{n+1}(\beta R)\right]\frac{P_n^m}{\sin\theta}\end{aligned} \tag{2.43}$$

$$\begin{aligned}\bar{\sigma}^n_{R\phi} &= a_{1nm}\frac{2\mu}{R^2}m\left[(n-1)Z_n(\alpha R)-\alpha R Z_{n+1}(\alpha R)\right]\frac{P_n^m}{\sin\theta}\\ &+ a_{2nm}\frac{2\mu}{R^2}\frac{m}{\beta}\left[\left(n^2-n-\frac{1}{2}\beta^2R^2\right)Z_n(\beta R)+\beta R Z_{n+1}(\beta R)\right]\frac{P_n^m}{\sin\theta}\\ &+ a_{3nm}\frac{\mu}{R}\left[(n-1)Z_n(\beta R)-\beta R Z_{n+1}(\beta R)\right]\frac{dP_n^m}{d\theta}\end{aligned} \tag{2.44}$$

$$\begin{aligned}\bar{\sigma}^n_{\theta\phi} &= a_{1nm}\frac{2\mu}{R^2}\frac{m}{\sin^2\theta}Z_n(\alpha R)\left[(n-1)\cos\theta P_n^m-(n+m)P_{n-1}^m\right]\\ &+ a_{2nm}\frac{2\mu}{R^2}\frac{m}{\beta}\frac{1}{\sin^2\theta}\left[(n+1)Z_n(\beta R)-\beta R Z_{n+1}(\beta R)\right]\left[(n-1)\cos\theta P_n^m-(n+m)P_{n-1}^m\right]\\ &+ a_{3nm}\frac{2\mu}{R}\frac{1}{\sin^2\theta}Z_n(\beta R)\left[\left(m^2-n-\frac{1}{2}n(n-1)\sin^2\theta\right)P_n^m+(n+m)\cos\theta P_{n-1}^m\right]\end{aligned} \tag{2.45}$$

$$\begin{aligned}\bar{\sigma}^n_{\phi\phi} &= a_{1nm}\frac{2\mu}{R^2}\left[\left\{\left(n+\alpha^2R^2-\frac{1}{2}\beta^2R^2\right)Z_n(\alpha R)-\alpha R Z_{n+1}(\alpha R)\right\}P_n^m+Z_n(\alpha R)\left(\cot\theta\frac{dP_n^m}{d\theta}-\frac{m^2}{\sin^2\theta}P_n^m\right)\right]\\ &+ a_{2nm}\frac{2\mu}{R^2}\frac{1}{\beta}\left[n(n+1)Z_n(\beta R)P_n^m+\left\{(n+1)Z_n(\beta R)-\beta R Z_{n+1}(\beta R)\right\}\left(\cot\theta\frac{dP_n^m}{d\theta}-\frac{m^2}{\sin^2\theta}P_n^m\right)\right]\\ &+ a_{3nm}\frac{2\mu}{R}\left[mZ_n(\beta R)\frac{1}{\sin\theta}\left(\cot\theta P_n^m-\frac{dP_n^m}{d\theta}\right)\right]\end{aligned} \tag{2.46}$$

$$\begin{aligned}\bar{\sigma}^n_{\theta\theta} &= a_{1nm}\frac{2\mu}{R^2}\left[\left\{\left(n+\alpha^2R^2-\frac{1}{2}\beta^2R^2\right)Z_n(\alpha R)-\alpha R Z_{n+1}(\alpha R)\right\}P_n^m+Z_n(\alpha R)\frac{d^2P_n^m}{d\theta^2}\right]\\ &+ a_{2nm}\frac{2\mu}{R^2}\frac{1}{\beta}\left[n(n+1)Z_n(\beta R)P_n^m+\left\{(n+1)Z_n(\beta R)-\beta R Z_{n+1}(\beta R)\right\}\frac{d^2P_n^m}{d\theta^2}\right]\\ &+ a_{3nm}\frac{2\mu}{R}\left[mZ_n(\beta R)\frac{1}{\sin\theta}\frac{d}{d\theta}\left(\frac{P_n^m}{\sin\theta}\right)\right]\end{aligned} \tag{2.47}$$

Presented here is a general theory in which a quantity of interest is calculated for each harmonic m. However, when the angle of incidence α is zero, only one harmonic number in equations (2.3) to (2.5) needs to be considered, namely $m = 0$ for incidence P wave and $m = 1$ for incident SV wave. The degenerate and the general cases of incidence are discussed in subsequent sections where particular problems are presented and solved.

3. Stress concentration in matrix around spheroidal particle under asymmetric dynamic loading

This investigation considers the incident plane shear wave on the three-dimensional spheroid prolate elastic solid. For simplicity, the effect of the interaction of neighbouring particles is ignored and the results are therefore valid for low volume fraction of particles. Figure 3.1a shows the geometry of a single prolate spheroidal particle having $b/a > 1$ embedded in an infinitely large matrix. *z-axis* is the symmetry axis, a and b are dimensions of the inclusion along x and z axis respectively. The spheroid is excited by time harmonic plane *SV* waves propagating in the xz plane, parallel to the axis of symmetry. In solving the problem a fictitious spherical boundary B is drawn so that it encloses the particle and a finite region of the elastic medium. The interior region between the particle and the boundary B is modelled by using an assembly of finite elements and the solution in the exterior region is represented by spherical wave functions. By imposing the continuity of the displacements and traction forces on the boundary B, between the interior and exterior regions, the model yields the displacements for the nodes lying on the boundary. This in turn yields both the displacements of the interior nodes and the unknown coefficients associated with the spherical wave functions.

The surface of the particle, denoted by S, may be defined by

$$\frac{x^2}{a^2}+\frac{y^2}{a^2}+\frac{z^2}{b^2}=1 \tag{3.1}$$

The domain of the medium is denoted by D. The material is assumed to be homogeneous, linearly elastic and isotropic. Only time-harmonic excitation is considered. Thus, all the field quantities have a time dependence $e^{-i\omega t}$, where ω is the frequency of excitation.

The equation of motion of the domain D for the steady state is specified by equation (2.1). The boundary conditions on the surface S of the particle are of the form

$$\sigma_{ij} n_j = 0 \qquad x \in S \tag{3.2}$$

where n is the unit normal vector to the surface S and the summation convention for repeated indices is assumed. A solution of equation (2.1) satisfying equation (3.2) is sought. In addition, the solution should be regular at infinity.

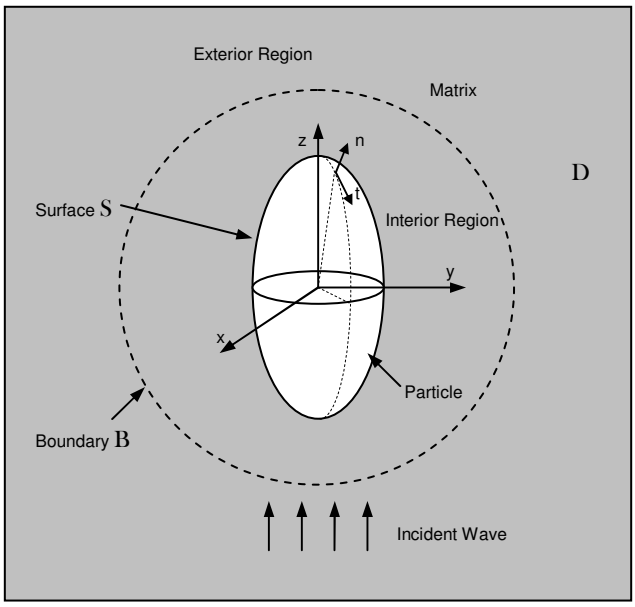

a. Schematic of the problem

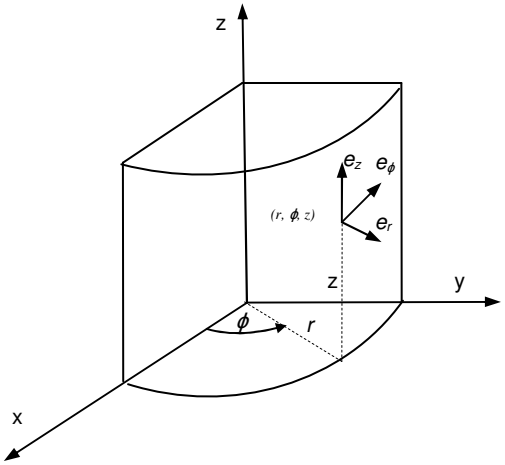

b. Cylindrical coordinate system

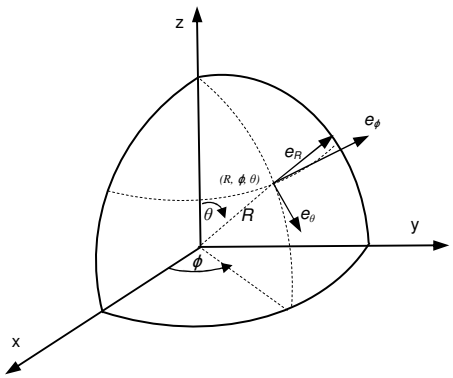

c. Spherical coordinate system

Figure 3.1 Problem geometry with cylindrical and spherical coordinate systems.

3.1. Formulation of the problem

3.1.1. Interior region

The interior region contains the particle and a small portion of the surrounding matrix. This region is modelled by using 8-noded isoparametric finite elements. A typical finite element mesh is shown in figure 3.2 where the mid-side and interior nodes are omitted for clarity. The formulation is presented in the cylindrical coordinate system (r, ϕ, z) shown in figure 3.1b. In the analysis of axisymmetric bodies subjected to non-axisymmetric loadings, both loads and displacements are expanded in Fourier series in the circumferential direction. For instance, the displacement components may be written, in cylindrical coordinate system, as

$$u_r(r,\phi,z,t) = \sum_{m=0}^{\infty}\left[\bar{u}_{rm}(r,z)\cos m\phi + \hat{u}_{rm}(r,z)\sin m\phi\right]e^{-i\omega t} \tag{3.3}$$

$$u_z(r,\phi,z,t) = \sum_{m=0}^{\infty}\left[\bar{u}_{zm}(r,z)\cos m\phi + \hat{u}_{zm}(r,z)\sin m\phi\right]e^{-i\omega t} \tag{3.4}$$

$$u_\phi(r,\phi,z,t) = \sum_{m=0}^{\infty}\left[-\bar{u}_{\phi m}(r,z)\sin m\phi + \hat{u}_{\phi m}(r,z)\cos m\phi\right]e^{-i\omega t} \tag{3.5}$$

where $i=\sqrt{-1}$, the overbar denotes amplitude of the displacement components symmetric about the $\phi=0$ axis, the hat denotes the antisymmetric components and m is the circumferential harmonic number. The negative sign before $\bar{u}_{\phi m}(r,z)$ has the effect of giving identical stiffness matrices for both symmetric and antisymmetric components. The primary unknowns in this formulation are amplitudes of the displacement components which are functions of r and z only and do not depend upon ϕ. Since the polarization of the incident wave is in the xz-plane, the resulting loading will be symmetric about $\phi=0$. Consequently, only the symmetric part of the displacement components is used. This study considers only the case of incident wave propagating along the z-axis with polarization along the x-axis. This results in further simplification in that only one harmonic number, namely m = 1, survives. Consequently, the displacement field can be written as

$$u_r(r,\phi,z,t) = \bar{u}_r(r,z)\cos\phi\, e^{-i\omega t} \tag{3.6}$$

$$u_z(r,\phi,z,t) = \bar{u}_z(r,z)\cos\phi\, e^{-i\omega t} \tag{3.7}$$

$$u_\phi(r,\phi,z,t) = -\bar{u}_\phi(r,z)\sin\phi\, e^{-i\omega t} \tag{3.8}$$

The amplitude of displacements within an element is interpolated from the nodal displacement amplitude as

$$\{\bar{u}\} = [N]\{\bar{q}\} \tag{3.9}$$

where *[N]* contains interpolation functions, $\{\bar{q}\}$ is the vector of nodal displacement amplitudes, and

$$\{\bar{u}\} = \left\langle \bar{u}_r \;\; \bar{u}_z \;\; \bar{u}_\phi \right\rangle^T \tag{3.10}$$

In the above, the superscript *T* denotes transpose. Explicit expressions for *[N]* may be found in the book by Cook et al. [53] or in many other standard reference books.

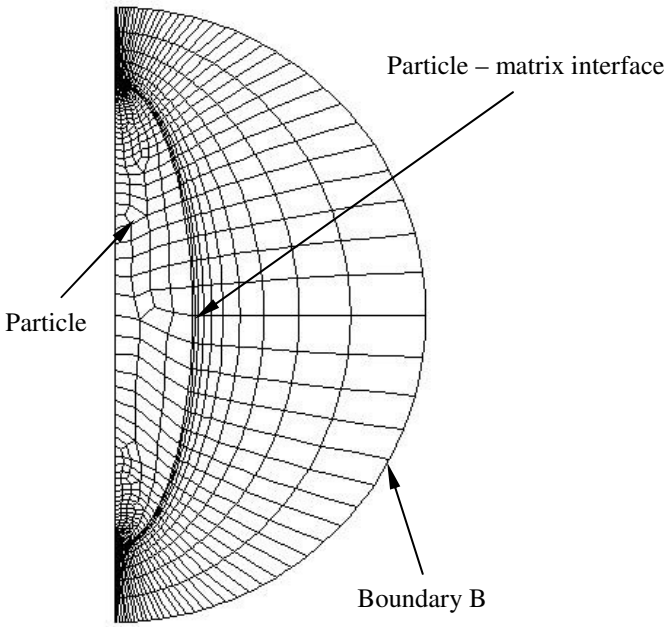

Figure 3.2 Finite element mesh of the interior region for *b/a* = 3.

The governing equation of motion, which can be obtained by following the conventional finite element methodology for axisymmetric elements subjected to non-axisymmetric loads [53], is given by:

$$[S]\{\bar{q}\} = \{\bar{P}\} \tag{3.11}$$

where

$$[S] = [K] - \omega^2 [M] \tag{3.12}$$

in which $[K]$ and $[M]$ are the respective stiffness and consistent mass matrices of the

interior region, $\{\overline{q}\}$ is the vector of nodal displacements, and $\{\overline{P}\}$ is the vector of nodal load amplitudes.

If the vector $\{\overline{q}\}$ is separated into two parts, $\{\overline{q}_B\}$ corresponding to nodal displacements at the boundary *B*, and $\{\overline{q}_I\}$ corresponding to nodal displacements elsewhere in the interior region equation (3.11) can be written as:

$$\begin{bmatrix} S_{II} & S_{IB} \\ S_{BI} & S_{BB} \end{bmatrix} \begin{Bmatrix} \overline{q}_I \\ \overline{q}_B \end{Bmatrix} = \begin{Bmatrix} 0 \\ \overline{P}_B \end{Bmatrix} \tag{3.13}$$

in which $\{\overline{P}_B\}$ represent the amplitudes of interaction forces between the interior and exterior regions.

3.1.2. Exterior region

The incident and scattered waves are denoted by the superscripts *inc* and *sct* respectively. The displacement vector **U** has contributions from both incident and scattered waves.

$$\boldsymbol{U} = \boldsymbol{U}^{inc} + \boldsymbol{U}^{sct} \tag{3.14}$$

While the incident wave field is known, the scattered wave field is unknown.

3.1.3. Incident waves

Let the incident wave be represented by the displacement field in Cartesian coordinate system as

$$\boldsymbol{U}^{inc} = e^{i\beta_1 Z - i\omega t} e_X \tag{3.15}$$

where e_x is the unit vector in *x* direction, this being the plane *SV*-wave propagating in the *z* direction, its extent covers the whole *x*-*y* plane. The displacement and stress field induced by this wave, which also occur in the absence of the solid particle, have the following explicit forms in cylindrical coordinates as in figure 3.1b:

$$u_r^{inc} = e^{i\beta_1 z}\cos\phi \;\; e^{-i\omega t} \tag{3.16}$$

$$u_\phi^{inc} = -e^{i\beta_1 z}\sin\phi\, e^{-i\omega t} \tag{3.17}$$

$$u_z^{inc} = 0 \tag{3.18}$$

$$\sigma_{rz}^{inc} = i\mu_1\beta_1\, e^{i\beta_1 z}\cos\phi \;\; e^{-i\omega t} \tag{3.19}$$

$$\sigma_{\phi z}^{inc} = -i\mu_1\beta_1\, e^{i\beta_1 z}\sin\phi\; e^{-i\omega t} \tag{3.20}$$

$$\sigma_{r\phi}^{inc} = \sigma_{rr}^{i} = \sigma_{\phi\phi}^{i} = \sigma_{zz}^{i} = 0 \tag{3.21}$$

where α and β are wave numbers defined in equation (2.6) and the subscript 1 refers to the matrix medium. It can be seen that the variation of the displacement components with respect to the angular coordinate ϕ is similar those presented in equations (3.6) to (3.8). It is obvious that the displacement and stress fields are asymmetric about the ϕ=0 axis.

The incident field can also be expanded in terms of the spherical eigenfunctions as

$$\overline{u}_R^{inc} = \sum_{n=1}^{\infty}\left[i^n \frac{2n+1}{n(n+1)}\left(-i\frac{n(n+1)}{\beta_1 R} j_n(\beta_1 R) P_n^1 \right)\right]\cos\phi \tag{3.22}$$

$$\overline{u}_\theta^{inc} = \sum_{n=1}^{\infty}\left[i^n \frac{2n+1}{n(n+1)}\left[-i\left((n+1)\frac{j_n(\beta_1 R)}{\beta_1 R} - j_{n+1}(\beta_1 R)\right)\frac{dP_n^1}{d\theta} + j_n(\beta_1 R)\frac{P_n^1}{\sin\theta}\right]\right]\cos\phi \tag{3.23}$$

$$\overline{u}_\phi^{inc} = \sum_{n=1}^{\infty}\left[i^n \frac{2n+1}{n(n+1)}\left[\;\; i\left((n+1)\frac{j_n(\beta_1 R)}{\beta_1 R} - j_{n+1}(\beta_1 R)\right)\frac{P_n^1}{\sin\theta} - j_n(\beta_1 R)\frac{dP_n^1}{d\theta}\right]\right]\sin\phi \tag{3.24}$$

For later use when satisfying the continuity conditions, an array containing the amplitudes of the nodal displacements on the boundary, $\left\{\overline{q}_B^{inc}\right\}$ can be constructed by evaluating equations (3.16) to (3.18) at each node on the boundary *B*. Similarly, an array containing the amplitudes of the nodal forces $\left\{\overline{P}_B^{inc}\right\}$ on the boundary can also be constructed from equations (3.19) to (3.21). Each of these arrays will have $3N_B$ elements.

3.1.4. Scattered waves

A solution for $\boldsymbol{U^{sct}}$ satisfying equation (2.1) and far-field radiation conditions can be written in the spherical coordinate system of figure 3.1c as [13]

$$U = \nabla\chi + \frac{1}{\beta}\nabla\times\nabla(R\psi)\times e_R + \nabla(R\varphi)\times e_R \tag{3.25}$$

where e_R is the unit vector in the R–direction and χ, ψ and φ are given by:

$$\chi^{sct}(R,\phi,\theta) = \sum a_{1n} h_n(\alpha_1 R) P_n^1(\cos\theta)\cos\phi\, e^{-i\omega t} \tag{3.26}$$

$$\psi^{sct}(R,\phi,\theta) = \sum a_{2n} h_n(\beta_1 R) P_n^1(\cos\theta)\cos\phi\, e^{-i\omega t} \tag{3.27}$$

$$\varphi^{sct}(R,\phi,\theta) = \sum a_{3n} h_n(\beta_1 R) P_n^1(\cos\theta)\sin\phi\, e^{-i\omega t} \tag{3.28}$$

In the above, and in the following, all the summations are over integral values of n from one to infinity, a_{1n}, a_{2n} and a_{3n} are as yet unknown amplitude coefficients, h_n is the spherical Hankel function of the first kind and order n. $P_n^1(\cos\theta)$ the associated Legendre function of first order and degree n.

Substituting equations (3.26) to (3.28) in to equation (3.25), we obtain

$$u_R^{sct}(R,\phi,\theta,t) = \bar{u}_R(R,\theta)\cos\phi\, e^{-i\omega t} = e^{-i\omega t}\cos\phi\sum \bar{u}_R^n \tag{3.29}$$

$$u_\theta^{sct}(R,\phi,\theta,t) = \bar{u}_\theta(R,\theta)\cos\phi\, e^{-i\omega t} = e^{-i\omega t}\cos\phi\sum \bar{u}_\theta^n \tag{3.30}$$

$$u_\phi^{sct}(R,\phi,\theta,t) = \bar{u}_\phi(R,\theta)\sin\phi\, e^{-i\omega t} = e^{-i\omega t}\sin\phi\sum \bar{u}_\phi^n \tag{3.31}$$

where

$$\bar{u}_R^n = a_{1n}\left[\frac{n}{R}h_n(\alpha_1 R) - \alpha_1 h_{n+1}(\alpha_1 R)\right]P_n^1 + a_{2n}n(n+1)\frac{h_n(\beta_1 R)}{\beta_1 R}P_n^1 \tag{3.32}$$

$$\bar{u}_\theta^n = a_{1n}\frac{h_n(\alpha_1 R)}{R}\frac{dP_n^1}{d\theta} + a_{2n}\left[(n+1)\frac{h_n(\beta_1 R)}{\beta_1 R} - h_{n+1}(\beta_1 R)\right]\frac{dP_n^1}{d\theta} + a_{3n}h_n(\beta_1 R)\frac{P_n^1}{\sin\theta} \tag{3.33}$$

$$-\bar{u}_\phi^n = a_{1n}\frac{h_n(\alpha_1 R)}{R}\frac{P_n^1}{\sin\theta} + a_{2n}\left[(n+1)\frac{h_n(\beta_1 R)}{\beta_1 R} - h_{n+1}(\beta_1 R)\right]\frac{P_n^1}{\sin\theta} + a_{3n}h_n(\beta_1 R)\frac{dP_n^1}{d\theta} \tag{3.34}$$

In the above and the equations that follow, the argument ($\cos\theta$) for P_n^1 and its derivatives has been suppressed for notational convenience.

The stress field associated with the displacements of equations (3.29) to (3.31) are given by

$$\sigma_{RR}^{sct}(R,\theta,\phi,t) = \bar{\sigma}_{RR}(R,\theta)\cos\phi\, e^{-i\omega t} \quad = e^{-i\omega t}\cos\phi\sum \bar{\sigma}_{RR}^{n} \tag{3.35}$$

$$\sigma_{R\theta}^{sct}(R,\theta,\phi,t) = \bar{\sigma}_{R\theta}(R,\theta)\cos\phi\, e^{-i\omega t} \quad = e^{-i\omega t}\cos\phi\sum \bar{\sigma}_{R\theta}^{n} \tag{3.36}$$

$$\sigma_{R\phi}^{sct}(R,\theta,\phi,t) = \bar{\sigma}_{R\phi}(R,\theta)\sin\phi\, e^{-i\omega t} \quad = e^{-i\omega t}\sin\phi\sum \bar{\sigma}_{R\phi}^{n} \tag{3.37}$$

where

$$\begin{aligned}\bar{\sigma}_{RR}^{n} &= a_{1n}\frac{2\mu_1}{R^2}\left[\left(n^2-n-\frac{1}{2}\beta_1^2R^2\right)h_n(\alpha_1R)+2\alpha_1Rh_{n+1}(\alpha_1R)\right]P_n^1 \\ &\quad + a_{2n}\frac{2\mu_1}{R^2}\frac{n(n+1)}{\beta_1}\left[(n-1)h_n(\beta_1R)-\beta_1Rh_{n+1}(\beta_1R)\right]P_n^1\end{aligned} \tag{3.38}$$

$$\begin{aligned}\bar{\sigma}_{R\theta}^{n} &= a_{1n}\frac{2\mu_1}{R^2}\left[(n-1)h_n(\alpha_1R)-\alpha_1Rh_{n+1}(\alpha_1R)\right]\frac{dP_n^1}{d\theta} \\ &\quad + a_{2n}\frac{2\mu_1}{R^2}\frac{1}{\beta}\left[\left(n^2-n-\frac{1}{2}\beta_1^2R^2\right)h_n(\beta_1R)+\beta_1Rh_{n+1}(\beta_1R)\right]\frac{dP_n^1}{d\theta} \\ &\quad + a_{3n}\frac{\mu_1}{R}\left[(n-1)h_n(\beta_1R)-\beta_1Rh_{n+1}(\beta_1R)\right]\frac{P_n^1}{\sin\theta}\end{aligned} \tag{3.39}$$

$$\begin{aligned}-\bar{\sigma}_{R\phi}^{n} &= a_{1n}\frac{2\mu_1}{R^2}\left[(n-1)h_n(\alpha_1R)-\alpha_1Rh_{n+1}(\alpha_1R)\right]\frac{P_n^1}{\sin\theta} \\ &\quad + a_{2n}\frac{2\mu_1}{R^2}\frac{1}{\beta_1}\left[\left(n^2-n-\frac{1}{2}\beta_1^2R^2\right)h_n(\beta_1R)+\beta_1Rh_{n+1}(\beta_1R)\right]\frac{P_n^1}{\sin\theta} \\ &\quad + a_{3n}\frac{\mu_1}{R}\left[(n-1)h_n(\beta_1R)-\beta_1Rh_{n+1}(\beta_1R)\right]\frac{dP_n^1}{d\theta}\end{aligned} \tag{3.40}$$

The other three stress components not shown here are not zero but they are not needed in the formulation.

Let p be the number of significant terms in equations (3.29) to (3.31), and (3.35) to (3.37). Evaluating equations (3.29) to (3.31) at each nodes lying on the boundary B, we can construct a matrix $[G]$ relating the nodal displacements to the unknown coefficients as

$$\left\{\overline{q}_B^{sct}\right\}_{sph} = [G]\{a\} \tag{3.41}$$

where $\left\{\overline{q}_B^{sct}\right\}_{sph}$ is the array of amplitude displacements, in spherical coordinates, at the nodes on the boundary B, $\{a\}$ contains the unknown coefficients a_{1n}, a_{2n} and a_{3n} with $n = 1, 2, .., p$. It can be seen that the matrix $[G]$ is complex valued. If N_B is the number of nodes on the boundary B, the $[G]$ matrix will have dimensions $3N_B$ x $3p$. Similarly a relationship between the amplitudes of the nodal forces $\left\{\overline{P}_B^{sct}\right\}_{sph}$, at the boundary B, and the unknown coefficients $\{a\}$, can be established by evaluating the stresses σ_{RR}, $\sigma_{R\theta}$ and $\sigma_{R\phi}$ at each of the nodes on the B and multiplying them by the corresponding tributary area:

$$\left\{\overline{P}_B^{sct}\right\}_{sph} = [F]\{a\} \tag{3.42}$$

A relationship between vector $\left\{\overline{P}_B^{sct}\right\}_{sph}$ and the displacement $\left\{\overline{q}_B^{sct}\right\}_{sph}$ vector can now be established by eliminating unknown coefficients $\{a\}$ from equations (3.41) and (3.42). We first write the equation (3.43) as (see Appendix A)

$$\{a\} = [H]\left\{\overline{q}_B^{sct}\right\}_{sph}; [H] = \left(\left[G^*\right]^T [G]\right)^{-1} \left[G^*\right]^T \tag{3.43}$$

Where $\left[G^*\right]$ is the complex conjugate of $[G]$. Substitution of equation (3.43) in equation (3.42) leads to

$$\left\{\overline{P}_B^{sct}\right\}_{sph} = [F][H]\left\{\overline{q}_B^{sct}\right\}_{sph} \tag{3.44}$$

In the above, $[H]$ is the generalized inverse of $[G]$. For $p \leq N_B$, the generalized inverse exists (Lancaster [54]) and the uniqueness of the operation is assured. The arrays $\left\{\overline{P}_B^{sct}\right\}_{sph}$ and $\left\{\overline{q}_B^{sct}\right\}_{sph}$ in equations (3.41) and (3.42) are in the spherical coordinate system. When they are transformed into cylindrical coordinates, equation (3.44) takes the form

$$\left\{\overline{P}_B^{sct}\right\} = \left[S_f\right]\left\{\overline{q}_B^{sct}\right\} \tag{3.45}$$

where

$$\left[S_f\right] = [T]^t [F][H][T] \tag{3.46}$$

In which $[T]$ is the transformation matrix from spherical to cylindrical coordinate system.

3.2. Global Solution

The continuity of the displacement and stresses across the boundary *B* can be imposed by setting the displacement and stresses from the interior region to be equal to those from the exterior region:

$$\{q_B\} = \left\{q_B^{inc}\right\} + \left\{q_B^{sct}\right\} \tag{3.47}$$

$$\{P_B\} = \left\{P_B^{inc}\right\} + \left\{P_B^{sct}\right\} \tag{3.48}$$

Since the ϕ variation of the displacement and force components in both interior and exterior regions are similar, equations (3.47) and (3.48) can be written in terms of the amplitudes as

$$\{\overline{q}_B\} = \left\{\overline{q}_B^{inc}\right\} + \left\{\overline{q}_B^{sct}\right\} \tag{3.49}$$

$$\left\{\overline{P}_B\right\} = \left\{\overline{P}_B^{inc}\right\} + \left\{\overline{P}_B^{sct}\right\} \tag{3.50}$$

In view of equations (3.49), (3.50) and (3.45), equation (3.13) takes the form

$$\begin{bmatrix} S_{II} & S_{IB} \\ S_{BI} & S_{BB} - S_f \end{bmatrix} \begin{Bmatrix} \overline{q}_I \\ \overline{q}_B \end{Bmatrix} = \begin{Bmatrix} 0 \\ \overline{P}_B^{inc} - S_f \overline{q}_B^{inc} \end{Bmatrix} \tag{3.51}$$

Once the above equation is solved for the nodal displacements, the stress field in the interior region can be obtained from conventional procedures used in finite element analysis.

3.3. Numerical results and discussion

The actual number of spherical functions required to construct a scattered field solution in the exterior region (equation (3.41)) is determined by conducting numerical experiments on the convergence of the solution. In this study a finite number of wave functions have been considered that was sufficient for the convergence of the solution, since the contribution of the higher-order terms of the infinite series in equation (3.41) and in other equations is small. The spherical wave functions should be taken in sequence so that no preference is given to a higher-order spherical function at the omission of a lower-order function. More details may be found in the excellent article by Dong [55] that reviews the hybrid method in its generality and addresses issues related to convergence, completeness and uniqueness of the solution.

The dynamic excitation is provided by an incident *SV*-wave defined by equation (3.15). In the absence of the particle, the stress field at any point in the medium can be expressed in rectangular coordinates as

$$\sigma_{xz} = \sigma_{zx} = i\mu_1\beta_1 e^{i\beta_1 z - i\omega t} \tag{3.52}$$

With all other stress components being zero the maximum value of the stresses is $\mu_1\beta_1$. In the presence of the particle, the stress field is significantly different from that given by equation (3.52) due to scattering. The nonzero stresses on the surface of the particle are $\sigma_{tt}, \sigma_{\phi\phi}$ and $\sigma_{t\phi}$ where *t* is the tangential vector on the surface of particle as shown in figure 3.1a. The results have the general form

$$\sigma = (R + iI) f(\phi) e^{-i\omega t} \tag{3.53}$$

Where $f(\phi)$ is either $\cos\phi$ or $\sin\phi$, the real part *R* represents the solution at $t = 0$ and $T/2$, and the imaginary part *I* represents the solution at $t = T/4$ and $3T/4$, T being the period of excitation. The absolute value $(R^2 + I^2)^{1/2}$ is the maximum stress that occurs at some instant depending on the phase-shift.

These stresses are expressed in dimensionless form by normalizing with respect to the maximum value of the incident stress field, $\mu_1\beta_1$:

$$\sigma_{ij}^* = \frac{|\sigma_{ij}|}{\mu_1\beta_1} \qquad i, j = t, \phi \tag{3.54}$$

Thus the values of σ_{ij}^* can be considered as dynamic stress concentration factors. They depend on the aspect ratio of the particle and the frequency of excitation. In addition they

also depend on shear moduli μ_1 and μ_2, Poisson's ratios v_1 and v_2, and mass densities ρ_1 and ρ_2 of the particle and matrix. The frequency is expressed in non-dimensional form through

$$\omega^* = \omega a \sqrt{\frac{\rho_1}{\mu_1}} \tag{3.55}$$

where a, as defined earlier, is the radius of the particle in the x-y plane. In addition, the shear modulus and density of the particle are expressed in nondimensional form through

$$\mu^* = \frac{\mu_2}{\mu_1} \quad ; \quad \rho^* = \frac{\rho_2}{\rho_1} \tag{3.56}$$

The following values of the parameters have been chosen for the computation:

$\mu^* = 2, 4, 8, 12$
$v_2, v_1 = 0.15, 0.25, 0.30, 0.35, 0.45$
$\rho^* = 0.5, 1, 2, 5$

The values are sufficient to cover the range of parameters which might be encountered in practical application [56, 57, 58, 59]. For instance, the ratio of shear moduli $\mu^* = \mu_2 / \mu_1$ is close to 8 for the case of a SiC particle embedded in an Al matrix.

The nature of the dynamic excitation is better appreciated by considering the limiting static case. When the frequency approaches zero, the applied stress field at infinity approaches

$$\sigma_{xz} = \sigma_{zx} = \sigma_0 \tag{3.57}$$

$$\sigma_{xx} = \sigma_{yy} = \sigma_{zz} = \sigma_{xy} = \sigma_{yz} \tag{3.58}$$

where σ_0 is a constant. The stress field of equations (3.57) and (3.58) is pure shear. Thus, the results presented herein are for the dynamic counterpart of this shear load.
For the spherical particle analytical solutions are available which are used to assess the accuracy of the numerical procedure. Figures 3.3 and 3.4 compare the nondimensional stress concentration values of stresses σ^*_{RR}, $\sigma^*_{R\theta}$ and $\sigma^*_{R\phi}$ on the surface of a spherical particle of radius a obtained by the numerical method against the analytical solution. For the two representative values of dimensionless frequency 0.01 and 3.0, agreement between the analytical and numerical results can be seen to be excellent. Other stress concentration values on the particle and matrix interface are lower than one and therefore not shown. At low dimensionless frequencies of 0.01 (figure 3.3) there is little dynamic effect present and the dynamic solution is hardly different from the corresponding static solution. The stress distributions also display symmetry about the xy-plane, as expected. For the normalized frequency of 3.0 the wavelength is about the same size as the diameter of the particle and a great deal of

scattering occurs (figure 3.4) which results in a stress distribution being quite different from the quasi-static solution.

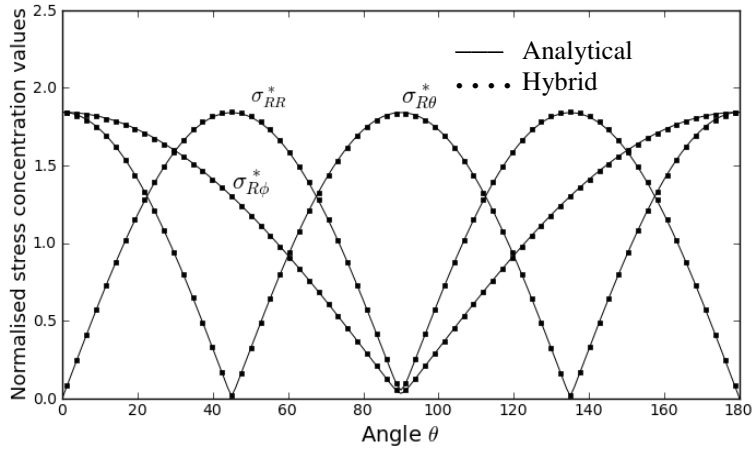

Figure 3.3 Comparison of stress concentration values along the circumference of a spherical particle for $\omega^* = 0.01$(ρ^*=1, μ^*=8, $\nu_1 = \nu_2$=0.3)

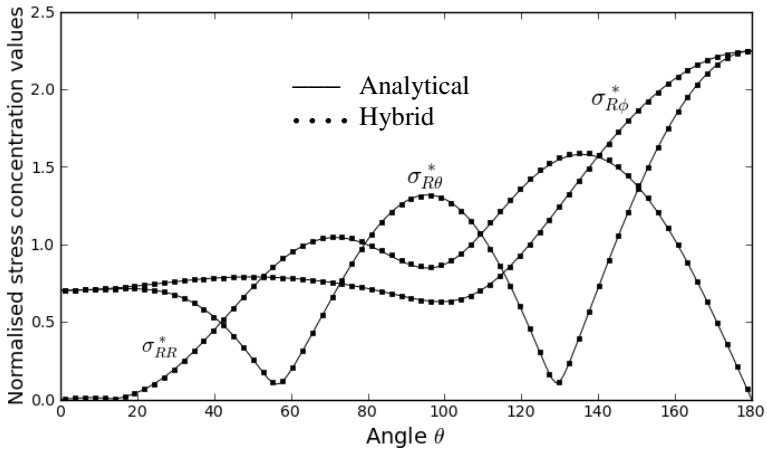

Figure 3.4 Comparison of stress concentration values along the circumference of a spherical particle for $\omega^* = 3$ (ρ^*=1, μ^*=8, $\nu_1 = \nu_2$=0.3)

A separate static analysis for sheroidal particle of *b/a*=3 (figure 3.5) and *b/a*=5 (figure 3.6) confirmed that the solution corresponding to the loads given by equations (3.56) and (3.57) agree with the dynamic solutions of a hybrid model. The finite element mesh for the static analysis used in figures 3.5 and 3.6 is shown in Appendix C figures C.1 and C.2. The solutions obtained by the hybrid method shown in figures 3.3 and 3.4 exhibit a very high level of accuracy. In general, the fineness of the finite element mesh and the number of wave functions *p* considered in equations (3.41) and (3.42) are two primary factors that influence

the accuracy of the solution. As in any finite element analysis, the fineness of the mesh must be gradually increased until convergence is reached. As for the number of wave functions p, it must be sufficiently large to guarantee the convergence of the series in equations (3.29) to (3.31) and (3.35) to (3.37). A simple strategy to satisfy the requirements is set p equal to N_B and gradually refine the mesh which, in turn, increases both N_B and p. While this worked well for low frequencies, numerical underflow and overflow problems were encountered at high frequencies. The numerical instability was caused by the magnitudes of Bessel and Hankel functions since, for p number of wave functions, the highest order of Bessel and Hankel functions to be evaluated is p+1 and the magnitudes of these functions increases at a rapid rate with the order. As a result, the magnitudes of the terms in the $[S]$ matrix of equation (3.11) and $[S_f]$ matrix in equation (3.45) differed by several orders which, in turn, rendered the matrix on the left side of equation (3.51) ill conditioned. Use of a matrix conditioning scheme such as diagonal scaling offered only a slight improvement to the situation. The recommendation is to start with $p = N_B/2$ and gradually refine the mesh. This worked well for all frequencies. The location of boundary B also affects the accuracy of the solution. The radius of this boundary, R_B, should be large enough to completely enclose the particle. However, a very large R_B is undesirable since the arguments of the Bessel and Hankel functions increase linearly with R_B and the algorithms available to calculate Bessel and Hankel functions become moderately less accurate for large arguments. It is therefore recommended that R_B be kept in the range of 1:1b –1:5b, where b is the larger semi-axis of the particle.

Figures 3.7, 3.8 and 3.9 illustrate the angular distribution of $\sigma^*_{nn}, \sigma^*_{n\phi}$ and σ^*_{nt} for both spherical and spheroidal particle for five different normalized frequencies. The small figures to the right of the main ones in figure 3.9 better illustrate the variation of stress around $\theta = 180^\circ$ which is the incident side of the particle. In these figures, the subscripts n and t refer to the normal and tangential directions, respectively, as shown in figure 3.1. For spherical particle $\sigma^*_{nn} = \sigma^*_{RR}$, $\sigma^*_{n\phi} = \sigma^*_{R\phi}$ and $\sigma^*_{nt} = \sigma^*_{R\theta}$. Other stress components are not shown here since their computed values turned out to be less than 1 for every frequency in the range $0 < \omega^* < 3$. It can be seen that both the nondimensional frequency and the aspect ratio b/a of the particle have a significant influence on the stress distribution. In addition, a simple consideration of the asymmetric nature of loading and the axisymmetric geometry of particle suggests that, at $\theta = 180^\circ$, $\sigma^*_{n\phi}$ must be equal to σ^*_{nt}. The results presented in figures 3.7 to 3.9 show that this is indeed the case. At a very small normalized frequency of 0.01 hardly any dynamic effect is expected. The dynamic solution can be regarded as quasi-static and dynamic load is given approximately by equations (3.57) and (3.58) which exhibit symmetry with respect to the $z = 0$ plane. As seen in figures 3.7 to 3.9 the resulting stress field is also symmetric about this plane for all aspect ratios. For $b/a = 1$ the maximum values of σ^*_{nn} occur at 45° and 135°, that of $\sigma^*_{n\phi}$ occur at 0° and 180° and for σ^*_{nt} occur at 0°, 90° and 180°. As the particle aspect ratio increases the position of these maximum stresses concentration values moves progressively towards the poles. For clarity reasons, a

narrow range of every graph in figure 3.9 have been shown to the right of every stress plot to better portray the behavior at peak values.

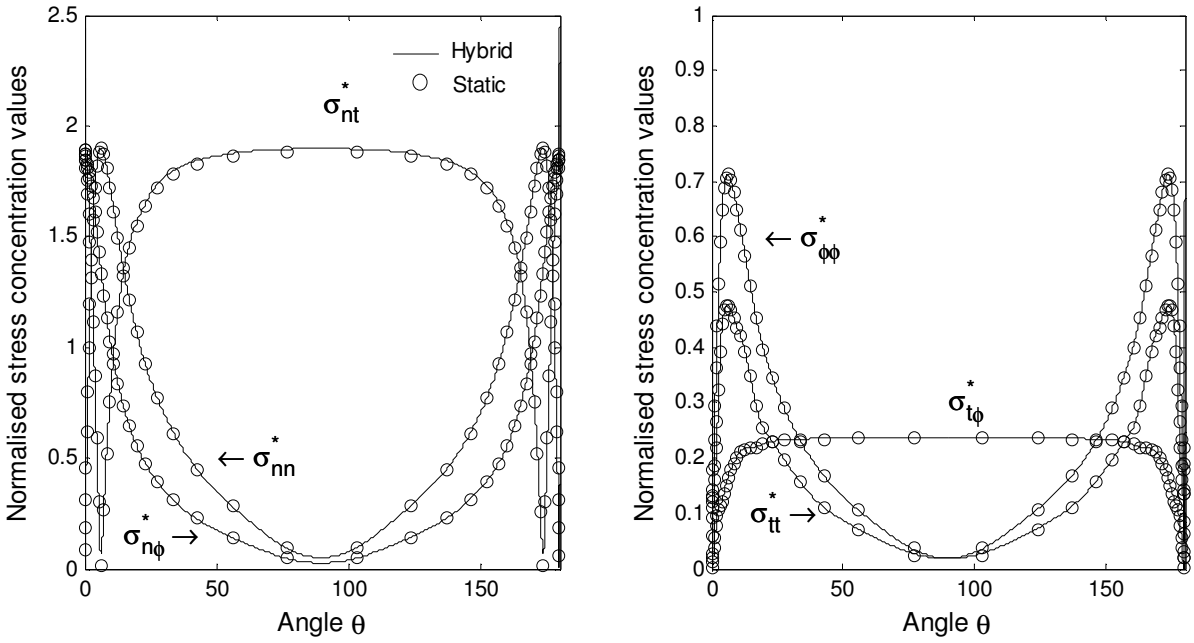

Figure 3.5 Comparison of stresses along the circumference of a spheroidal particle of *b/a*=3 subject to static loading

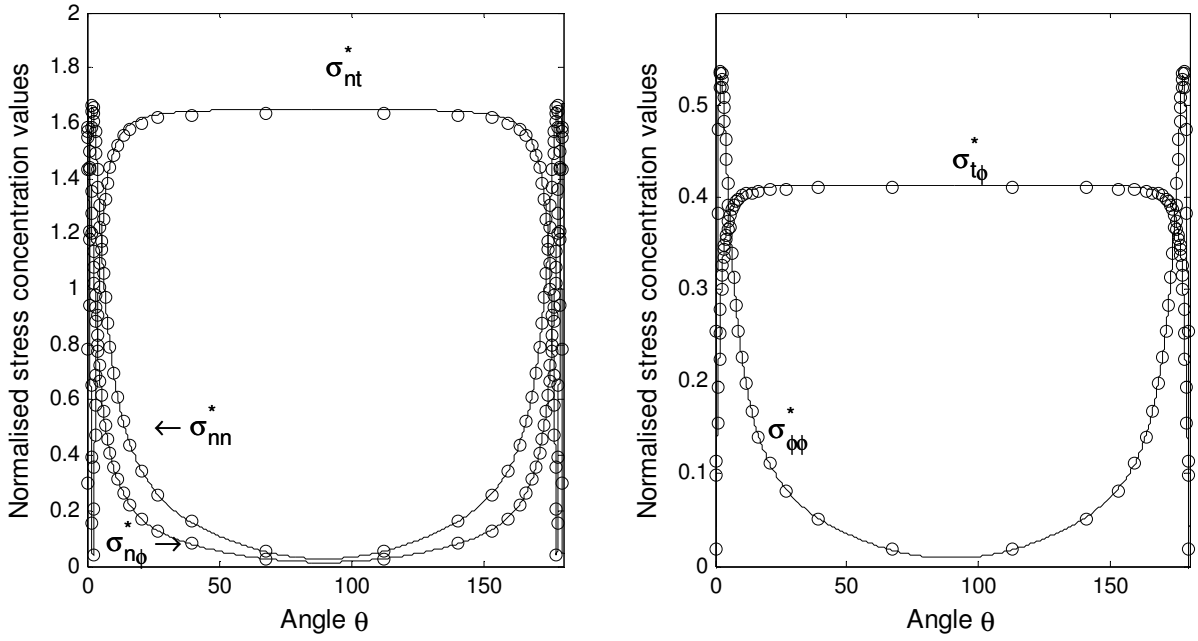

Figure 3.6 Comparison of stresses along the circumference of a spheroidal particle of *b/a*=5 subject to static loading

The maximum values of σ^*_{nn}, $\sigma^*_{n\phi}$ and σ^*_{nt} and are always greater than 1 in the considered range of normalized frequencies and so are of a great interest in this study, whereas the values of other three stresses σ_{tt}, $\sigma_{\phi\phi}$ and $\sigma_{t\phi}$ are always less than 1. Between the three stress components σ^*_{nn}, $\sigma^*_{n\phi}$ and σ^*_{nt} the dominant component seems to be $\sigma^*_{n\phi}$ and σ^*_{nt}. The maximum values of these stress components for both spherical and spheroidal geometries occur at θ =180˚. These are much larger than the stress concentration value corresponding to ω^* = 0.01, which is especially true for the spheroidal geometry.

Figure 3.10 shows the influence of the geometry on the dynamic stress concentration. To obtain this figure, the maximum value of $\sigma^*_{n\phi}$ at the particle-matrix interface for a given frequency was first calculated and the procedure was repeated for several discrete frequencies in the nondimensional frequency range 0–3. The maximum of $\sigma^*_{n\phi}$ for each frequency consistently occurred at θ =180˚. As expected, the dynamic stress concentration increases with the aspect ratio but this increase significantly depends on both the frequency and aspect ratio.

The effect of the mismatch of elastic constant μ^* between the particle and matrix on the dynamic stress concentration is presented in figure 3.11. It is evident that for any given frequency, the dynamic stress concentration increases with the degree of mismatch. This effect is especially predominant on the spheroidal particle.

Finally, the effect of the density of the particle on the stress concentration is illustrated in figure 3.12. It can be seen that the stress concentration is greater than that of the static case. This increase is higher for a particle having a higher density than that of the matrix. In particular, the dynamic stress concentration reaches a maximum value of 4.6 for the case ρ^* = 4 and this value is 147% more than the corresponding quasi-static value.

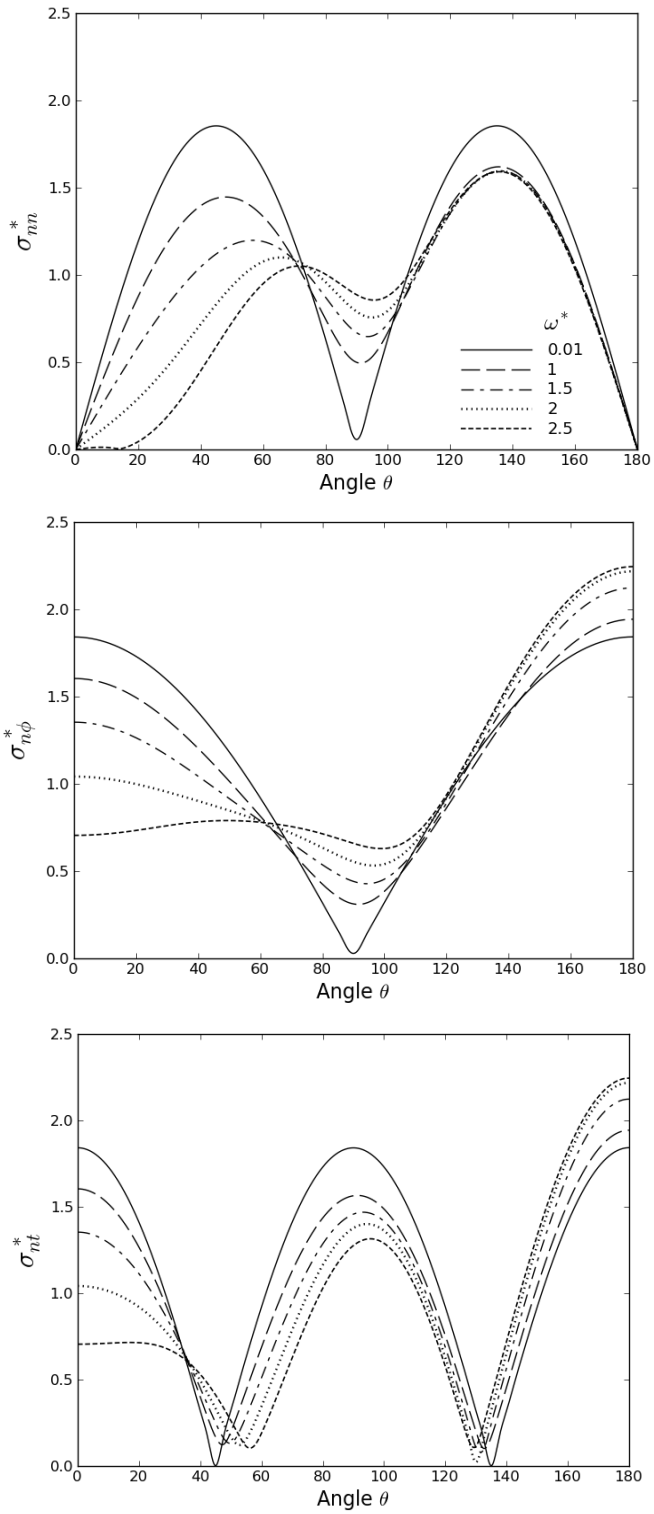

Figure 3.7 Angular distribution of stress concentration on the particle matrix interface for b/a=1 (ρ^*=1, μ^*=8, ν_1= ν_2=0.3)

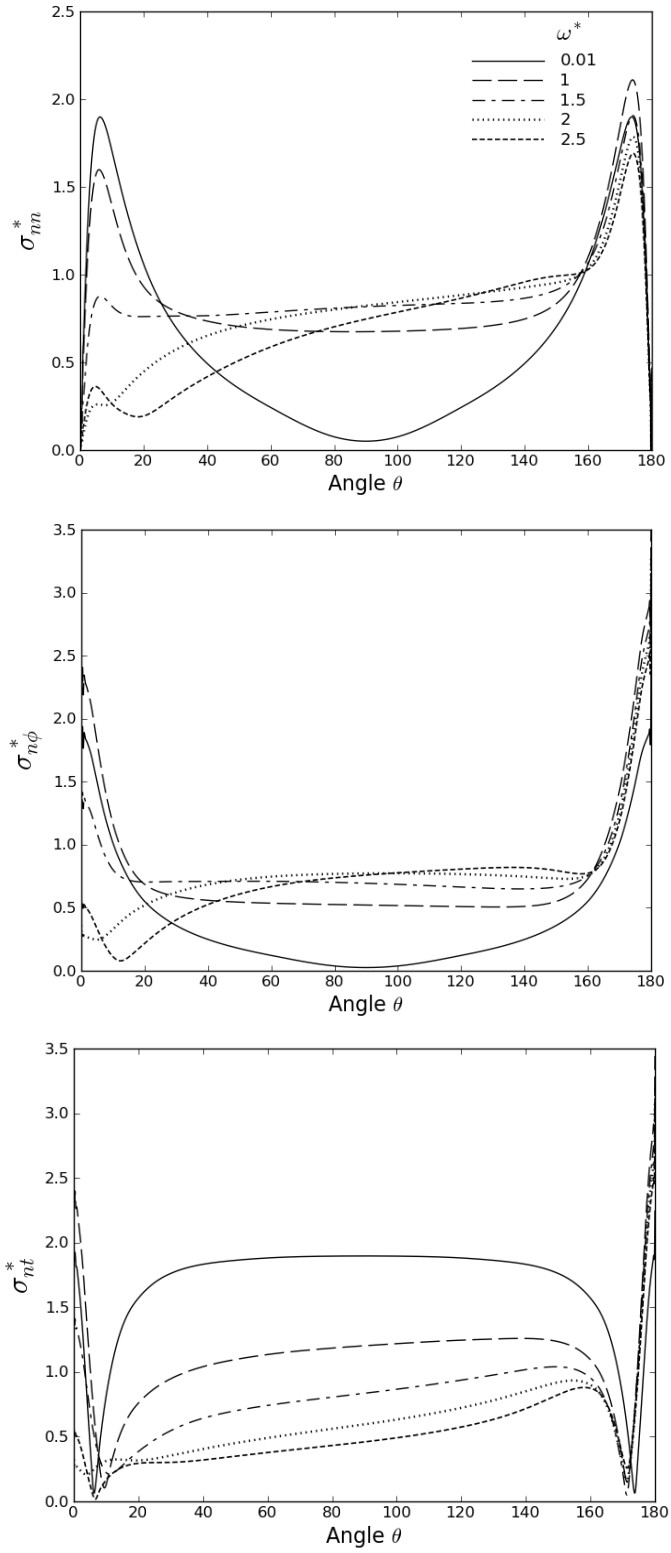

Figure 3.8 Angular distribution of stress concentration on the particle matrix interface for b/a=3 (ρ^*=1, μ^*=8, v_1= v_2=0.3)

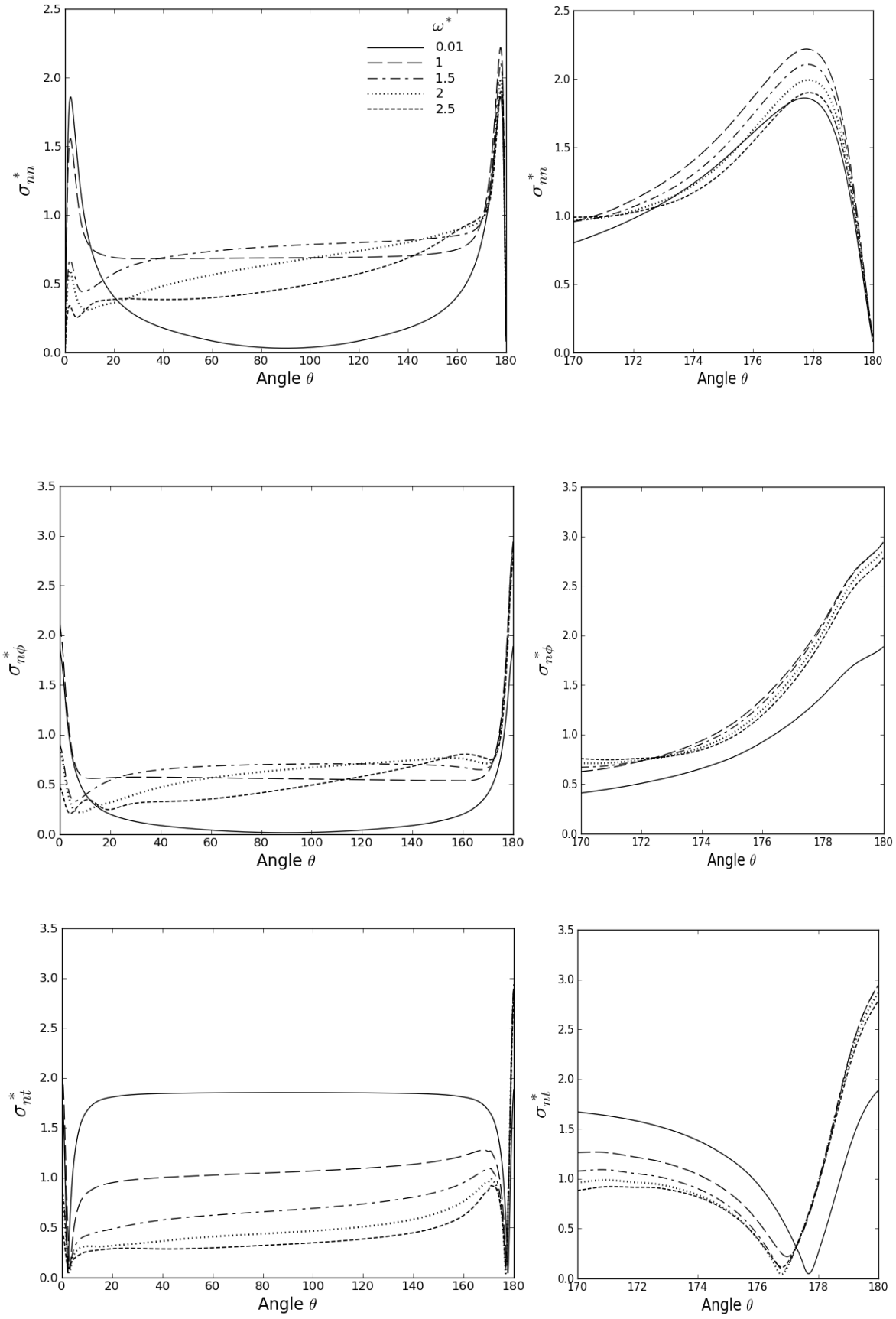

Figure 3.9 Angular distribution of stress concentration on the particle matrix interface for b/a =5 (ρ^*=1, μ^*=8, v_1= v_2=0.3)

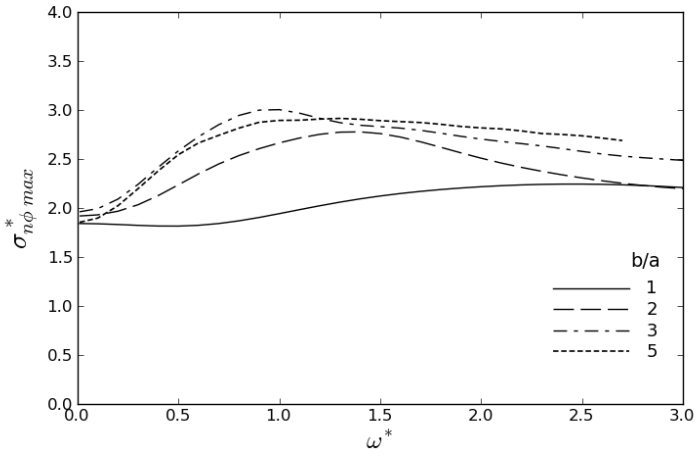

Figure 3.10 Effect of particle b/a value on peak stress concentration values on the particle matrix interface (ρ^*=1, μ^*=8, v_1= v_2=0.3)

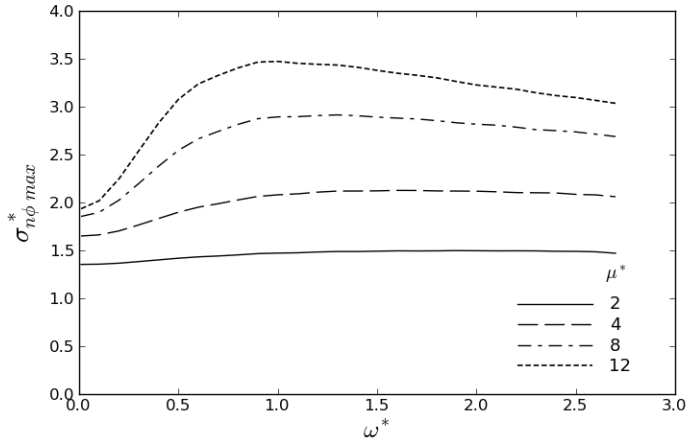

a)

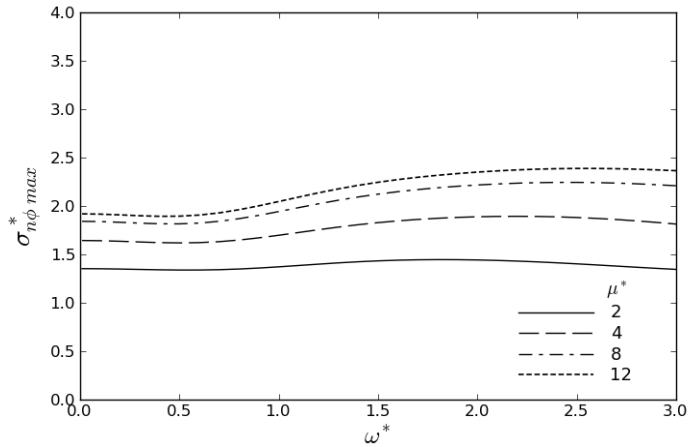

b)

Figure 3.11 Effect of particle stiffness on peak stress concentration values for: 3.17a) *b/a* =1 and 3.17b) *b/a* =5 (ρ^*=1, v_1= v_2=0.3)

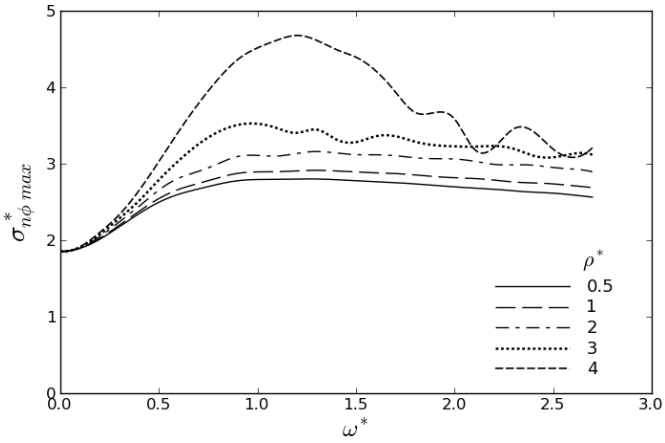

Figure 3.12 Effect of particle density on peak peak stress concentration values for *b/a* =5 (μ^*=8, ν_1=ν_2=0.3)

3.4. Conclusion

A hybrid axysimmetric finite element technique has been used to determine the stress concentration distribution around a spheroidal particle under asymmetric dynamic loading for various matrix and particle properties. The method combines the finite element technique with spherical wave functions to obtain the solution. The accuracy of the hybrid method has been verified by comparing the results with the analytical solution for a spherical particle. The study was done in the effort to predict the most likely location of crack initiation. The stress concentration values were presented at the particle-matrix interface being the region with the highest stress concentration values. These values at the spheroidal particle and matrix interface have shown to be significantly influenced by the variation of particle aspect ratio, excitation frequency and the degree of elastic mismatch between the particle and matrix. High values of particle stiffness have shown that the peak stress concentration values can be as high as 147% more than quasi-static values.

4. Effect of an interphase layer on the dynamic stress concentration in a Mg matrix surrounding a SiC particle

4.1. Formulation of the Problem

The three dimensional model studied here is shown in figure 4.1. The model consists of a normalized spherical particle radius $R_p=0.9$ embedded in an infinite matrix with the interphase layer applied between the particle and the matrix, which is represented by concentric spheres. This case hereafter is referred to as matrix – interphase – particle. Owing to the geometry the problem is best described by spherical coordinates (R, ϕ, θ).

The material properties are given by Lamé constants λ_i and μ_i and mass density by ρ_i. The subscripts i = 1, 2, 3 donate matrix (medium 1), particle (medium 2) and interphase layer (medium 3) respectively. The change in dynamic strength properties of the material as loading rate increases is ignored for simplicity. The dynamic excitation is provided by an incident plane compressional wave propagating in positive z-axis direction. Since the problem is symmetric about z-axis, field quantities such as displacements and stresses are independent of spherical ϕ coordinate. The contact between the particle, interphase layer and matrix is assumed to be welded, and materials elastic and linear.

Constant property materials and functionally graded materials were considered for the interphase. Constant property materials were modeled as a single layer with uniform material properties throughout the thickness. Functionally graded materials were modeled with multiple layers each having a uniform material property.

The time variation is assumed to be of the form $e^{i\omega t}$, where ω is the frequency of excitation. Thus, all field quantities have the same time variation which is suppresses in all subsequent representations for notational convenience.

Since the displacement component U_ϕ is zero due to symmetry, following Helmholtz's decomposition of a vector field, the general solution of equation (2.1) for this problem can be written as:

$$U = \nabla\chi + \frac{1}{\beta}\nabla\times\nabla(R\psi)\times e_R \tag{4.1}$$

By setting m=0 in equations (2.3) to (2.5) for plane compressional P-wave propagating in z-direction the potential functions χ and ψ may be written in spherical coordinates as:

$$\chi(R,\theta)=\sum_{n=0}^{\infty}a_{1n}Z_n(\alpha R)P_n(\cos\theta) \tag{4.2}$$

$$\psi(R,\theta)=\sum_{n=0}^{\infty}a_{2n}Z_n(\beta R)P_n(\cos\theta) \tag{4.3}$$

The potentials χ and ψ satisfy the equations (2.7) and (2.8).

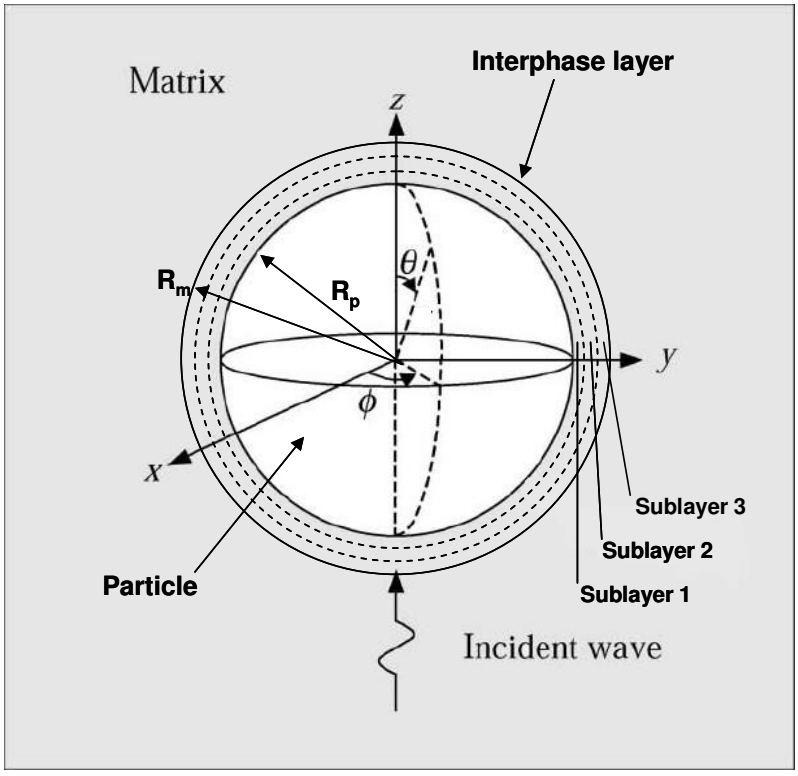

Figure 4.1 Schematic illustration of the matrix-interphase-particle problem.

The resulting displacement and stress amplitudes reduce to the following:

$$\bar{u}_R^n=\sum_{n=0}^{\infty}a_{1n}\left[\frac{n}{R}Z_n(\alpha R)-\alpha Z_{n+1}(\alpha R)\right]P_n^0+a_{2n}n(n+1)\frac{Z_n(\beta R)}{\beta R}P_n^0 \tag{4.4}$$

$$\bar{u}_\theta^n=\sum_{n=0}^{\infty}a_{1n}\frac{Z_n(\alpha R)}{R}\frac{dP_n^0}{d\theta}+a_{2n}\left[(n+1)\frac{Z_n(\beta R)}{\beta R}-Z_{n+1}(\beta R)\right]\frac{dP_n^0}{d\theta} \tag{4.5}$$

$$\bar{\sigma}_{RR}^{n} = a_{1nm}\frac{2\mu}{R^2}\left[\left(n^2-n-\frac{1}{2}\beta^2R^2\right)Z_n(\alpha R)+2\alpha R Z_{n+1}(\alpha R)\right]P_n^0 + a_{2nm}\frac{2\mu}{R^2}\frac{n(n+1)}{\beta}\left[(n-1)Z_n(\beta R)-\beta R Z_{n+1}(\beta R)\right]P_n^0 \tag{4.6}$$

$$\bar{\sigma}_{R\theta}^{n} = a_{1nm}\frac{2\mu}{R^2}\left[(n-1)Z_n(\alpha R)-\alpha R Z_{n+1}(\alpha R)\right]\frac{dP_n^0}{d\theta} + a_{2nm}\frac{2\mu}{R^2}\frac{1}{\beta}\left[\left(n^2-n-\frac{1}{2}\beta^2R^2\right)Z_n(\beta R)+\beta R Z_{n+1}(\beta R)\right]\frac{dP_n^0}{d\theta} \tag{4.7}$$

$$\bar{\sigma}_{\theta\theta}^{n} = a_{1nm}\frac{2\mu}{R^2}\left[\left\{\left(n+\alpha^2R^2-\frac{1}{2}\beta^2R^2\right)Z_n(\alpha R)-\alpha R Z_{n+1}(\alpha R)\right\}P_n^0+Z_n(\alpha R)\frac{d^2P_n^0}{d\theta^2}\right] + a_{2nm}\frac{2\mu}{R^2}\frac{1}{\beta}\left[n(n+1)Z_n(\beta R)P_n^0+\left\{(n+1)Z_n(\beta R)-\beta R Z_{n+1}(\beta R)\right\}\frac{d^2P_n^0}{d\theta^2}\right] \tag{4.8}$$

In the above, the argument ($\cos\theta$) for P_n^0 and its derivatives has been suppressed for notational convenience.

Refer to the chapter 2.1 for further explanation of the terms in above equations.

4.1.1. Refracted wave field in the particle

The refracted waves, being confined in the spherical particle, are standing waves. Using the solutions of the wave equations (4.2) and (4.3), they can be represented by

$$\chi^{rfr} = \sum_{n=0}^{\infty} b_{1n}\, j_n(\alpha_2 R)\; P_n^0(cos\theta) \tag{4.9}$$

$$\psi^{rfr} = \sum_{n=0}^{\infty} b_{2n}\, j_n(\beta_2 R)\; P_n^0(cos\theta) \tag{4.10}$$

where j_n is the spherical Bessel function of the first kind and $P_n^0(\cos\theta)$ is the Legendre polynomial. Superscript *rfr* refers to refracted wave field and subscript 2 refers to the particle medium.

By substituting equations (4.9) and (4.10) into equation (4.1) and the resulting expressions into equations (2.30) to (2.33) the displacements and stresses in spherical coordinate system due to refracted field in the particle are obtained.

$$\bar{u}_R^{rfr} = \sum_{n=0}^{\infty} b_{1n}\left[\frac{n}{R}\,j_n(\alpha_2 R)-\alpha_2\, j_{n+1}(\alpha_2 R)\right]P_n^0 + b_{2n}n(n+1)\frac{j_n(\beta_2 R)}{\beta_2 R}P_n^0 \tag{4.11}$$

$$\bar{u}_{\theta}^{rfr} = \sum_{n=0}^{\infty} b_{1n} \frac{j_n(\alpha_2 R)}{R} \frac{dP_n^0}{d\theta} + b_{2n} \left[(n+1) \frac{j_n(\beta_2 R)}{\beta_2 R} - j_{n+1}(\beta_2 R) \right] \frac{dP_n^0}{d\theta} \tag{4.12}$$

$$\begin{aligned} \bar{\sigma}_{RR}^{rfr} = & \sum_{n=0}^{\infty} b_{1n} \frac{2\mu_2}{R^2} \left[\left(n^2 - n - \frac{1}{2} \beta_2^2 R^2 \right) j_n(\alpha_2 R) + 2\alpha_2 R j_{n+1}(\alpha_2 R) \right] P_n^0 \\ & + b_{2n} \frac{2\mu_2}{R^2} \frac{n(n+1)}{\beta_2} \left[(n-1) j_n(\beta_2 R) - \beta_2 R j_{n+1}(\beta_2 R) \right] P_n^0 \end{aligned} \tag{4.13}$$

$$\begin{aligned} \bar{\sigma}_{R\theta}^{rfr} = & \sum_{n=0}^{\infty} b_{1n} \frac{2\mu_2}{R^2} \left[(n-1) j_n(\alpha_2 R) - \alpha_2 R j_{n+1}(\alpha_2 R) \right] \frac{dP_n^0}{d\theta} \\ & + b_{2n} \frac{2\mu_2}{R^2} \frac{1}{\beta_2} \left[\left(n^2 - n - \frac{1}{2} \beta_2^2 R^2 \right) j_n(\beta_2 R) + \beta_2 R j_{n+1}(\beta R) \right] \frac{dP_n^0}{d\theta} \end{aligned} \tag{4.14}$$

4.1.2. Refracted wave field in the interphase layer

The wave field in the interphase layer, as well as for each sublayer, also consists of standing refracted waves. For any i^{th} layer, the solution can be written in the form:

$$\chi^{rfr} = \sum_{n=0}^{\infty} c_{1n} j_n(\alpha_3 R)\ P_n^0(cos\theta) + c_{2n} y_n(\alpha_3 R)\ P_n^0(cos\theta) \tag{4.15}$$

$$\psi^{rfr} = \sum_{n=0}^{\infty} c_{3n} j_n(\beta_3 R)\ P_n^0(cos\theta) + c_{4n} y_n(\beta_3 R)\ P_n^0(cos\theta) \tag{4.16}$$

where y_n is the spherical Bessel function of the second kind and the subscript 3 refers to the interphase layer medium.

By substituting equations (4.15) and (4.16) into equation (4.1) and the resulting expressions into equations (2.30) to (2.33) the displacement and stresses in spherical coordinate system due to refracted field in the interphase layer, and each sublayer are obtained.

$$\begin{aligned} \bar{u}_R^{rfr} = & \sum_{n=0}^{\infty} c_{1n} \left[\frac{n}{R} j_n(\alpha_3 R) - \alpha_3 j_{n+1}(\alpha_3 R) \right] P_n\ + c_{2n} n(n+1) \frac{j_n(\beta_3 R)}{\beta_3 R} P_n^0 \\ & + c_{3n} \left[\frac{n}{R} y_n(\alpha_3 R) - \alpha_3 y_{n+1}(\alpha_3 R) \right] P_n\ + c_{4n} n(n+1) \frac{y_n(\beta_3 R)}{\beta_3 R} P_n^0 \end{aligned} \tag{4.17}$$

$$\begin{aligned} \bar{u}_{\theta}^{rfr} = & \sum_{n=0}^{\infty} c_{1n} \frac{j_n(\alpha_3 R)}{R} \frac{dP_n^0}{d\theta} + c_{2n} \left[(n+1) \frac{j_n(\beta_3 R)}{\beta_3 R} - j_{n+1}(\beta_3 R) \right] \frac{dP_n^0}{d\theta} \\ & + c_{3n} \frac{y_n(\alpha_3 R)}{R} \frac{dP_n^0}{d\theta} + c_{4n} \left[(n+1) \frac{y_n(\beta_3 R)}{\beta_3 R} - y_{n+1}(\beta_3 R) \right] \frac{dP_n^0}{d\theta} \end{aligned} \tag{4.18}$$

$$\begin{aligned}\bar{\sigma}_{RR}^{rfr} = &\sum_{n=0}^{\infty} c_{1n}\frac{2\mu_3}{R^2}\left[\left(n^2-n-\frac{1}{2}\beta_3^2R^2\right)j_n(\alpha_3R)+2\alpha_3Rj_{n+1}(\alpha_3R)\right]P_n^0\\ &+c_{2n}\frac{2\mu_3}{R^2}\frac{n(n+1)}{\beta_3}\left[(n-1)\,j_n(\beta_3R)-\beta_3Rj_{n+1}(\beta_3R)\right]P_n^0\\ &+c_{3n}\frac{2\mu_3}{R^2}\left[\left(n^2-n-\frac{1}{2}\beta_3^2R^2\right)y_n(\alpha_3R)+2\alpha_3Ry_{n+1}(\alpha_3R)\right]P_n^0\\ &+c_{4n}\frac{2\mu_3}{R^2}\frac{n(n+1)}{\beta_3}\left[(n-1)\,y_n(\beta_3R)-\beta_3Ry_{n+1}(\beta_3R)\right]P_n^0\end{aligned} \tag{4.19}$$

$$\begin{aligned}\bar{\sigma}_{R\theta}^{rfr} = &\sum_{n=0}^{\infty} c_{1n}\frac{2\mu_3}{R^2}\left[(n-1)\,j_n(\alpha_3R)-\alpha_3Rj_{n+1}(\alpha_3R)\right]\frac{dP_n^0}{d\theta}\\ &+c_{2n}\frac{2\mu_3}{R^2}\frac{1}{\beta_3}\left[\left(n^2-n-\frac{1}{2}\beta_3^2R^2\right)j_n(\beta_3R)+\beta_3Rj_{n+1}(\beta_3R)\right]\frac{dP_n^0}{d\theta}\\ &+c_{3n}\frac{2\mu_3}{R^2}\left[(n-1)\,y_n(\alpha_3R)-\alpha_3Ry_{n+1}(\alpha_3R)\right]\frac{dP_n^0}{d\theta}\\ &+c_{4n}\frac{2\mu_3}{R^2}\frac{1}{\beta_3}\left[\left(n^2-n-\frac{1}{2}\beta_3^2R^2\right)y_n(\beta_3R)+\beta_3Ry_{n+1}(\beta_3R)\right]\frac{dP_n^0}{d\theta}\end{aligned} \tag{4.20}$$

4.1.3. Incident and scattered wave fields in the matrix

The incident plane compressional *P*-wave travelling in positive *z*-direction through the matrix can be represented by two potentials:

$$\chi^{inc} = e^{i\alpha_1 z - i\varpi t};\quad \psi^{inc} = 0 \tag{4.21}$$

where subscript *inc* indicates the incident field.

When potential χ^{inc} is expanded in terms of spherical eigenfunctions as:

$$\chi^{inc} = \sum_{n=0}^{\infty} i^n(2n+1)\,j_n(\alpha_1R)\;P_n^0(cos\theta) \tag{4.22}$$

Here subscript 1 refers to the matrix medium.

By substituting equations (4.22) into equation (4.1) and the resulting expressions into equations (2.30) to (2.33) the displacement and stresses in the matrix due to incident field are obtained.

$$\bar{u}_R^{inc} = \sum_{n=0}^{\infty} i^n(2n+1)\left[\frac{n}{R}j_n(\alpha_1R)-\alpha_1j_{n+1}(\alpha_1R)\right]P_n^0 \tag{4.23}$$

$$\bar{u}_\theta^{inc} = \sum_{n=0}^{\infty} i^n(2n+1)\frac{j_n(\alpha_1R)}{R}\frac{dP_n^0}{d\theta} \tag{4.24}$$

$$\bar{\sigma}_{RR}^{inc} = \sum_{n=0}^{\infty} i^n (2n+1) \frac{2\mu_1}{R^2} \left[\left(n^2 - n - \frac{1}{2}\beta_1^2 R^2 \right) j_n(\alpha_1 R) + 2\alpha_1 R j_{n+1}(\alpha_1 R) \right] P_n^0 \tag{4.25}$$

$$\bar{\sigma}_{R\theta}^{inc} = \sum_{n=0}^{\infty} i^n (2n+1) \frac{2\mu_1}{R^2} \left[(n-1)\, j_n(\alpha_1 R) - \alpha_1 R j_{n+1}(\alpha_1 R) \right] \frac{dP_n^0}{d\theta} \tag{4.26}$$

Scattered wave field expressions, just as refracted fields, can be obtained from solutions of the wave equations (4.2) and (4.3). For the scattered field in the matrix only the waves propagating outward need to be considered and they are given by

$$\chi^{sct}(R,\theta) = \sum_{n=0}^{\infty} a_{1n} h_n(\alpha_1 R) P_n^0(\cos\theta) \tag{4.27}$$

$$\psi^{sct}(R,\theta) = \sum_{n=0}^{\infty} a_{2n} h_n(\beta_1 R) P_n^0(\cos\theta) \tag{4.28}$$

where h_n is the Henkel function of the first kind and superscript *sct* refers to scattered wave field.

Again by substituting equations (4.27) and (4.28) into equation (4.1) and the resulting expressions into equations (2.30) to (2.33) the displacement and stresses in the matrix due to scattered field are obtained.

$$\bar{u}_R^{sct} = \sum_{n=0}^{\infty} a_{1n} \left[\frac{n}{R} h_n(\alpha_1 R) - \alpha_1 h_{n+1}(\alpha_1 R) \right] P_n^0 + a_{2n} n(n+1) \frac{h_n(\beta_1 R)}{\beta_1 R} P_n^0 \tag{4.29}$$

$$\bar{u}_\theta^{sct} = \sum_{n=0}^{\infty} a_{1n} \frac{h_n(\alpha_1 R)}{R} \frac{dP_n^0}{d\theta} + a_{2n} \left[(n+1) \frac{h_n(\beta_1 R)}{\beta_1 R} - h_{n+1}(\beta_1 R) \right] \frac{dP_n^0}{d\theta} \tag{4.30}$$

$$\begin{aligned} \bar{\sigma}_{RR}^{sct} = & \sum_{n=0}^{\infty} a_{1n} \frac{2\mu_1}{R^2} \left[\left(n^2 - n - \frac{1}{2}\beta_1^2 R^2 \right) h_n(\alpha_1 R) + 2\alpha_1 R h_{n+1}(\alpha_1 R) \right] P_n^0 \\ & + a_{2n} \frac{2\mu_1}{R^2} \frac{n(n+1)}{\beta_1} \left[(n-1) h_n(\alpha_1 R) - \beta_1 R h_{n+1}(\beta_1 R) \right] P_n^0 \end{aligned} \tag{4.31}$$

$$\begin{aligned} \bar{\sigma}_{R\theta}^{sct} = & \sum_{n=0}^{\infty} a_{1n} \frac{2\mu_1}{R^2} \left[(n-1) h_n(\alpha_1 R) - \alpha_1 R h_{n+1}(\alpha_1 R) \right] \frac{dP_n^0}{d\theta} \\ & + a_{2n} \frac{2\mu_1}{R^2} \frac{1}{\beta_1} \left[\left(n^2 - n - \frac{1}{2}\beta_1^2 R^2 \right) h_n(\beta_1 R) + \beta_1 R h_{n+1}(\beta_1 R) \right] \frac{dP_n^0}{d\theta} \end{aligned} \tag{4.32}$$

The coefficients a_n, b_n, and c_n in equations (4.29) to (4.32), (4.11) to (4.14) and (4.17) to (4.20) are to be determined from the boundary conditions between particle, interphase layer and matrix.

4.1.4. Boundary conditions

At the interface between matrix and the interphase layer the displacements and stresses must be continuous. The total field in the matrix is obtained by superposition of incident and scattered field. Thus the boundary conditions are:

$$ {}^{1}\overline{u}_R^{inc} + {}^{1}\overline{u}_R^{sct} = {}^{3}\overline{u}_R^{rfr} \tag{4.33} $$

$$ {}^{1}\overline{u}_\theta^{inc} + {}^{1}\overline{u}_\theta^{sct} = {}^{3}\overline{u}_\theta^{rfr} \tag{4.34} $$

$$ {}^{1}\overline{\sigma}_{R\theta}^{inc} + {}^{1}\overline{\sigma}_{R\theta}^{sct} = {}^{3}\overline{\sigma}_{R\theta}^{rfr} \tag{4.35} $$

$$ {}^{1}\overline{\sigma}_{RR}^{inc} + {}^{1}\overline{\sigma}_{RR}^{sct} = {}^{3}\overline{\sigma}_{RR}^{rfr} \tag{4.36} $$

where superscripts on the left of the terms refer to the medium and on the right of the term refers to the wave type.

The boundary conditions at the interface of the interphase layer and the particle are:

$$ {}^{3}\overline{u}_R^{rfr} = {}^{2}\overline{u}_R^{rfr} \tag{4.37} $$

$$ {}^{3}\overline{u}_\theta^{rfr} = {}^{2}\overline{u}_\theta^{rfr} \tag{4.38} $$

$$ {}^{3}\overline{\sigma}_{RR}^{rfr} = {}^{2}\overline{\sigma}_{RR}^{rfr} \tag{4.39} $$

$$ {}^{3}\overline{\sigma}_{R\theta}^{rfr} = {}^{2}\overline{\sigma}_{R\theta}^{rfr} \tag{4.40} $$

By invoking the orthogonality relations of Legendre polynomials, one obtains, for each $n \geq 0$, a set of simultaneous algebraic equations. When there are three layers, for example, a set of twenty equations are obtained which can be expressed in matrix form as:

$$ [E]\{a_n\} = \{f\} \tag{4.41} $$

where the vector $\{a_n\}$ contains the unknown coefficients a_n , b_n and c_n, and elements of $[E]$ and $\{f\}$ are complex valued. Equation (4.41) is solved to obtain these coefficients. The elements of the matrix $[E]$ and the vector $\{f\}$ in case of one interphase layer are shown in Appendix B.

4.2. Numerical results and discussion

In this study, the dynamic excitation is provided by an incident *P*-wave defined by equation (4.21). In the absence of the reinforcing particle, the stress field at any point in the medium can be expressed in rectangular coordinates as

$$\sigma_{xx} = -\lambda_1 \alpha_1^2 e^{i(\alpha_1 z - \omega t)} \tag{4.42}$$

$$\sigma_{yy} = -\lambda_1 \alpha_1^2 e^{i(\alpha_1 z - \omega t)} \tag{4.43}$$

$$\sigma_{zz} = -\mu_1 \beta_1^2 e^{i(\alpha_1 z - \omega t)} \tag{4.44}$$

$$\sigma_{xy} = \sigma_{yz} = \sigma_{zx} = 0 \tag{4.45}$$

Since all the shear stresses vanish, all the normal stresses are principal stresses and the maximum value is $\sigma_0 = -\mu_1 \beta_1^2 e^{i(\alpha_1 z - \omega t)}$. When a particle is present, the stress field is significantly different from that given by equations (4.42) to (4.45) due to multiple reflection and scattering. The addition of an interphase layer further changes this stress field.

The variation of stress components σ_{RR} , $\sigma_{\theta\theta}$ and $\sigma_{\phi\phi}$ as well as von Mises equivalent stress, σ_{vm}, are presented to show the influence that the configuration of the interphase layer has on the dynamic stress concentration in the matrix. The von Mises stress is often used to describe the failure criterion of ductile material such as Mg. The von Mises equivalent stress incorporates terms from the full stress tensor and can be calculated in terms of the principal stresses σ_1, σ_2 and σ_3 :

$$\sigma_{vm} = \frac{1}{\sqrt{2}}\left[(\sigma_1 - \sigma_2)^2 + (\sigma_2 - \sigma_3)^2 + (\sigma_3 - \sigma_1)^2\right]^{\frac{1}{2}} \tag{4.46}$$

The normal stresses and the von Mises stress are expressed in dimensionless forms by normalizing with respect to σ_0 and σ_0' respectively:

$$\sigma_{ij}^* = \frac{|\sigma_{ij}|}{\sigma_0} \qquad i, j = R, \theta, \phi \tag{4.47}$$

$$\sigma_{vm}^* = \frac{|\sigma_{vm}|}{\sigma_0'} \tag{4.48}$$

where

$$\sigma_0' = \frac{1 - 2\nu_1}{1 - \nu_1} \mu_1 \beta_1^2 \tag{4.49}$$

The expression for σ_0' was obtained by substituting equations (4.42) to (4.45) into equation (4.46). Thus, σ_0' represents the maximum value of the von Mises stress in the matrix if no

particle was present. Since σ_0 also represents the maximum value of the principal stress in the matrix in the absence of a particle, the values of σ_{ij}^* and σ_{vm}^* given by equations (4.47) and (4.48) can be considered as dynamic stress concentration factors which depend on a number of non-dimensional variables including:

1. the frequency of excitation,
2. the ratio of shear moduli of interphase layer and matrix, μ_3/μ_1,
3. the Poisson's ratio v_3, and
4. the ratio of densities, ρ_3/ρ_1.

In order to present the results in a non-dimensional form, all the linear dimensions have been normalised with respect to the matrix radius R_m. The frequency of excitation is expressed in non-dimensional form through

$$\omega^* = \omega a_m \sqrt{\frac{\rho_1}{(\lambda_1 + 2\mu_1)}} \tag{4.50}$$

For computations, a frequency range of $\omega^* = 0$ to 3 is considered. The SiC-particle and Mg-matrix offer the following material properties:

$\mu_2/\mu_1 = 11.4$
$\rho_2/\rho_1 = 1.77$
$v_2 = v_1 = 0.3$

In addition, the following values of the material parameters are chosen for the interphase layer:

$\rho_3/\rho_1 = 0.5, 07, 1, 1.4, 1.77, 2, 2.2$
$\mu_3/\mu_1 = 25, 15, 8, 4, 0.8, 0.6, 0.4$
$v_3 = 0.4, 0.3, 0.2, 0.1, 0.05$

These values are sufficient to cover the range of parameters which might be encountered in practical applications and demonstrate the essential behavior of dynamic stress concentrations.

The thickness of the interphase layer zone is assumed to be equal to $0.1R_m$. In order to quantify the effect of the interphase layer on the stress concentration in the matrix, stresses were computed in the matrix with and without the interphase. In both cases, the stresses were computed in the matrix at the same locations. This was achieved by using a particle size of $0.9R_m$ when an interphase layer was present.

An appreciation of the dynamic loading can be gained by considering the limiting static case. When the frequency approaches zero, the applied stress field at infinity tends towards

$$\sigma_{zz} = -\sigma_o \tag{4.51}$$

$$\sigma_{xx} = \sigma_{yy} = -\frac{\nu_1}{1-\nu_1}\sigma_0 \tag{4.52}$$

$$\sigma_{xy} = \sigma_{yz} = \sigma_{zx} = 0 \tag{4.53}$$

The stress field of equations (4.51) to (4.53) is triaxial. Thus, the results presented herein are for the dynamic counterpart of this triaxial load.

The stress field in the matrix in the absence of an interphase is initially calculated for various frequencies by adding the incident and scattered field amplitudes. The stresses are expressed as infinite series in equations (4.25), (4.26), (4.31) and (4.32). The series, however, converged rapidly, requiring a maximum of 25 terms for the largest frequency. Since Bessel functions, such as $j_{n,}$ grow to very large values with $n,$ they often present difficulties in numerical calculations. However, no such difficulties were encountered during the computation due to the use of normalised values for size and material parameters. The results are shown in figure 4.2 for two frequencies, ω^* = 0.02 and 2.0, where three stress components are plotted for a portion of the matrix surrounding the particle. The plane wave is approaching from the bottom of the figure in all cases, and the colour bar at the base of the figure indicates the range of stress concentration factors that occur. The particle is shown in each case by a circle of unit radius. The frequency of ω^* = 0.02 can be considered as representing a *quasi-static* state, since the wave length at this frequency is several times larger than the particle. Thus, hardly any dynamic effects are expected and the corresponding results may be considered as the quasi-static solution. A separate static analysis, based on the works of Eshelby [60, 61], revealed that the results corresponding to ω^* = 0.02 coincided with the static solutions. It can be seen in figure 4.2 that stress components display symmetry about θ = 90º which is consistent with the loading given by equations (4.51) to (4.53).

The presence of dynamic loading effects is evident in the results corresponding to the normalised frequency of ω^* = 2. In this case, considerable reflection, refraction and scattering of the incident wave takes place, resulting in a significantly different stress field. The increase in frequency has led to a concentration of high values of σ^*_{RR} on the illuminated side of the particle near the particle/matrix interface. The maximum value of σ^*_{RR} in the matrix occurs at the interface between the particle and matrix, on the θ = 180º line and is greater than the corresponding maximum value for the quasi-static case. A rippling effect can also be seen to have developed behind this point of maximum stress, indicating the effect of dynamic loading. The maximum of $\sigma^*_{\phi\phi}$ also occurs at this point but its value is significantly lower than that of σ^*_{RR}. For the stress component $\sigma^*_{\theta\theta}$, the maximum value also occurs at the particle-matrix interface, but at the angular location of θ = 90º. The concentration of high values for the different stress components at the particle-matrix interface seems to substantiate a common observation that in many practical applications of particulate-reinforced composites, failure often initiates in the matrix at the interface between the particle and matrix. Even though the results are not shown here, it was noted that the stress field in the particle was comparable to that in the matrix. Particles, however, often have considerably

larger modulus and substantially higher yield stress values than the matrix and initiation of failure will therefore most likely take place within the matrix. For this reason the attention henceforth is limited to the state of stress in the matrix only. In the following sections, interphase regions with unknown yield strength will be introduced and the possibility of failure in these regions will also be ignored.

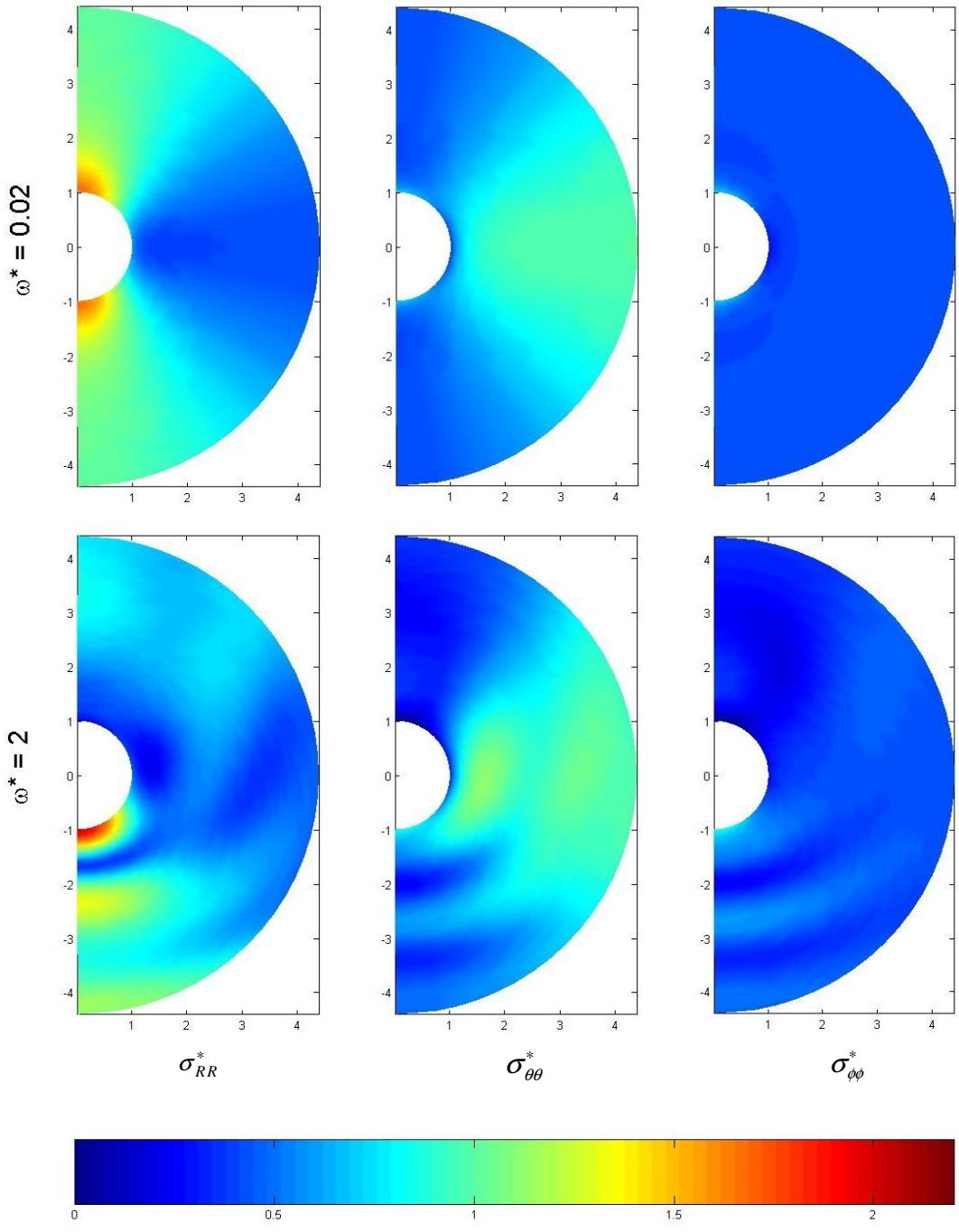

Figure 4.2 Stress distribution around the particle without the interphase layer for two frequencies ($\mu_2/\mu_1 = 11.4$; $\nu_2 = \nu_1 = 0.3$)

4.2.1. Effect of an interphase layer of higher elastic modulus than the matrix

The effect on the stress concentration within the matrix resulting from the addition of an interphase layer was considered for the following configurations: μ_3/μ_1 = 4, 8, 15 and 25. For a given frequency, the stress concentration in the matrix was obtained by first calculating the stress components at the radius $R = R_m$ for various angles and then taking the maximum value. This procedure was repeated for a number of normalised frequencies in the range 0 to 3. These results are presented in figure 4.3 which shows the variation of stress concentration in the matrix with frequency. It is seen that the addition of an interphase layer leads to slightly lower stress concentrations at low frequencies. However, slightly higher stress concentrations are often seen at high frequencies.

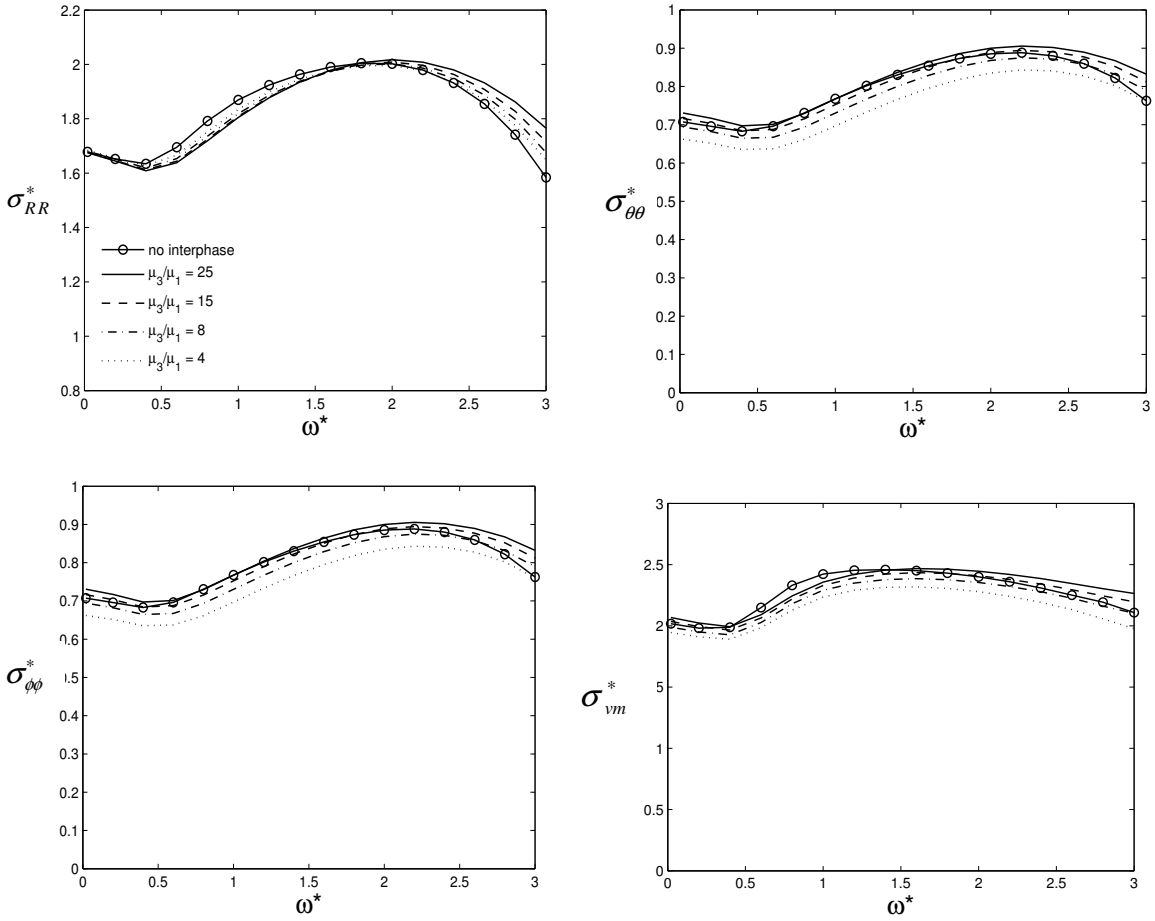

Figure 4.3 Effect of interphase layer with an elastic modulus larger than that of the matrix

The stress concentration values for $\sigma^*_{\phi\phi}$ and $\sigma^*_{\theta\theta}$ are less than 1, that is, there is no stress amplification. For the stress components σ^*_{RR} and σ^*_{vm}, the dynamic stress concentration values are lower than the quasi-static ones for normalised frequencies up to 0.6. At normalised frequencies greater than 0.6, each curve displays a local maximum. The stress concentration factors at local maximum points are greater than the corresponding quasi-static values and they occur at various frequencies. Even though some reduction in stress concentration is possible at a particular frequency, it is not always possible to achieve a consistent reduction of stress concentration over the given frequency range 0 to 3.

4.2.2. Effect of a functionally graded interphase layer

The previous results clearly indicate that no significant reduction in the maximum value of any normal stress component is possible through the introduction of an interphase layer with an elastic modulus larger than the matrix. In recent years, functionally graded materials have been receiving a lot of attention for applications in extremely high temperature environments and in bonded media (Koizumi [62] and Lee *et al* [63]). The advantage of functionally graded material stems from the ability to tailor a continuous and gradual variation of its thermal and mechanical properties. The potential for reducing stress concentration through using a functionally graded material in the interphase layer will now be investigated. The shear modulus of the interphase layer is assumed to have a linear variation with a value equal to that of the matrix at the matrix interface, and to that of the particle at the particle interface as shown in figure 4.4. Such an interphase layer eliminates material discontinuities at the interfaces. It was anticipated that this would eliminate or substantially reduce the stress concentrations. For modeling purposes, the interphase layer is divided into one, two or three sublayers, each sublayer having a uniform property.

In the case of three sublayers, each sublayer has a thickness of 0.0333 R_m so that the thickness of the interphase layer remains at $0.1R_m$. Since each sublayer has uniform material properties, the expressions for displacements and stresses in each sublayer are given by equations (4.17) to (4.20). Figure 4.5 depicts the effect of the functionally graded interphase layer on the stress concentration for σ^*_{RR} and σ^*_{vm}. The results for $\sigma^*_{\phi\phi}$ and $\sigma^*_{\theta\theta}$ are not presented since their values are, in all cases, significantly less than those of σ^*_{RR} and σ^*_{vm}. In spite of the initial anticipation, the reduction in stress concentration is not significant and, at high frequencies, the stress concentration for σ^*_{RR} is slightly increased. A closer examination reveals that the results for σ^*_{RR} are similar to those displayed in figure 4.3 In fact, this is to be expected since the effective modulus of the interphase layer in all sublayer configurations is greater than that of the matrix. The von Mises stress, unlike σ^*_{RR}, shows a consistent decrease throughout the frequency range. This reduction varies depending on a frequency with maximum reduction being 6% at $\omega^* = 1$. It is somewhat surprising to note that the number of sublayers has little effect on the stress concentration factors.

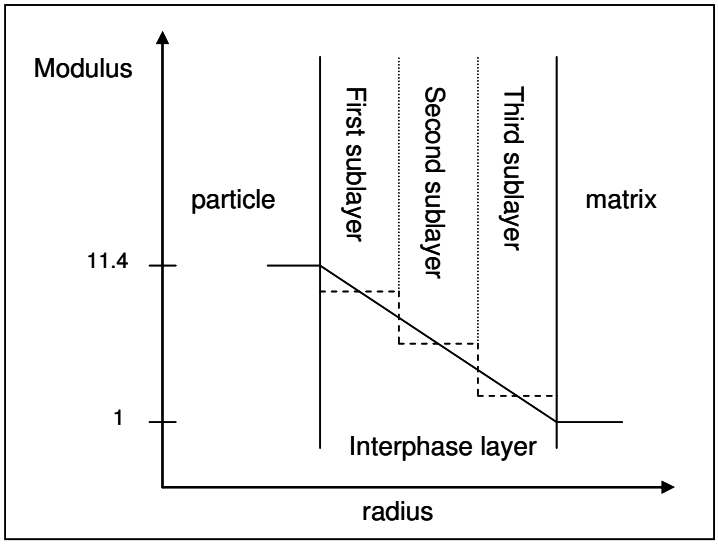

Figure 4.4 Schematic variation of the elastic modulus of a functionally graded material

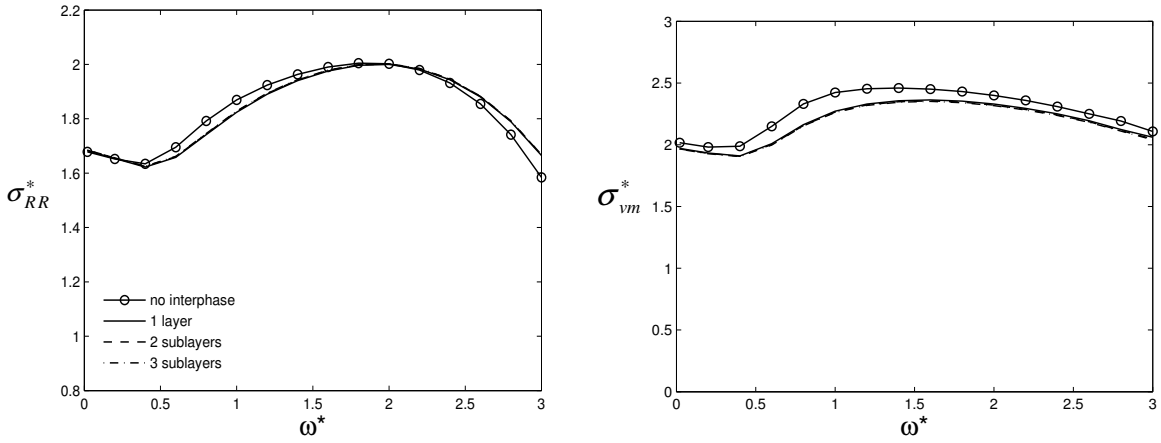

Figure 4.5 Effect of a functionally graded interphase layer

4.2.3. Effect of an interphase layer with an elastic modulus lower than the matrix

In particulate-reinforced composites subjected to static loads, it has been demonstrated by Carman *et al* [30], for example, that an interphase layer with a lower elastic modulus than the matrix reduces the matrix stresses. In this section, this is further investigated for a dynamic loading by considering a constant-property interphase layer. Figure 4.6 presents the variation of σ^*_{RR} and σ^*_{vm} for decreasing values of interphase layer modulus: μ_3/μ_1 = 1, 0.8, 0.6, and 0.4. The results clearly indicate that a reduction in the local maximum of σ^*_{RR} is possible with the introduction of a low-modulus interphase. The reduction becomes more significant at high frequencies. For instance, when μ_3/μ_1 = 0.4 and ω^* = 3, the stress concentration for σ^*_{RR} is reduced from 1.60 to 1.26 which represents a reduction of 21 % while von Mises stress shows a substantial reduction of 37 %. However in the frequency range from 0.8 to 1.25, this interphase layer is seen to cause a slight increase for both stress concentration factors.

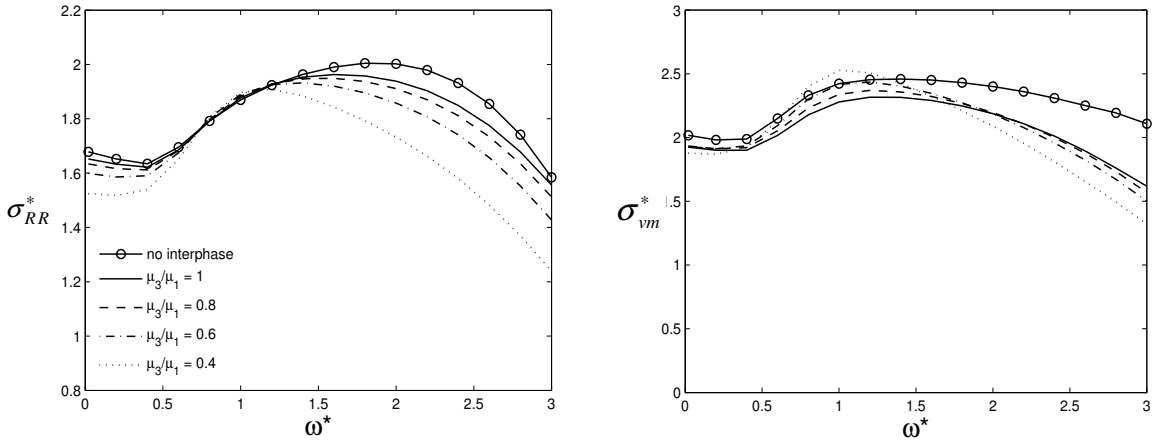

Figure 4.6 Effect of interphase layer with a stiffness lower than that of the matrix

4.2.4. Effect of Poisson's ratio

The values of the Poisson's ratio of the interphase layer have thus far been kept constant. It will be investigated now how this variable affects the stress concentration in the matrix. Figure 4.7 represents the effect that the Poisson's ratio of the interphase layer has on the stress concentration for σ^*_{RR} and σ^*_{vm} when μ_3/μ_1 = 0.4. It can be seen that there is a consistent reduction of stress concentration for σ^*_{RR} when the Poisson's ratio of the interphase layer is decreased and this reduction is significant at high frequencies. In fact, a reduction of 41% can be seen when the normalised frequency is 3. A similar trend is observed for σ^*_{vm} until the normalised frequency becomes 2.4. At this frequency σ^*_{vm} exhibits a maximum reduction of 44%. However, σ^*_{vm} starts increasing slightly in the frequency range 2.4 to 3 when the Poisson's ratio of the interphase is 0.2 or 0.1. This change in behavior of σ^*_{vm} is due to the shift in the angular position of the maximum from 180° to 90°. This is illustrated in Figure 4.8 which shows the angular location at which the maximum value for σ^*_{vm} occurs for various frequencies.

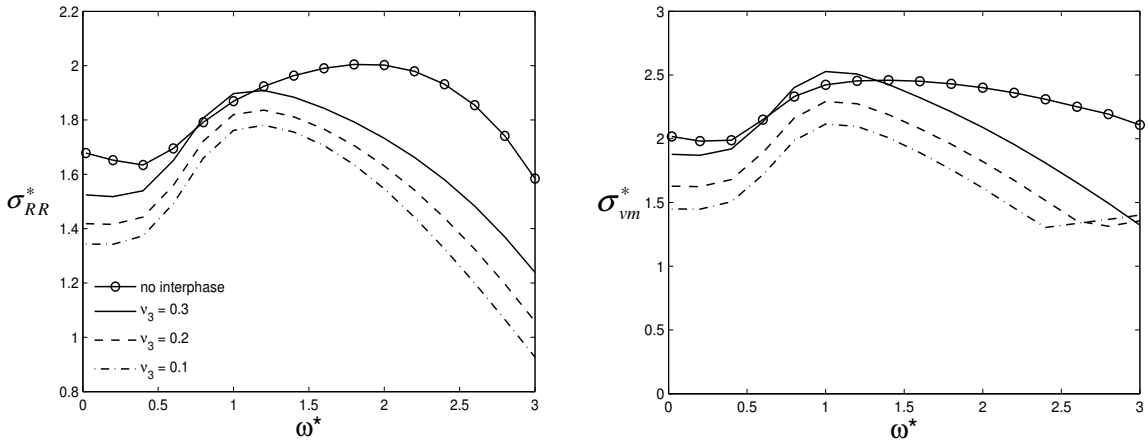

Figure 4.7 Effect of Poisson's ratio of the interphase on the stress concentration

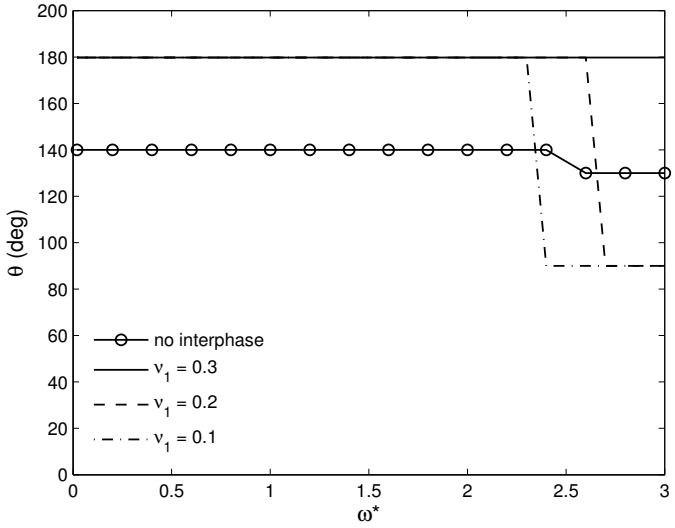

Figure 4.8 Angular location of maximum von Mises stress for different Poisson's ratios ($\mu_3/\mu_1 = 0.4$, $\rho_3/\rho_1 = 1$)

4.2.5. Effect of Density

Figure 4.9 shows the effect of density of the interphase layer for the case $\mu_3/\mu_1 = 0.4$ and $\nu_i = 0.1$. The density of the interphase, be it lower or higher than that of the matrix, seems to have little influence for normalised frequencies up to 2.2. At frequencies higher than 2.2, an interphase lighter than the matrix could cause a small reduction in stress concentration.

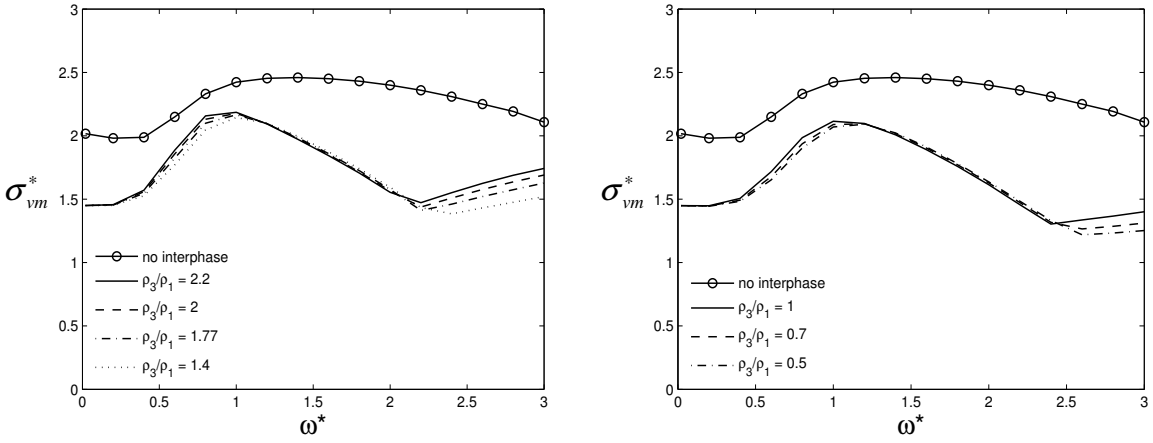

Figure 4.9 Effect of density of interphase layer on maximum von Mises stress ($\mu_3/\mu_1 = 0.4$, $v_3 = 0.1$, $v_2 = v_1 = 0.3$)

4.3. Conclusion

The effect of an interphase layer on the stress field caused by a dynamic loading in a Mg-matrix surrounding SiC-particle has been studied in this paper. It was found that the introduction of an interphase layer with an elastic modulus larger than the matrix or a functionally graded interphase layer cannot offer significant reduction of stress concentration. However, an interphase layer with an elastic modulus lower than the matrix caused substantial decrease in stress concentration at high frequencies. The amount of reduction depends strongly on the frequency. A reduction of 21% for σ_{RR}^{*} and 37% for σ_{vm}^{*} could be achieved at the normalized frequency of 3 through the introduction of an interphase layer whose modulus is 2.5 times lower than that of the matrix. The stress concentration could be further reduced by decreasing the Poisson's ratio of the interphase to 0.1. Here a maximum reduction of 44% for von Mises stress concentration can be achieved at the normalised frequency of 2.4.

5. Surface effects on the dynamic elastic state surrounding a nanosized spherical particle

5.1. Problem Formulation

In the bulk of the solids the equilibrium and constitutive equations are the same as those in the traditional elasticity theory Gurtin and Murdoch [37] and Gurtin *et a.l* [40]. Figure 5.1 shows geometry of a single spherical nano-particle of radius a embedded in an infinitely large matrix with *z-axis* as the symmetry axis. Owing to the geometry the problem is best described by spherical coordinates (R, ϕ, θ). The bulk material properties are given by Lamé constants λ_i and μ_i and mass density by ρ_i. The subscripts i = 1 and 2 donate matrix (medium 1) and nano-particle (medium 2). Spheroid is excited by time harmonic plane *SV* (shear) waves propagating in the *xz* plane, parallel to the axis of symmetry. On encountering the particle incident waves are reflected, refracted and scattered. The time variation is assumed to be of the form $e^{-i\omega t}$, where ω is the frequency of excitation. Only time-harmonic excitation is considered. Since all field quantities have the same time variation this term will be suppresses in all subsequent representations for notational convenience.

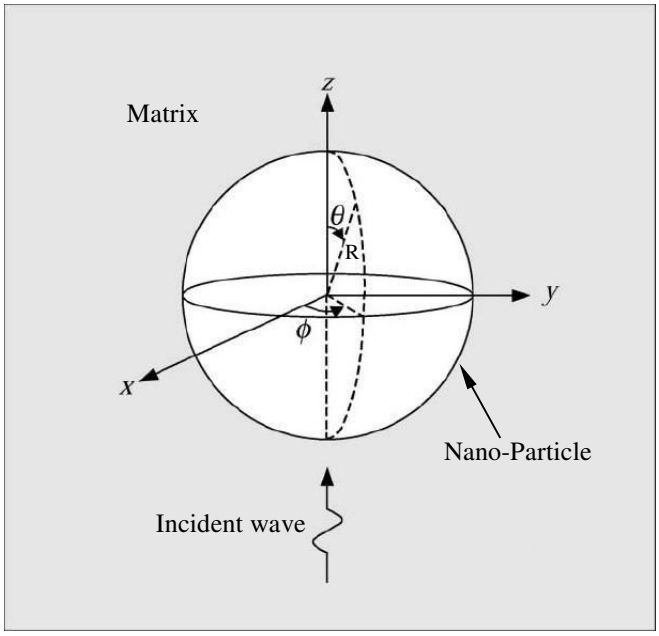

Figure 5.1 Schematic illustration of the general problem.

The nano-particle and matrix material is assumed to be homogeneous, linearly elastic, isotropic and fully bonded. Assuming a harmonic steady-state loading and from the theory of elasticity the displacement at any point within the bulk medium must satisfy the equation (2.1) of motion:

In the matrix the wave field consists of both incident and scattered waves while the particle consists of only refracted wave field. By denoting the incident and scattered waves by the superscripts *inc* and *sct* respectively, the displacement vector $\boldsymbol{U}$ in the matrix has contributions from both incident and scattered waves.

$$\boldsymbol{U} = \boldsymbol{U}^{inc} + \boldsymbol{U}^{sct} \tag{5.2}$$

While the incident wave field is known, the scattered wave field in the matrix and the refracted field in the particle is unknown.

Before writing the displacement and stress expressions for incident, scattered and refracted waves, the general expressions for displacement amplitudes of the equations (2.13) to (2.15) and stress amplitudes of the equations (2.42) to (2.47) are rewritten in the following form:

$$\bar{u}_R^n = a_{1n} c_{21} P_n^1 + a_{2n} c_{22} P_n^1 \tag{5.3}$$

$$\bar{u}_\theta^n = a_{1n} c_{23} \frac{dP_n^1}{d\theta} + a_{2n} c_{24} \frac{dP_n^1}{d\theta} + a_{3n} c_{25} \frac{P_n^1}{\sin\theta} \tag{5.4}$$

$$\bar{u}_\phi^n = a_{1n} c_{23} \frac{P_n^1}{\sin\theta} + a_{2n} c_{24} \frac{P_n^1}{\sin\theta} + a_{3n} c_{25} \frac{dP_n^1}{d\theta} \tag{5.5}$$

$$\bar{\sigma}_{RR}^n = a_{1n} c_2 P_n^1 + a_{2n} c_1 P_n^1 \tag{5.6}$$

$$\bar{\sigma}_{R\theta}^n = a_{1n} c_9 \frac{dP_n^1}{d\theta} + a_{2n} c_{10} \frac{dP_n^1}{d\theta} + a_{3n} c_{11} \frac{P_n^1}{\sin\theta} \tag{5.7}$$

$$\bar{\sigma}_{R\phi}^n = a_{1n} c_9 \frac{P_n^1}{\sin\theta} + a_{2n} c_{10} \frac{P_n^1}{\sin\theta} + a_{3n} c_{11} \frac{dP_n^1}{d\theta} \tag{5.8}$$

$$\begin{aligned} \bar{\sigma}_{\theta\theta}^n = {} & a_{1n} \left[c_3 P_n^1 + c_4 \frac{d^2 P_n^1}{d\theta^2} \right] + a_{2n} \left[c_5 P_n^1 + c_6 \frac{d^2 P_n^1}{d\theta^2} \right] \\ & + a_{3n} \left[c_{12} \frac{1}{\sin\theta} \left(\frac{dP_n^1}{d\theta} - \cot\theta P_n^1 \right) \right] \end{aligned} \tag{5.9}$$

$$\begin{aligned} \bar{\sigma}_{\phi\phi}^n = {} & a_{1n} \left[c_3 P_n^1 + c_4 \left(\cot\theta \frac{dP_n^1}{d\theta} - \frac{1}{\sin^2\theta} P_n^1 \right) \right] \\ & + a_{2n} \left[c_5 P_n^1 + c_6 \left(\cot\theta \frac{dP_n^1}{d\theta} - \frac{1}{\sin^2\theta} P_n^1 \right) \right] \\ & + a_{3n} \left[c_{12} \frac{1}{\sin\theta} \left(\cot\theta P_n^1 - \frac{dP_n^1}{d\theta} \right) \right] \end{aligned} \tag{5.10}$$

$$\bar{\sigma}^n_{\theta\phi} = a_{1n}c_4\frac{1}{\sin^2\theta}\left[(n-1)\cos\theta P^1_n - (n+1)P^1_{n-1}\right] + a_{2n}c_6\frac{1}{\sin^2\theta}\left[(n-1)\cos\theta P^1_n - (n+1)P^1_{n-1}\right] + a_{3n}c_{12}\frac{1}{\sin^2\theta}\left[\left(1^2 - n - \frac{1}{2}n(n-1)\sin^2\theta\right)P^1_n + (n+1)\cos\theta P^1_{n-1}\right] \tag{5.11}$$

where

$$c_1 = \frac{2\mu}{R^2}\left[\left(n^2 - n - \frac{1}{2}\beta^2R^2\right)Z_n(\alpha R) + 2\alpha R Z_{n+1}(\alpha R)\right] \tag{5.12}$$

$$c_2 = \frac{2\mu}{R^2}\frac{n(n+1)}{\beta}\left[(n-1)Z_n(\beta R) - \beta R Z_{n+1}(\beta R)\right] \tag{5.13}$$

$$c_3 = \frac{2\mu}{R^2}\left[\left(n + \alpha^2R^2 - \frac{1}{2}\beta^2R^2\right)Z_n(\alpha R) - \alpha R Z_{n+1}(\alpha R)\right] \tag{5.14}$$

$$c_4 = \frac{2\mu}{R^2}Z_n(\alpha R) \tag{5.15}$$

$$c_5 = \frac{2\mu}{R^2}\frac{1}{\beta}n(n+1)Z_n(\beta R) \tag{5.16}$$

$$c_6 = \frac{2\mu}{R^2}\frac{1}{\beta}\left[(n+1)Z_n(\beta R) - \beta R Z_{n+1}(\beta R)\right] \tag{5.17}$$

$$c_9 = \frac{2\mu}{R^2}\left[(n-1)Z_n(\alpha R) - \alpha R Z_{n+1}(\alpha R)\right] \tag{5.18}$$

$$c_{10} = \frac{2\mu}{R^2}\frac{1}{\beta}\left[\left(n^2 - n - \frac{1}{2}\beta^2R^2\right)Z_n(\beta R) + \beta R Z_{n+1}(\beta R)\right] \tag{5.19}$$

$$c_{11} = \frac{\mu}{R}\left[(n-1)Z_n(\beta R) - \beta R Z_{n+1}(\beta R)\right] \tag{5.20}$$

$$c_{12} = \frac{2\mu}{R}Z_n(\beta R) \tag{5.21}$$

$$c_{21} = \frac{n}{R}Z_n(\alpha R) - \alpha Z_{n+1}(\alpha R) \tag{5.22}$$

$$c_{22} = n(n+1)\frac{Z_n(\beta R)}{\beta R} \tag{5.23}$$

$$c_{23} = \frac{Z_n(\alpha R)}{R} \tag{5.24}$$

$$c_{24} = (n+1)\frac{Z_n(\beta R)}{\beta R} - Z_{n+1}(\beta R) \tag{5.25}$$

$$c_{25} = Z_n(\beta R) \tag{5.26}$$

In the above and the equations that follow, the argument (cosθ) for P^1_n and its derivatives has been suppressed for notational convenience.

The incident wave displacement and stresses are described in section 3.1.3.

The expressions for scattered wave displacements and stresses are given in section 3.1.4 equations (3.32) to (3.34) and (3.38) to (3.40). Since only three stress components for scattered wave are given, all six can be obtained from equations (5.3) to (5.11) by replacing the function Z_n by $h_n^{(1)}$ in the expressions for c_1, c_2,..., etc with α and β being those of matrix.

5.1.1. Refracted waves in the particle

The refracted waves, being confined in the spherical particle, are standing waves. The potentials χ, ψ and φ in the equation (2.2) are now given by:

$$\chi^{rfr}(R,\phi,\theta) = \sum b_{1n} j_n(\alpha_2 R) P_n^1 \cos\phi \tag{5.27}$$

$$\psi^{rfr}(R,\phi,\theta) = \sum b_{2n} j_n(\beta_2 R) P_n^1 \cos\phi \tag{5.28}$$

$$\varphi^{rfr}(R,\phi,\theta) = \sum b_{3n} j_n(\beta_2 R) P_n^1 \sin\phi \tag{5.29}$$

where superscript *rfr* refers to the refracted wave, b_{1n}, b_{2n} and b_{3n} are as yet unknown amplitude coefficients and subscript 2 refers to the particle medium,

By substituting equations (5.27) to (5.29) into equation (2.2) and the resulting expressions into equations (2.13) to (2.15) and equations (2.30) to (2.35) the displacements and stresses in spherical coordinate system due to refracted field in the particle are obtained. These expressions are given in equations (5.3) to (5.11) by replacing the function Z_n by j_n in the expressions for c_1, c_2,...,etc with α and β being those of a particle.

5.1.2. Surface/interface elasticity

In the surface/interface elasticity theory an interface is considered as a negligibly thin surface or a membrane glued to the underlying bulk materials without slipping and its inertia can be neglected for dynamic problems. The elastic constants of the membrane are different from those of its adjoining materials and are given by constants μ^s and λ^s. This leads to a set of nonclassical boundary conditions at the interface. Basic equations of the surface/interface elasticity theory are reviewed here.

The relation between surface energy density $\Gamma(\varepsilon_{\alpha\beta})$ and the surface stress tensor $\sigma^s_{\alpha\beta}$ is

$$\sigma^s_{\alpha\beta} = \imath^0 \delta_{\alpha\beta} + \frac{\partial \Gamma}{\partial \varepsilon^s_{\alpha\beta}} \tag{5.30}$$

where superscript *s* denotes the surface, $\imath^0$ is the residual surface stress under unstrained conditions, $\delta_{\alpha\beta}$ is the Kronecker delta and $\varepsilon^s_{\alpha\beta}$ the second rank tensor of the surface/interface strain.

The equilibrium condition on the surface can be written as

$$t_\alpha + \sigma^s_{\beta\alpha,\beta} = 0, \quad \sigma_{ij} n_i n_j = \sigma^s_{\alpha\beta} \kappa_{\alpha\beta} \tag{5.31}$$

$$\sigma^s_{\alpha\beta} = \iota^0 \delta_{\alpha\beta} + \left(\lambda^s + \iota^0\right) \varepsilon_{\gamma\gamma} \delta_{\alpha\beta} + 2\left(\mu^s - \iota^0\right) \delta_{\alpha\gamma} \varepsilon_{\gamma\beta} \tag{5.32}$$

where superscript *s* denotes the surface, t_α is the tangential component of the traction $t_i = \left\langle \sigma^s_{ij} \right\rangle n_j$ in the direction χ_α , $\left\langle \sigma_{ij} \right\rangle$ is the change of the bulk stress tensor across the surface/interface, $\sigma^s_{\alpha\beta}$ is the stress tensor of the surface/interface, n_i is the normal vector of the surface/interface, $\kappa_{\alpha\beta}$ is the surface/interface curvature.

For the isotropic surface/interface the stresses are given by:

$$\sigma^s_{\alpha\beta} = \lambda^s \varepsilon^s_{\gamma\gamma} \delta_{\alpha\beta} + 2\mu^s \varepsilon^s_{\alpha\beta} \tag{5.33}$$

5.1.3. Continuity conditions

The surface/interface strains in spherical coordinates in terms of the matrix stresses in the bulk are given by

$$\varepsilon^s_{\theta\theta} = \varepsilon^1_{\theta\theta} = \frac{1}{E}\left(\sigma^1_{\theta\theta} - v\sigma^1_{\phi\phi} - v\sigma^1_{RR}\right) \tag{5.34}$$

$$\varepsilon^s_{\phi\phi} = \varepsilon^1_{\phi\phi} = \frac{1}{E}\left(\sigma^1_{\phi\phi} - v\sigma^1_{\theta\theta} - v\sigma^1_{RR}\right) \tag{5.35}$$

$$\varepsilon^s_{\theta\phi} = \frac{\sigma^1_{\theta\phi}}{2G} \tag{5.36}$$

where superscript 1 refers to the matrix medium. *E*, *G* and *v* donate Young's modulus, shear modulus and Poisson's ratio of the matrix respectively.

The stress-strain relationships for the surface/interface from equation (5.33) are given by:

$$\sigma^s_{\theta\theta} = \lambda^s \left(\varepsilon^s_{\theta\theta} + \varepsilon^s_{\phi\phi}\right) + 2\mu^s \varepsilon^s_{\theta\theta} \tag{5.37}$$

$$\sigma^s_{\phi\phi} = \lambda^s \left(\varepsilon^s_{\theta\theta} + \varepsilon^s_{\phi\phi}\right) + 2\mu^s \varepsilon^s_{\phi\phi} \tag{5.38}$$

$$\sigma^s_{\theta\phi} = 2\mu^s \varepsilon^s_{\theta\phi} \tag{5.39}$$

Substituting equations (5.40) to (5.42) into equations (5.37) to (5.39) and resulting expressions into equilibrium condition of equation (5.33) the surface effects on the interface of the nano-sized spherical particle of radius *a* and the matrix are obtained:

$$\left(\sigma_{RR}^{1}-\sigma_{RR}^{2}\right)=\frac{1}{a}\left(\sigma_{\theta\theta}^{s}+\sigma_{\phi\phi}^{s}\right) \tag{5.40}$$

$$\left(\sigma_{R\theta}^{1}-\sigma_{R\theta}^{2}\right)=-\left(\frac{1}{a}\frac{\delta\sigma_{\theta\theta}^{s}}{\delta\theta}+\frac{1}{a}\left(\sigma_{\theta\theta}^{s}-\sigma_{\phi\phi}^{s}\right)\cot\theta+\frac{1}{a}\frac{1}{\sin\theta}\frac{\delta\sigma_{\theta\phi}^{s}}{\delta\phi}\right) \tag{5.41}$$

$$\left(\sigma_{R\phi}^{1}-\sigma_{R\phi}^{2}\right)=-\left(\frac{\delta\sigma_{\theta\phi}^{s}}{\delta\theta}+\frac{1}{a}2\cot\theta\,\sigma_{\theta\phi}^{s}+\frac{1}{a}\frac{1}{\sin\theta}\frac{\delta\sigma_{\phi\phi}^{s}}{\delta\phi}\right) \tag{5.42}$$

where $\sigma_{RR}^{1}=\sigma_{RR}^{inc}+\sigma_{RR}^{sct}$ and same applies for $\sigma_{R\theta}^{1}$ and $\sigma_{R\phi}^{1}$. Superscript 2 refer to the refracted wave field in the particle.

The displacement continuity conditions on the interface require that:

$$\bar{u}_{R}^{1}=\bar{u}_{R}^{2} \tag{5.43}$$

$$\bar{u}_{\theta}^{1}=\bar{u}_{\theta}^{2} \tag{5.44}$$

$$\bar{u}_{\phi}^{1}=\bar{u}_{\phi}^{2} \tag{5.45}$$

Where $\bar{u}_{R}^{1}=\bar{u}_{R}^{inc}+\bar{u}_{R}^{sct}$ and the same applies for $\bar{u}_{\theta}^{1}$ and $\bar{u}_{\phi}^{1}$.

Substituting equations (5.34) to (5.36) into (5.37) to (5.39) and the resulting expressions into equations (5.40) to (5.42) the interface stress conditions in terms of bulk stresses are obtained

$$\sigma_{RR}^{1}-\sigma_{RR}^{2}=2\left(k_1+k_2\right)\left(1-v_1\right)\left(\sigma_{\theta\theta}^{1}+\sigma_{\phi\phi}^{1}\right)-4v_1\left(k_1+k_2\right)\sigma_{RR}^{1} \tag{5.46}$$

$$\begin{aligned}\sigma_{R\theta}^{1}-\sigma_{R\theta}^{2}=&\left[\left(1-v_1\right)k_1+2k_2\right]\frac{\delta\sigma_{\theta\theta}^{1}}{\delta\theta}-\left[\left(1-v\right)k_1-2k_2\right]\frac{\delta\sigma_{\phi\phi}^{1}}{\delta\theta}\\&+2v_1\left(k_1+k_2\right)\frac{\delta\sigma_{RR}^{1}}{\delta\theta}-2k_2\left(1+v\right)\left(\sigma_{\theta\theta}^{1}+\sigma_{\phi\phi}^{1}\right)\\&+2k_2\left(1+v_1\right)\frac{1}{\sin\theta}\sigma_{\theta\phi}^{1}\end{aligned} \tag{5.47}$$

$$\begin{aligned}\sigma_{R\phi}^{1}-\sigma_{R\phi}^{2}=&\,2k_2\left(1+v_1\right)\frac{\delta\sigma_{\theta\phi}^{1}}{\delta\theta}+2\sigma_{\theta\phi}^{1}\cot\theta\\&+\frac{1}{\sin\theta}\left\{\left[\left(1-v_1\right)k_1-2k_2\right]\sigma_{\theta\theta}^{1}+\left[\left(1-v_1\right)k_1+2k_2\right]\sigma_{\phi\phi}^{1}-v_1\left(k_1+k_2\right)\sigma_{RR}^{1}\right\}\end{aligned} \tag{5.48}$$

where k_1 and k_2 are dimensionless parameters

$$k_1 = \frac{\lambda^s}{E_1 a} \quad , \qquad k_2 = \frac{\mu^s}{E_1 a} \tag{5.49}$$

With a particle size approaching macroscopic values the terms μ^2 and λ^2, and consequently k_1 and k_2 approach zero. The surface/interface effects disappear in this case and the equations (5.40) to (5.42) reduce to the solution of the classical elasticity. In view of the modelling different material properties of the matrix and the inhomogeneity, as the ratio $\mu_2/\mu_1 \to 0$ the inhomogeneity becomes a cavity, however as $\mu_2/\mu_1 \to \infty$ the inhomogeneity becomes a rigid inclusion.

By invoking the orthogonality relations of Legendre polynomials in equations (5.43) to (5.48), one obtains, for each n ≥ 1, two sets of simultaneous algebraic equations which can be expressed in matrix form as:

$$[E]\{b_n\} = \{f\} \tag{5.50}$$

$$[P]\{d_n\} = \{q\} \tag{5.51}$$

where the vector $\{b_n\}$ contains the unknown coefficients $[a_{1n}\ a_{2n}\ b_{1n}\ b_{2n}]^T$ and vector $\{d_n\}$ contains the unknown coefficients $[a_{3n}\ b_{3n}]^T$. The elements of $[E]$ and $[P]$ and vectors $\{f\}$ and $\{q\}$ are given in the Appendix D. Equations (5.50) and (5.51) can be solved to determine the coefficients a_{1n}, a_{2n}, a_{3n}, b_{1n}, b_{2n} and b_{3n}.

5.2. Numerical results and discussion

In the absence of the nano-particle, the stress field at any point in the medium can be expressed in rectangular coordinates as

$$\sigma_{xz} = \sigma_{zx} = i\mu_1\beta_1\, e^{i\beta_1 z - i\omega t} \tag{5.52}$$

where subscript 1 refers to the matrix medium. With all other stress components being zero the maximum value of the stresses is $\mu_1\beta_1$.

In the presence of the nano-particle, the stress field is significantly different from that given by equation (5.52) due to scattering. The nonzero stresses on the surface of the particle are σ_{RR}, $\sigma_{R\phi}$ and $\sigma_{R\theta}$. The results have the general form

$$\sigma = (R + iI)\, f(\phi)\, e^{-i\omega t} \tag{5.53}$$

where $f(\phi)$ is either $\cos\phi$ or $\sin\phi$, the real part R represents the solution at $t = 0$ and $T/2$, and the imaginary part I represents the solution at $t = T/4$ and $3T/4$, T being the period of excitation. The absolute value $(R^2 + I^2)^{1/2}$ is the maximum stress that occurs at some instant depending on the phase-shift.

These stresses are expressed in dimensionless form by normalizing with respect to the maximum value of the incident stress field, $\mu_1\beta_1$:

$$\sigma_{ij}^{*} = \frac{|\sigma_{ij}|}{\mu_1\beta_1} \qquad i, j = t, \phi \tag{5.54}$$

Thus the values of σ_{ij}^{*} can be considered as dynamic stress concentration factors. They depend on the aspect ratio of the particle and the frequency of excitation; the latter is expressed in non-dimensional form through

$$\omega^{*} = \omega a\sqrt{\frac{\rho_1}{\mu_1}} \tag{5.55}$$

where a, as defined earlier, is the radius of the nano-particle in the ***x-y*** plane.

The nature of the dynamic excitation is better appreciated by considering the limiting static case. When the frequency approaches zero, the applied stress field at infinity approaches

$$\sigma_{xz} = \sigma_{zx} = \sigma_0 \tag{5.56}$$

$$\sigma_{xx} = \sigma_{yy} = \sigma_{zz} = \sigma_{xy} = \sigma_{yz} \tag{5.57}$$

where σ_0 is a constant. The stress field of equations (5.56) and (5.57) is pure shear. Thus, the results presented herein are for the dynamic counterpart of this shear load.

In the following examples the effects of parameter k_2 and normalized frequency ω^{*} on the stress concentration values in the matrix at the interface has been examined. Parameter k_1=0 and $\nu_1 = \nu_2$=0.3. In many practical applications of particulate-reinforced composites a common observation is that failure often initiates in the matrix at the interface between the particle and matrix which. This confirms the high stress concentration values obtained in this study for different stress components. Particles often have considerably larger modulus and substantially higher yield stress values than the matrix and initiation of failure will therefore most likely take place within the matrix. For this reason, we will henceforth limit our attention to the state of stress in the matrix at the interface only.

Figures 5.1 to 5.2 illustrate the angular distribution of σ_{RR}^{*} and $\sigma_{R\phi}^{*}$ for six k_2 values and normalized frequencies of ω^{*} = 0.1 and 3. The other stress values are not shown since their values consistently fall between those of σ_{RR}^{*} and $\sigma_{R\phi}^{*}$. It can be seen that both

nondimensional frequency and k_2 have significant influence on stress distribution. At a very small normalized frequency of 0.1 the wavelength of the incident wave is much larger than the nano-particle radius and hardly any dynamic effect is expected. The dynamic solution can be regarded as quasi-static and dynamic load is given approximately by equations (5.56) and (5.57) which exhibit symmetry with respect to the z = 0 plane. As seen in figures 5.1 to 5.2 the resulting stress field is also symmetric about this plane for all k_2 values. The maximum values of σ^*_{RR} occur at $\theta/\pi = 0.25, 0.75$ and that of $\sigma^*_{R\phi}$ occur $\theta/\pi = 0$ and 1. The influence of k_2 on σ^*_{RR} and $\sigma^*_{R\phi}$ stress concentration values is the highest at these same values of θ/π. The most significant reduction of σ^*_{RR} stress concentration values occur at k_2 values greater than 1. For values lower than 1 the stress concentration reduction is not significant. The effect of k_2 values on $\sigma^*_{R\phi}$ stress concentration values is less than for σ^*_{RR}. With increasing k_2 values in the range below 1 show more or less the same stress concentration reduction as values above 1, which is different to that of σ^*_{RR}.

For the normalized frequency of 3.0 the wavelength is about the same size as the diameter of the particle and a great deal of scattering occurs (figures 5.2) which results in a stress distribution being quite different from the quasi-static solution. The dynamic stress concentration distribution is no longer symmetric about the $\theta/\pi = 0.5$. The influence of k_2 values on both σ^*_{RR} and $\sigma^*_{R\phi}$ occur at the peak stress concentration values. The effect of k_2 values on σ^*_{RR} occur across greater angle range at higher normalized frequency than is the case at quasi-static loading. The increasing k_2 values result in higher $\sigma^*_{R\phi}$ stress concentration values at θ/π range below 0.65.

The radial distribution of σ^*_{RR}, $\sigma^*_{R\phi}$ and $\sigma^*_{R\theta}$ in the matrix at $\theta/\pi = 0.75$ is illustrated in figures 5.3 and 5.4 for $\omega^* = 0.1$ and 2. The stress concentration of $\sigma^*_{R\theta}$ in figure 5.3 is not shown as its values fall far below that of $\sigma^*_{R\phi}$. As the radius increase all three stress components converge to incident field values as expected. The maximum values of the stresses occur at or near the interface indicating the most likely location of the matrix failure. The stress concentration values are mostly affected by nano-sized particle properties at or very near the interface. This effect then relatively quickly disappears as distance from the particle increases, as expected.

The influence of the k_2 parameter and the normalized frequency on the peak stress concentration values for σ^*_{RR} and $\sigma^*_{R\phi}$ is shown in figure 5.5. The increasing k_2 values shows a reduction of σ^*_{RR} peak stress concentration values throughout the frequency range. A significant decrease occurs for k_2 values greater than 1, which is reflected in figures 5.1 and 5.2. The peak stress concentration values of $\sigma^*_{R\phi}$ experience a drop for k_2 values lower than 1 throughout the frequency range. However the values show an increase for k_2 values greater than 1 at $\omega^* > 0.7$.

Figures 5.6 and 5.7 show the effect of stiffness ratio μ^* of nano-particle to matrix on the peak stress concentration values of σ^*_{RR} and $\sigma^*_{R\phi}$ that occur over a range of normalized frequencies $0 < \omega^* < 3$. Values of figure 3.6 and 3.7 are computed for k_2 value of 0.5 and 2 respectively. It is evident that the higher particle stiffness value result in a steady increase in peak stress concentration values of σ^*_{RR} throughout the considered normalized frequency range and for both k_2 values. This increase in stress concentration values becomes progressively higher with the increase in frequency. The values of $\sigma^*_{R\phi}$ however exhibit initially a reduction in stress concentration values throughout the frequency range considered as the particle-matrix stiffness ratio increases from a very low ratio. As the particle-matrix stiffness ratio increases further the effect is reversed showing quite a large increase in stress concentration values. The greatest effect is shown at very low frequencies.

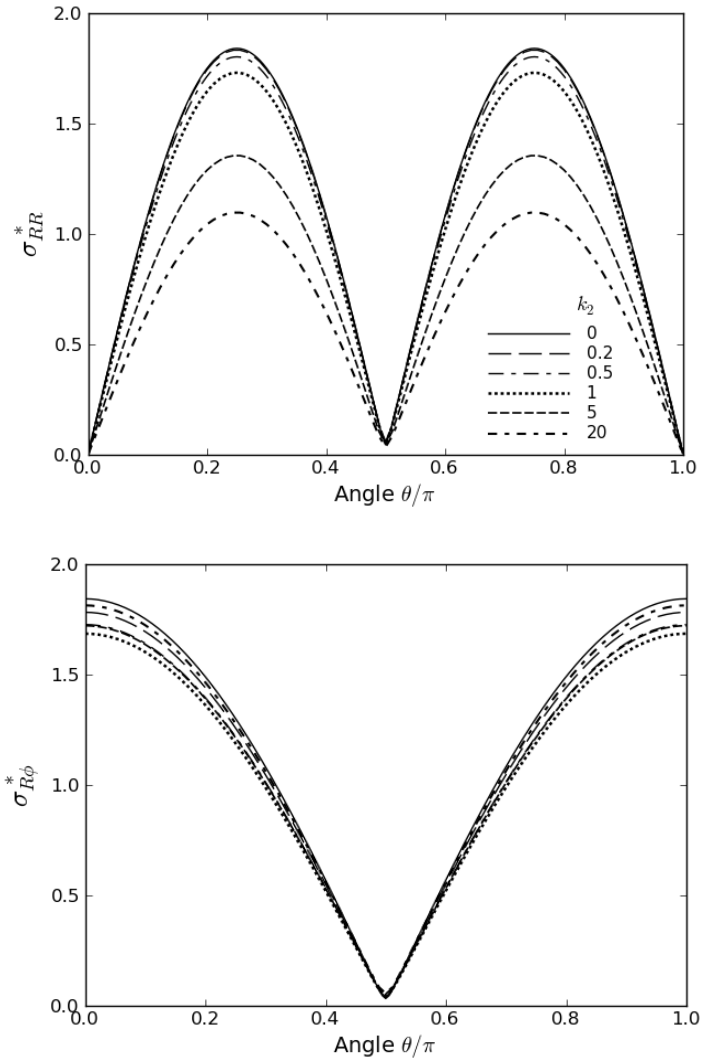

Figure 5.1 Angular distribution of stress concentration in the matrix at the nano-particle matrix interface for $\omega^* = 0.1$ ($\rho^*=1$, $\mu^*=8$, $\nu_1 = \nu_2=0.3$)

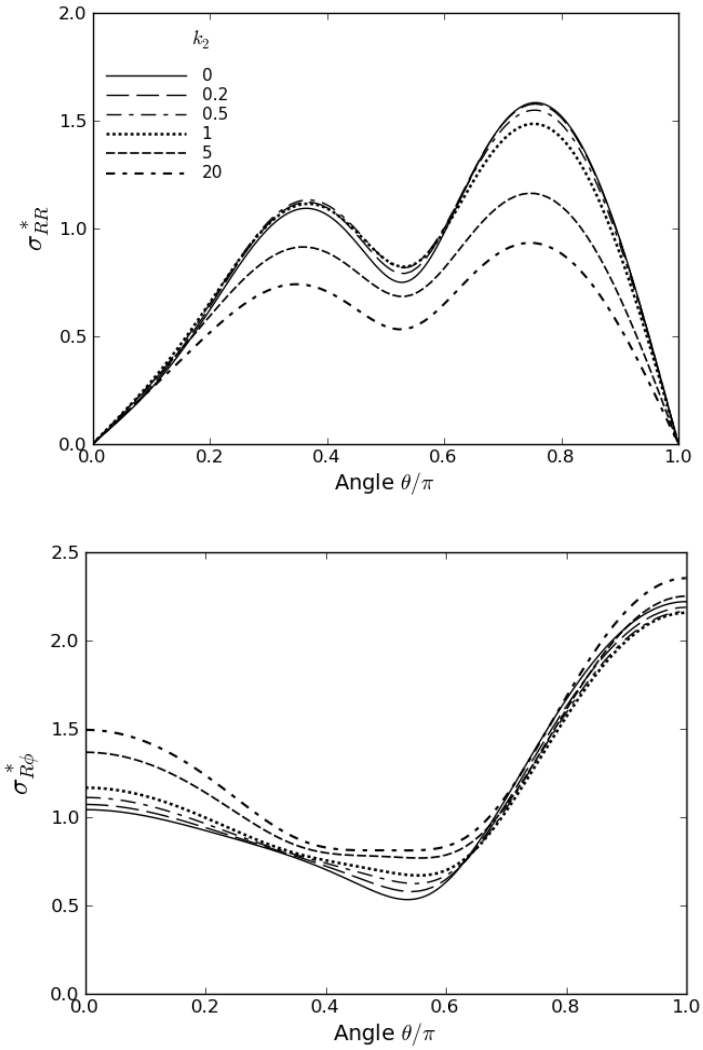

Figure 5.2 Angular distribution of stress concentration in the matrix at the nano-particle matrix interface for $\omega^* = 3$ ($\rho^*=1$, $\mu^*=8$, $\nu_1 = \nu_2 = 0.3$)

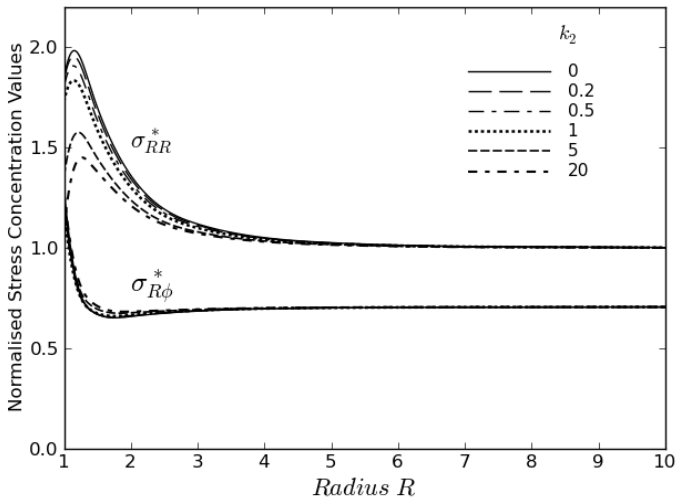

Figure 5.3 Radial distribution of stress concentration in the matrix at $\theta/\pi = 0.75$ angle for $\omega^* = 0.1$ (ρ^*=1, μ^*=8, $\nu_1 = \nu_2$=0.3)

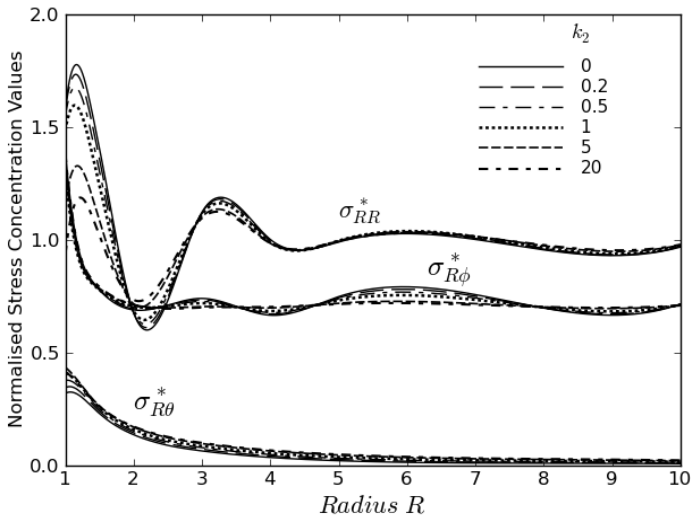

Figure 5.4 Radial distribution of stress concentration in the matrix at $\theta/\pi = 0.75$ angle for $\omega^* = 2$ (ρ^*=1, μ^*=8, $\nu_1 = \nu_2$=0.3)

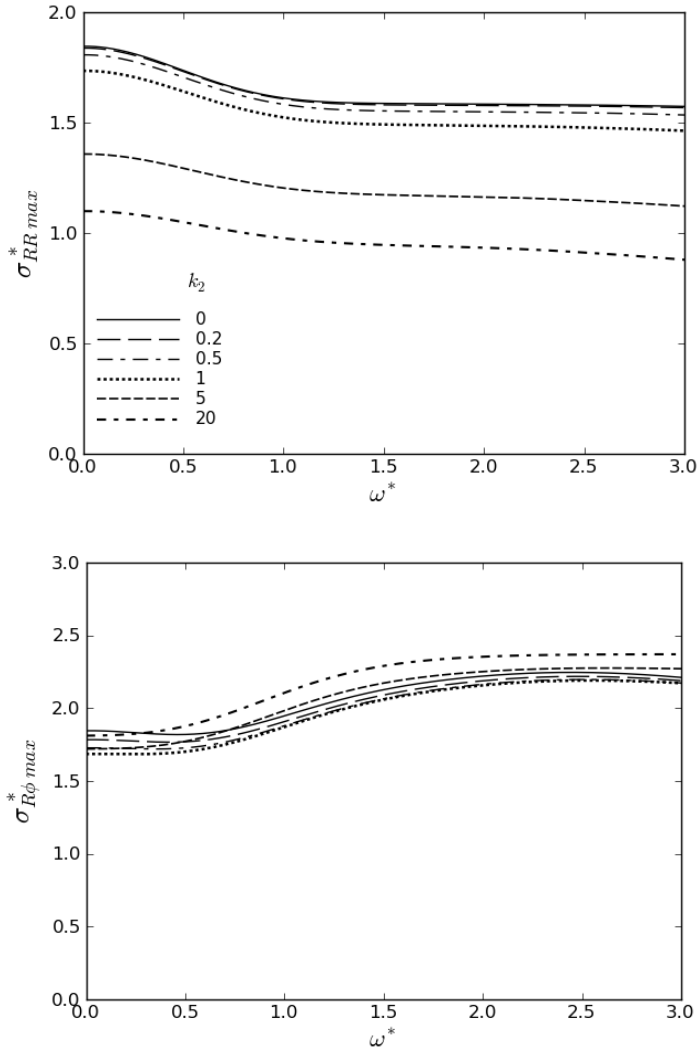

Figure 5.5 Effect of k_2 on the peak stress concentration values in the matrix at the nano-particle matrix interface (ρ^*=1, μ^*=8, v_1= v_2=0.3)

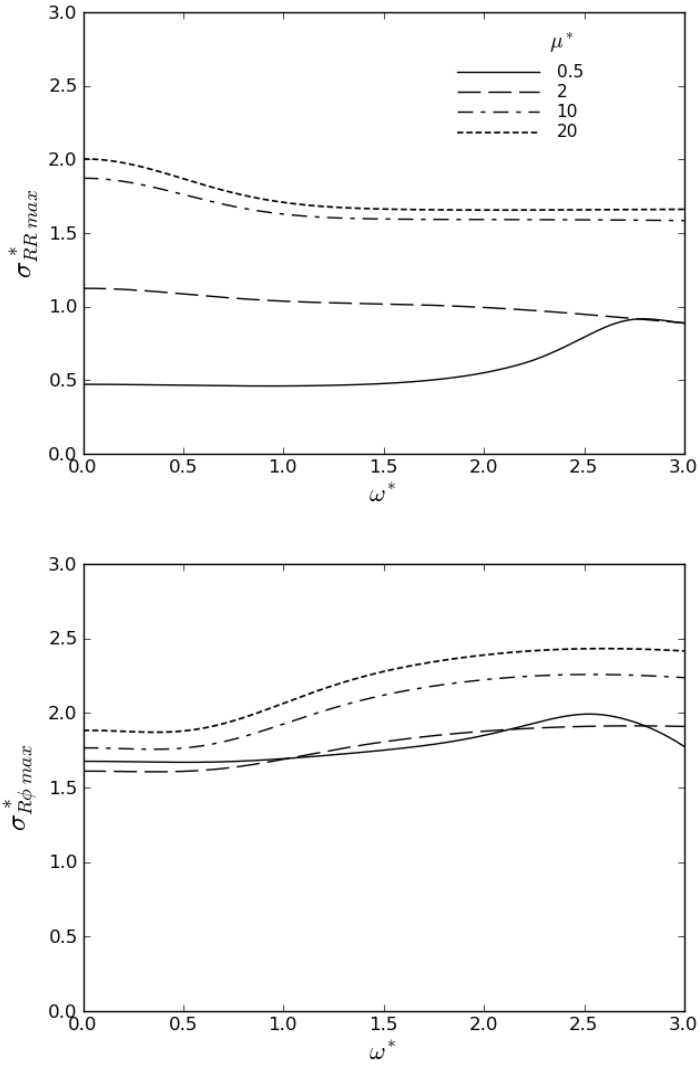

Figure 5.6 Effect of nano-particle/matrix stiffness ratio μ^* on the peak stress concentration values in the matrix at the particle matrix interface for k_2 =0.5 (ρ^*=1, ν_1= ν_2=0.3)

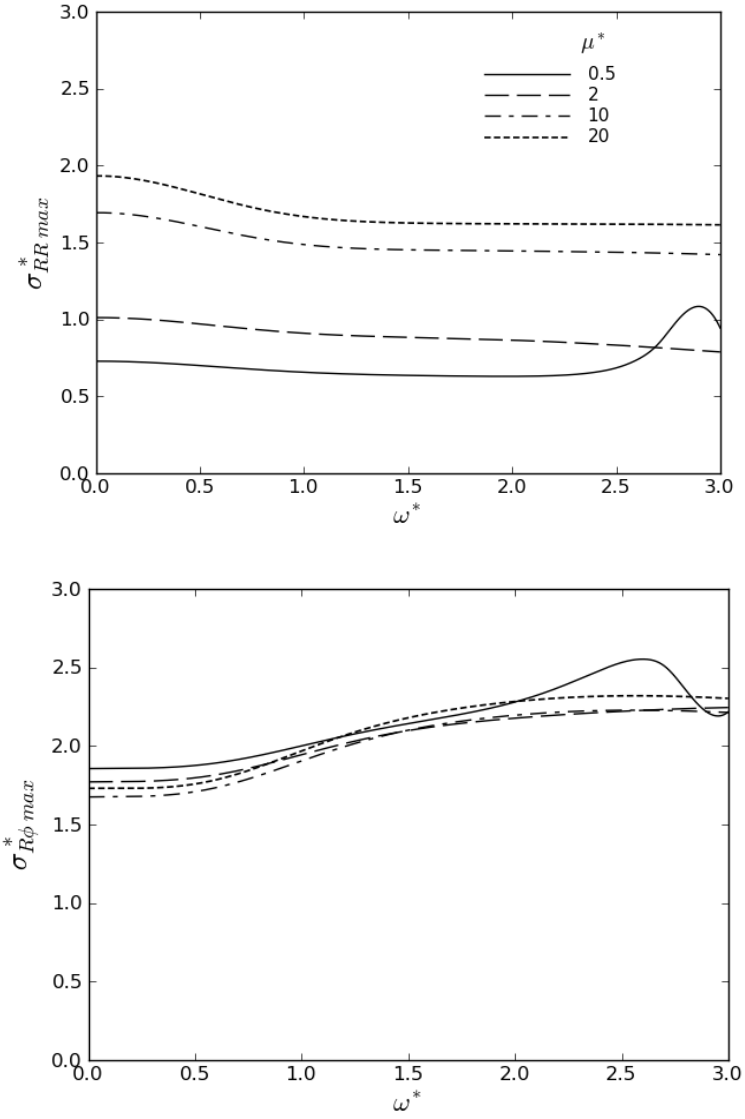

Figure 5.7 Effect of nano-particle/matrix stiffness ratio μ^* on the peak stress concentration values in the matrix at the particle matrix interface for k_2 =2 (ρ^*=1, ν_1= ν_2=0.3)

5.3. Conclusion

The study presents the effect of surface/interface elasticity on the dynamic stress field at the interface of the nanosized particle and the matrix due to a shear wave loading. It has been shown that the dynamic stress field at the particle-matrix interface is significantly affected by surface/interface elasticity as the particle size reduces to nanometers. The surface/interface effect is localized to a region at or very near the interface and quickly disappears away from interface. The increasing surface elastic constant μ^s can significantly reduce the stress concentration values concentration values at the nano-particle matrix interface.

6. Summary and final conclusion

The study deals with determining stress concentration in a particle reinforced composite at the particle-matrix interface as a result of interaction with elastic waves. Stress concentration at the interphase has been directly linked to formation of microcracks that eventually lead to failure. The investigation here analysed three interrelated problems by expanding techniques previously developed. All the analysis assumed low concentration of particles and therefore interaction of neighboring particles was ignored. All the materials are assumed linear elastic and perfectly bonded to each other. The investigation considered the effects of prolate spheroidal shape of a particle, nanoparticle surface/interface energy and particle-matrix interphase layers on dynamic stress concentration.

Since the analysis of the dynamic stress concentration around a particle due to dynamic waves is limited to a simple spherical shape, a hybrid technique was used. The technique is an extension of the already developed hybrid technique for axisymmetric loading to incorporate three dimensionality of asymmetric shear loading. It uses the finite element method with spherical wave functions. The analysis showed that the higher aspect ratios of the spheroidal particle result in increase in dynamic stress concentration. The increase however depends on both frequency of incident wave and aspect ratio. At higher wave frequencies, high values of spheroidal particle stiffness can result in 147% increase in peak stress concentration from the quasi-static values.

As the interphase layer in MMCs either occurs naturally or is intentionally introduced it is important to consider its effect on dynamic stress concentration. It is desirable to also investigate the properties of the interphase layer to potentially reduce the dynamic stress concentration at the particle-matrix interface. The study considered interphase effect in a Mg-matrix surrounding a SiC-particle. Both functionally graded and constant property interphase layers were considered. The analysis showed that the functionally graded interphase layer does not offer any significant stress concentration reduction. However a constant property interphase layer with elastic modulus and Poisson's ratio lower than the matrix can significantly reduce the stress concentration.

Stress states of the materials at nanoscale are found to differ from those at macroscale. This variation of the material behavior around the free surface or interface, as structures reduce to nano-meters has mainly contributed to Surface/interface energy. Previous two studies outlined in the paragraphs above have been extended here to include free surface/interface effects as the particle size reduces to nanometers. The nano-particle was subject to shear dynamic waves and by considering the effects of surface/interface elasticity, stress concentration values at the interface with matrix were obtained. The results showed that Surface/interface elasticity of the nanosized particle has a significant effect on dynamic stress field at the particle-matrix interface. The increasing surface elastic constant μ^s greatly reduces the stress concentration values at the nano-particle matrix interface. This effect is however localized near the interface and quickly disappears away from interface.

The findings show that the particle shape, particle size, interphase layer properties as well as particle and matrix properties all have a significant influence on dynamic stress concentration at the particle-matrix interface.

References

[1] www.globalspec.com/reference/69955/203279/chapter-15-composite-materials. Figure 15.1: Different types of reinforcement for composites.

[2] www.tms.org/pubs/journals/JOM/0104/Rawal-0104.html. Figure 1. Photo courtesy of **U.S. Air Force**/**NASA**.

[3] www.cmt-ltd.com/html/mat_1.htm. Metal matrix composites, Figure Title: Properties of AMCs versus conventional alloys.

[4] ASM Handbook, Vol 21 Composites, 2001.

[5] Davidson DL. The effect of particulate SiC on fatigue crack growth in a cast-extruded aluminium alloy composite. *Metalurgicall and Materials Transactions, 1991, vol. 22, pp. 97-209.*

[6] Sternberg E. Three-dimensional stress concentrations in the theory of elasticity. *Applied Mechanics Rev, 1958, vol. 11, pp. 1-5.*

[7] Neuber H, Hahn HG. Stress concentration in scientific research and engineering. *Applied Mechanics Rev, 1966, vol. 19, pp. 187-286.*

[8] Tan SC. Stress concentrations laminated composites. Lancaster, PA: *Technomic Publishing Co., 1994.*

[9] Prokic, A, Lukic, D, Anagnosti, P. Stress – strain field around elliptic cavities in elastic continuum. *European Journal of Mechanics, 2009, 28, 86-93.*

[10] Wang Z, Chen TK, Lloyd DJ. Stress distribution in particulate reinforced metal matrix composites subjected to external load. *Metalurgicall and Materials Transactions, 1993, vol. 24A, pp. 197-207.*

[11] Agarwal BD, Broutman LJ. Three-dimensional finite element analysis of spherical particle composites. *Fiber Science and Technology, 1974, vol. 7, pp. 63-72.*

[12] Kassam ZHA, Zhang RJ, Wang Z. Finite element simulation to investigate interaction between crack and particulate reinforcements in metal-matrix composites. *Materials Science and Engineering, 1995, vol. A203, pp. 286-299.*

[13] Pao YH, Mow CC. Diffraction of elastic waves and dynamic stress concentrations. *New York: Crane and Russak, 1973.*

[14] Bogan SD, Hinders MK. Dynamic stress concentrations in fiber-reinforced composites with interface layers. *Journal of Composite Materials, 1993, vol. 27, pp. 1272-1312.*

[15] Ying CF, Truell R. Scattering of a plane longitudinal wave by a spherical obstacle in an isotropically elastic solid. *Journal of Applied Physics, 1956, vol. 27, pp. 1086-1184.*

[16] Bostrom A. Scattering by a smooth elastic obstacle. *Journal of Acoustic Society of America, 1980, vol. 67, pp. 1904-1917.*

[17] Shindo Y, Nozaki H, Datta SK. Effect of interface layers on elastic wave propagation in a metal matrix composite reinforced by particles. *Journal of Applied Mechanics, 1995; 62; 178-85.*

[18] Paskaramoorthy R, Meguid SA. Large internal stresses in particle-reinforced composites subjected to dynamic loads. *Journal of Composite Science and Technology, 1999; vol. 59: pp. 1361-67.*

[19] Paskaramoorthy R, Kienhöfer F, Chandler HD. The response of particle-reinforced composites to asymmetric dynamic loading. *Journal of Composite Science and Technology, 2002, vol. 62, pp. 223-232.*

[20] Datta, SK. Diffraction of plane elastic waves by ellipsoidal inclusions. *Journal of Acoustic Society of America, 1997, 61, 1432-1537.*

[21] Willis, JR. A polarization approach to the scattering of elastic waves – I. Scattering by a single inclusion. *Journal of Mechanics and Physics of Solids, 1980, 28, 287-305.*

[22] Paskaramoorthy R, Datta SK, Shah AH. Effect of interface layers on scattering of elastic waves. *Journal of Applied Mechanics, 1988; 55: 871-8.*

[23] Olsson, P, Datta, SK., and Bostrom, A. Elastodynamic scattering from inclusions surrounded by thin interface layers. *Journal of Applied Mechanics, 1990, 57, 672-676.*

[24] Meguid, SA, Wang, XD. Wave scattering from partially-debonded inhomogeneities in advanced ceramics. *Presented at the 1997. Joint ASME, ASCE and SES Summer Meeting, 29 June-2 July, Northwestern University.*

[25] R. Paskaramoorthy, F. Kienhöfer, and S. A. Meguid . "The Dynamic Stress Field in the Matrix Surrounding a Spheroidal Particle". *Journal of Composite Materials, Aug 2002; vol. 36: pp. 1803 - 1824.*

[26] Madhukar MS, Drzal LT. Fiber-matrix adhesion and its effects on composite mechanical properties: I. Inplane and interlaminar shear behavior of graphite/epoxy composites. *Journal of Composite Materials, 1991, vol. 25, pp. 932-958.*

[27] Wu Y, Dong Z. Three dimensional finite element analysis of composites with coated spherical inclusions. *Materials Science and Engineering, 1995, vol. 203, pp. 314-337.*

[28] Ghosn LJ, Lerch BA. Optimum interface properties for metal matrix composites. *NASA Technical Memorandum, 1989, vol. 102295, pp. 1-19.*

[29] Jansson S, Leckie FA. Reduction of thermal stresses in continuous fibre reinforced metal matrix composites with interface layers. *Journal of Composite Materials, 1992, vol. 26, pp. 1474-1486.*

[30] Carman GP, Averill RC, Reifsnider KL, Reddy JN. Optimization of fiber coatings to minimize stress concentrations in composite materials. *Journal of Composite Materials, 1993, vol. 27, pp. 589-612.*

[31] Al-Ostaz A, Jasiuk I. Effect of interface and random arrangement of inclusions on the local stresses in composite materials. *Durability of Composite Materials, 1994; 51: 207-217.*

[32] Foldy LL. Multiple scattering theory of waves. *Physical Review, 1945; 67: 107-119.*

[33] Lee CS, Ahn AH, DeJonghe LC, Thomas G. Effect of functionally graded material (FGM) layers on the residual stress of polytypoidally joined Si_3N_4–Al_2O_3, *Materials Science and Engineering: A, 2006, vol. 434, pp. 160-165.*

[34] Cammarata, RC. Surface and interface stresses effects in thin films. *Progress in Surface Science, 1994, 46, 1–38.*

[35] Cammarata, RC. Surface and interface stress effects on interfacial and nanostructured materials. *Materials Science and Engineering: A, 1997,237, 180–184.*

[36] Streitz, FH, Cammarata, RC, and Sieradzki, K. Surface-stress effects on elastic properties. I. *Thin metal films. Physics Rev., B, 1994, 49, 10699–10706.*

[37] Gurtin, ME, and Murdoch, AI. Acontinuum theory of elastic material surfaces. *Archives of Rational Mechanics and Analysis, 1975, 57, 291–323.*

[38] Gurtin, ME, and Murdoch, AI. Surface stress in solids. *International Journal of Solids and Structures, 1978, 14, 431–440.*

[39] Murdoch, AI. Thermodynamical theory of elastic-material interfaces. *Quarterly Journal of Mechanics and Applied Mathematics, 1976, 29, 245–275.*

[40] Gurtin, M E, Weissmüller, J, and Larché, F. Ageneral theory of curved deformable interfaces in solids at equilibrium. *Philosophical. Magazine, A, 1998,78, 1093–1109.*

[41] Shenoy, VB. Atomistic calculations of elastic properties of metallic fcc crystal surfaces. *Physics Rev., B, 2005, 71, 094104-1–11.*

[42] Miller, RE, and Shenoy, VB. Size-dependent elastic properties of nanosized structural elements. *Nanotechnology, 2000, 11, 139–147.*

[43] Shenoy, VB. Size-dependent rigidities of nanosized torsional elements. *International Journal of Solids and Structures, 2002, 39, 4039–4052.*

[44] Cuenot, S, Fr'etigny, C, Demoustier-Champagne, S, and Nysten, B. Surface tension effect on the mechanical properties of nanomaterials measured by atomic force microscopy. *Physics Rev., B, 2004, 69, 165410–165413.*

[45] Jing, GY, Duan, HL, Sun, XM, Zhang, ZS, Xu, J, Li, YD, Wang, J, and Yu, DP. Surface effects on elastic properties of silver nanowires: contact atomic-force microscopy. *Physics Rev., B 2006, 73, 235409-1–6.*

[46] Sharma, P, Ganti, S, and Bhate, N. Effect of surfaces on the sizedependent elastic state of nano-inhomogeneities. *Applied Physics Letters, 2003, 82, 535–537.*

[47] Fang, QH, and Liu, YW. Size-dependent interaction between an edge dislocation and a nanoscale inhomogeneity with interface effects. *Acta Materialia, 2006, 54, 4213–4220.*

[48] Wang, GF, and Wang, TJ. Deformation around a nanosized elliptical hole with surface effect. *Applied Physics Letters, 2006, 89, 161901-1–3.*

[49] Paskaramoorthy, R., Meguid, SA. On the dynamic behavior of porous materials. *Journal of Solids and Structures, 2000, 37, 2341-2358.*

[50] Wang, GF, Wang, TJ, and Feng, XQ. Surface effects on the diffraction of plane compressional waves by a nanosized circular hole. *Applied Physics Letters, 2006, 89, 231923-1–3.*

[51] Wang, GF. Diffraction of shear waves by a nanosized spherical cavity. *Journal of Applied Physics, 2008,103, 053519-5.*

[52] Wang, GF, Feng XQ, and Yu SW. Interface effects on the diffraction of plane compressional waves by a nanosized spherical inclusion. *Journal of Applied Physics, 2007,102, 043533.*

[53] Cook, RD, Malkus, DS, Plesha, ME. Concepts and applications of finite element analysis, third ed., *John Wiley & Sons, New York, 1989.*

[54] Lancaster, P. 1969. Theory of Matrices, pp. 301–307, Academic Press, New York.

[55] Dong, SB, 1981. Global-local finite element methods. In: Pilkey, W.D., Noor, A.K. (Eds), *State-of-the-Art Survey of Finite Element Methods (Chap. 14) ASME Publication.*

[56] Taya M. and Arsenault RJ. Metal Matrix Composites. *Permagon Pres, New York, 1989.*

[57] Gaofeng Q, Yujiu S, and Mingjing T. Mechanical Properties and Evaluation of Magnesium Matrix Composites. *Proceding of the Second International Conference of Composite Science and Technology, Jun 1998, pp. 175-179.*

[58] Ranganath S.A. Review on Particulate-reinforced Titanium Matrix Composites. *Journal of Material Science, vol. 32, 1997, pp. 1-16.*

[59] Noor A.K. and Levine S.R. Composite Materials, vol 3: Flight-Vehicle Material, Structures and Dynamic Assessment & Future Directions. *Academic Press, 1974.*

[60] Eshelby JD. 1957. The determination of the elastic field of an ellipsoidal inclusion and related problems. *Proceedings of Royal Society of London Series, A, 241:376–86.*

[61] Eshelby JD. 1959. The elastic field outside an ellipsoidal inclusion. *Proceedings of Royal Society of London Series, A, 252:561–9.*

[62] Koizumi M. 1997. FGM activities in Japan. *Composites Part B; 28:1–4.*

[63] Lee CS, Ahn AH, DeJonghe LC, Thomas G. 2006. Effect of functionally graded material (FGM) layers on the residual stress of polytypoidally joined. *Materials Science and Engineering, A; 434:160–5.*

Appendix A

Assuming $\left\{\overline{q}_B^{sct}\right\}_{sph}$ is known, equation (3.41) may be solved for $\{a\}$ by minimizing the least square error of the error function $\{\varepsilon\}$ defined by

$$\{\varepsilon\} = [G]\{a\} - \left\{\overline{q}_B^{s}\right\}_{sph} \tag{A.1}$$

The square of the ε^2, which is a scalar, is given by

$$\varepsilon^2 = \left\{\varepsilon^*\right\}^T \{\varepsilon\} \tag{A.2}$$

Substitution of (A1) in (A2) leads to

$$\varepsilon^2 = \left\{a^*\right\}^T \left[G^*\right]^T [G]\{a\} - \left\{\overline{q}_B^{s^*}\right\}_{sph}^T [G]\{a\} - \left\{a^*\right\}^T \left[G^*\right]^T \left\{\overline{q}_B^{s}\right\}_{sph} + \left\{\overline{q}_B^{s^*}\right\}_{sph}^T \left\{\overline{q}_B^{s}\right\}_{sph} \tag{A.3}$$

Minimizing the square of the error with respect to $\{a\}$ yields

$$\left[G^*\right]^T [G]\{a\} = \left[G^*\right]^T \left\{\overline{q}_B^{s}\right\}_{sph} \tag{A.4}$$

Since

$\left[G^*\right]^T \ [G]$ is a square matrix, the Equation. (A4) can be solved for $\{a\}$ as

$$\{a\} = [H]\left\{\overline{q}_B^{s}\right\}_{sph} \tag{A.5}$$

where

$$[H] = \left(\left[G^*\right]^T [G]\right)^{-1} \left[G^*\right]^T \tag{A.6}$$

For $p \le N_B$, $[H]$ is the generalized inverse of $[G]$ and the uniqueness of the operation is assured (Lancaster [54]).

Appendix B

$$E(1,1) = \frac{2\mu_1}{R^2}\left[\left(n^2 - n - \frac{1}{2}\beta_1^2 R^2\right) h_n(\alpha_1 R) + 2\alpha_1 R\, h_{n+1}(\alpha_1 R)\right] \tag{B.1}$$

$$E(1,2) = \frac{2\mu_1}{R^2}\frac{n(n+1)}{\beta_1}\left[(n-1)\ h_n(\beta_1 R) - \beta_1 R\, h_{n+1}(\beta_1 R)\right] \tag{B.2}$$

$$E(1,3) = -\frac{2\mu_3}{R^2}\left[\left(n^2 - n - \frac{1}{2}\beta_3^2 R^2\right) j_n(\alpha_3 R) + 2\alpha_3 R\ j_{n+1}(\alpha_3 R)\right] \tag{B.3}$$

$$E(1,4) = -\frac{2\mu_3}{R^2}\frac{n(n+1)}{\beta_3}\left[(n-1)\ j_n(\beta_3 R) - \beta_3 R\, j_{n+1}(\beta_3 R)\right] \tag{B.4}$$

$$E(1,5) = -\frac{2\mu_3}{R^2}\left[\left(n^2 - n - \frac{1}{2}\beta_3^2 R^2\right) y_n(\alpha_3 R) + 2\alpha_3 R\ y_{n+1}(\alpha_3 R)\right] \tag{B.5}$$

$$E(1,6) = -\frac{2\mu_3}{R^2}\frac{n(n+1)}{\beta_3}\left[(n-1)\ y_n(\beta_3 R) - \beta_3 R\, y_{n+1}(\beta_3 R)\right] \tag{B.6}$$

$$E(1,7) = 0 \tag{B.7}$$

$$E(1,8) = 0 \tag{B.8}$$

$$E(2,1) = \frac{2\mu_1}{R^2}\left[(n-1)\ h_n(\alpha_1 R) - \alpha_1 R\, h_{n+1}(\alpha_1 R)\right] \tag{B.9}$$

$$E(2,2) = \frac{2\mu_1}{R^2}\frac{1}{\beta_1}\left[\left(n^2 - n - \frac{1}{2}\beta_1^2 R^2\right) h_n(\beta_1 R) + 2\beta_1 R\ h_{n+1}(\beta_1 R)\right] \tag{B.10}$$

$$E(2,3) = -\frac{2\mu_3}{R^2}\left[(n-1)\ j_n(\alpha_3 R) - \alpha_3 R\, j_{n+1}(\alpha_3 R)\right] \tag{B.11}$$

$$E(2,4) = -\frac{2\mu_3}{R^2}\frac{1}{\beta_3}\left[\left(n^2 - n - \frac{1}{2}\beta_3^2 R^2\right) j_n(\beta_3 R) + \beta_3 R\ j_{n+1}(\beta_3 R)\right] \tag{B.12}$$

$$E(2,5) = -\frac{2\mu_3}{R^2}\left[(n-1)\ y_n(\alpha_3 R) - \alpha_3 R\, y_{n+1}(\alpha_3 R)\right] \tag{B.13}$$

$$E(2,6) = -\frac{2\mu_3}{R^2}\frac{1}{\beta_3}\left[\left(n^2 - n - \frac{1}{2}\beta_3^2 R^2\right) y_n(\beta_3 R) + \beta_3 R\ y_{n+1}(\beta_3 R)\right] \tag{B.14}$$

$$E(2,7) = 0 \tag{B.15}$$

$$E(2,8)=0 \tag{B.16}$$

$$E(3,1)=\left[\frac{n}{R}\,h_n(\alpha_1 R)-\alpha_1\,h_{n+1}(\alpha_1 R)\right] \tag{B.17}$$

$$E(3,2)=n(n+1)\frac{h_n(\beta_1 R)}{\beta_1 R} \tag{B.18}$$

$$E(3,3)=-\left[\frac{n}{r}\,j_n(\alpha_3 R)-\alpha_3\,j_{n+1}(\alpha_3 R)\right] \tag{B.19}$$

$$E(3,4)=-n(n+1)\frac{j_n(\beta_3 R)}{\beta_3 R} \tag{B.20}$$

$$E(3,5)=-\left[\frac{n}{R}\,y_n(\alpha_3 R)-\alpha_3\,y_{n+1}(\alpha_3 R)\right] \tag{B.21}$$

$$E(3,6)=-n(n+1)\frac{y_n(\beta_3 R)}{\beta_3 R} \tag{B.22}$$

$$E(3,7)=0 \tag{B.23}$$

$$E(3,8)=0 \tag{B.24}$$

$$E(4,1)=\frac{h_n(\alpha_1 R)}{R} \tag{B.25}$$

$$E(4,2)=\left[(n+1)\frac{h_n(\beta_1 R)}{\beta_1 R}-h_{n+1}(\beta_1 R)\right] \tag{B.26}$$

$$E(4,3)=-\frac{j_n(\alpha_3 R)}{R} \tag{B.27}$$

$$E(4,4)=-\left[(n+1)\frac{j_n(\beta_3 R)}{\beta_3 R}-j_{n+1}(\beta_3 R)\right] \tag{B.28}$$

$$E(4,5)=-\frac{y_n(\alpha_3 R)}{R} \tag{B.29}$$

$$E(4,6)=-\left[(n+1)\frac{y_n(\beta_3 R)}{\beta_3 R}-y_{n+1}(\beta_3 R)\right] \tag{B.30}$$

$$E(4,7)=0 \tag{B.31}$$

$$E(4,8)=0 \tag{B.32}$$

$$E(5,1)=0 \tag{B.33}$$

$$E(5,2)=0 \tag{B.34}$$

$$E(5,3)=\frac{2\mu_3}{R^2}\left[\left(n^2-n-\frac{1}{2}\beta_3^2R^2\right)j_n(\alpha_3R)+2\alpha_3R\ j_{n+1}(\alpha_3R)\right] \tag{B.35}$$

$$E(5,4)=\frac{2\mu_3}{R^2}\frac{n(n+1)}{\beta_3}\left[(n-1)\ j_n(\beta_3R)-\beta_3R\,j_{n+1}(\beta_3R)\right] \tag{B.36}$$

$$E(5,5)=\frac{2\mu_3}{R^2}\left[\left(n^2-n-\frac{1}{2}\beta_3^2R^2\right)y_n(\alpha_3R)+2\alpha_3R\ y_{n+1}(\alpha_3R)\right] \tag{B.37}$$

$$E(5,6)=\frac{2\mu_3}{R^2}\frac{n(n+1)}{\beta_3}\left[(n-1)\ y_n(\beta_3R)-\beta_3R\,y_{n+1}(\beta_3R)\right] \tag{B.38}$$

$$E(5,7)=-\frac{2\mu_3}{R^2}\left[\left(n^2-n-\frac{1}{2}\beta_2^2R^2\right)j_n(\alpha_2R)+2\alpha_2R\ j_{n+1}(\alpha_2R)\right] \tag{B.39}$$

$$E(5,8)=-\frac{2\mu_2}{R^2}\frac{n(n+1)}{\beta_2}\left[(n-1)\ j_n(\beta_2R)-\beta_2R\,j_{n+1}(\beta_2R)\right] \tag{B.40}$$

$$E(6,1)=0 \tag{B.41}$$

$$E(6,2)=0 \tag{B.42}$$

$$E(6,3)=\frac{2\mu_3}{R^2}\left[(n-1)\ j_n(\alpha_3R)-\alpha_3R\,j_{n+1}(\alpha_3R)\right] \tag{B.43}$$

$$E(6,4)=\frac{2\mu_3}{R^2}\frac{1}{\beta_3}\left[\left(n^2-n-\frac{1}{2}\beta_3^2R^2\right)\ j_n(\beta_3R)+\beta_3R\ j_{n+1}(\beta_3R)\right] \tag{B.44}$$

$$E(6,5)=\frac{2\mu_3}{R^2}\left[(n-1)\ y_n(\alpha_3R)-\alpha_3R\,y_{n+1}(\alpha_3R)\right] \tag{B.45}$$

$$E(6,6)=\frac{2\mu_3}{R^2}\frac{1}{\beta_3}\left[\left(n^2-n-\frac{1}{2}\beta_3^2R^2\right)\ y_n(\beta_3R)+\beta_3R\ y_{n+1}(\beta_3R)\right] \tag{B.46}$$

$$E(6,7)=-\frac{2\mu_2}{R^2}\left[(n-1)\ j_n(\alpha_2R)-\alpha_2R\,j_{n+1}(\alpha_2R)\right] \tag{B.47}$$

$$E(6,8) = -\frac{2\mu_2}{R^2}\frac{1}{\beta_2}\left[\left(n^2 - n - \frac{1}{2}\beta_2^2 R^2\right)\ j_n(\beta_2 R) + \beta_2 R\ j_{n+1}(\beta_2 R)\right] \tag{B.48}$$

$$E(7,1) = 0 \tag{B.49}$$

$$E(7,2) = 0 \tag{B.50}$$

$$E(7,3) = \left[\frac{n}{R}\ j_n(\alpha_3 R) - \alpha_3\ j_{n+1}(\alpha_3 R)\right] \tag{B.51}$$

$$E(7,4) = n(n+1)\frac{j_n(\beta_3 R)}{\beta_3 R} \tag{B.52}$$

$$E(7,5) = \left[\frac{n}{R}\ y_n(\alpha_3 R) - \alpha_3\ y_{n+1}(\alpha_3 R)\right] \tag{B.53}$$

$$E(7,6) = n(n+1)\frac{y_n(\beta_3 R)}{\beta_3 R} \tag{B.54}$$

$$E(7,7) = -\left[\frac{n}{R}\ j_n(\alpha_2 R) - \alpha_2\ j_{n+1}(\alpha_2 R)\right] \tag{B.55}$$

$$E(7,8) = -n(n+1)\frac{j_n(\beta_2 R)}{\beta_2 R} \tag{B.56}$$

$$E(8,1) = 0 \tag{B.57}$$

$$E(8,2) = 0 \tag{B.58}$$

$$E(8,3) = \frac{j_n(\alpha_3 R)}{R} \tag{B.59}$$

$$E(8,4) = \left[(n+1)\frac{j_n(\beta_3 R)}{\beta_3 R} - j_{n+1}(\beta_3 R)\right] \tag{B.60}$$

$$E(8,5) = \frac{y_n(\alpha_3 R)}{R} \tag{B.61}$$

$$E(8,6) = \left[(n+1)\frac{y_n(\beta_3 R)}{\beta_3 R} - y_{n+1}(\beta_3 R)\right] \tag{B.62}$$

$$E(8,7) = -\frac{j_n(\alpha_2 R)}{R} \tag{B.63}$$

$$E(8,8) = -\left[(n+1)\frac{j_n(\beta_2 R)}{\beta_2 R} - j_{n+1}(\beta_2 R)\right] \tag{B.64}$$

$$f(1,1) = -i^n (2n+1) \left(\frac{2\mu_1}{R^2}\right)\left[\left(n^2 - n - \frac{1}{2}\beta_1^2 R^2\right) j_n(\alpha_1 R) + 2\alpha_1 R\, j_{n+1}(\alpha_1 R)\right] \quad \text{(B.65)}$$

$$f(2,1) = -i^n (2n+1) \left(\frac{2\mu_1}{R^2}\right)\left[(n-1)\ j_n(\alpha_1 R) - \alpha_1 R\, j_{n+1}(\alpha_1 R)\right] \quad \text{(B.66)}$$

$$f(3,1) = -i^n (2n+1)\left[\frac{n}{R}\ j_n(\alpha_1 R) - \alpha_1\, j_{n+1}(\alpha_1 R)\right] \quad \text{(B.67)}$$

$$f(4,1) = -i^n (2n+1)\left(\frac{j_n(\alpha_1 R)}{\beta_1 R}\right) \quad \text{(B.68)}$$

$$f(5,1)\ to\ f(8,1) = 0 \quad \text{(B.69)}$$

Appendix C

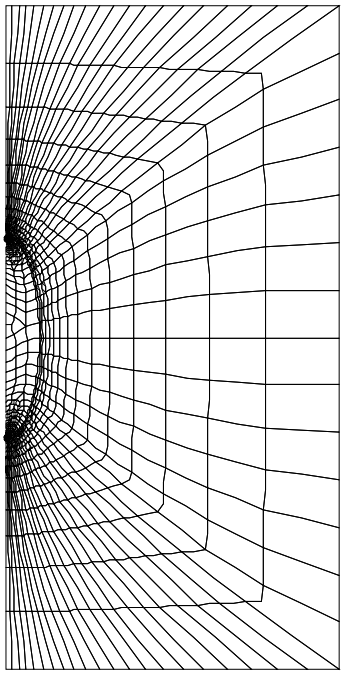

Figure C.1. Finite element mesh for the spheroidal particle (*b/a*=3) for static loading case

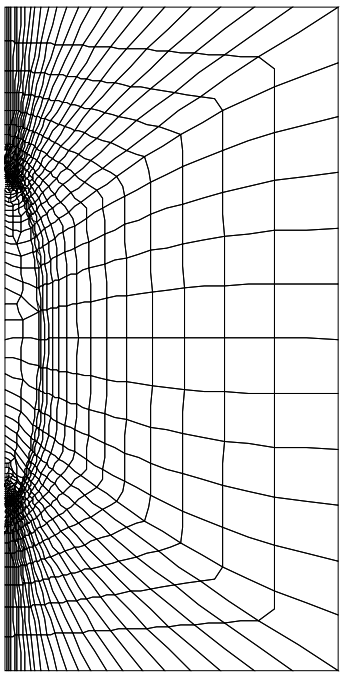

Figure C.2. Finite element mesh for the spheroidal particle (*b/a*=5) for static loading case

Appendix D

The elements of the matrices ***[E]*** and ***[P]*** and vectors ***{f}*** and ***{q}*** in equations (4.50) and (4.51) are given by:

$$E_{11} = c_1 - 2k_3c_3 + n(n+1)k_3c_4 \tag{D.1}$$

$$E_{12} = c_2 - 2k_3c_5 + n(n+1)k_3c_6 \tag{D.2}$$

$$E_{13} = -k_{10}e_1 \tag{D.3}$$

$$E_{14} = -k_{10}e_2 \tag{D.4}$$

$$E_{21} = c_9 + k_6c_1 + (k_4 + k_5)c_3 - n(n+1)k_4c_4 + (k_4 - k_5)c_4 \tag{D.6}$$

$$E_{22} = c_{10} + k_6c_2 + (k_4 + k_5)c_5 - n(n+1)k_4c_6 + (k_4 - k_5)c_6 \tag{D.7}$$

$$E_{23} = -e_9 \tag{D.8}$$

$$E_{24} = -e_{10} \tag{D.9}$$

$$E_{31} = c_{21} \tag{D.10}$$

$$E_{32} = c_{22} \tag{D.11}$$

$$E_{33} = -e_{21} \tag{D.12}$$

$$E_{34} = -e_{22} \tag{D.13}$$

$$E_{41} = c_{23} \tag{D.14}$$

$$E_{42} = c_{24} \tag{D.15}$$

$$E_{43} = -e_{23} \tag{D.16}$$

$$E_{44} = -e_{24} \tag{D.17}$$

$$f_1 = -\frac{i^{(n+1)}(2n+1)}{n(n+1)}\left[d_2 - 2k_3d_5 + n(n+1)k_3d_6\right] \tag{D.18}$$

$$f_2 = -\frac{i^{(n+1)}(2n+1)}{n(n+1)}\left[d_{10} + k_6d_2 + (k_4 + k_5)d_5 - n(n+1)k_4d_6 + (k_4 - k_5)d_6\right] \tag{D.19}$$

$$f_3 = -\frac{i^{(n+1)}(2n+1)}{n(n+1)}d_{22} \tag{D.20}$$

$$f_4 = -\frac{i^{(n+1)}(2n+1)}{n(n+1)}d_{24} \tag{D.21}$$

$$P_{11} = c_{11} + (k_4 - k_5)\left(-\frac{1}{2}n(n+1) + 1\right)c_{12} \tag{D.22}$$

$$P_{12} = -e_{11} \tag{D.23}$$

$$P_{21} = c_{25} \tag{D.24}$$

$$P_{22} = -e_{25} \tag{D.25}$$

$$q_1 = \frac{(-i)^n(2n+1)}{n(n+1)}\left[d_{11} + (k_4 - k_5)\left(-\frac{1}{2}n(n+1) + 1\right)d_{12}\right] \tag{D.26}$$

$$q_2 = \frac{(-i)^n(2n+1)}{n(n+1)}d_{25} \tag{D.27}$$

where

$$k_3 = \frac{2\left(k_1 + k_2\right)\left(1 - v\right)}{1 + 4v\left(k_1 + k_2\right)} \tag{D.28}$$

$$k_4 = k_1\left(1 - v\right) + 2k_2 \tag{D.29}$$

$$k_5 = k_1\left(1 - v\right) + 2k_2 v \tag{D.30}$$

$$k_6 = 2\left(k_1 + k_2\right)v \tag{D.31}$$

$$k_{10} = \frac{1}{1 + 4v\left(k_1 + k_2\right)} \tag{D.32}$$

In the above equations c_1, c_2,..., etc are calculated using $h_n^{(1)}$ for Z_n and α and β are those of matrix.

The d_1, d_2,..., etc have identical expressions as c_1, c_2,..., etc but are calculated using j_n for Z_n and α and β are those of matrix.

The e_1, e_2,..., etc have identical expressions as c_1, c_2,..., etc but are calculated using j_n for Z_n and α and β are those of the nano-particle.